Impact of Nanoparticles and Fillers in Polymer Nanocomposites and Additive Manufacturing

A Dissertation Presented for the
Doctor of Philosophy
Degree
The University of Tennessee, Knoxville

Sahar Sherif Hassan Rostom
August 2019

Copyright © 2019 by Sahar Rostom
All rights reserved.

DEDICATION

This dissertation is dedicated to my loving husband Ahmed Amer. Without his patience and emotional support, the work presented here would never have been accomplished. I would also like to dedicate this work to my three lovely kids, Hala Amer, Yara Amer and Yusuf Amer, without their hugs and kisses to cheer me up along the way, I would have never made it through. Finally, I would like to dedicate the work to my parents and father in law who supported me throughout this entire path.

ACKNOWLEDGEMENTS

I would like to acknowledge the financial and academic support of Dr. Mark Dadmun without which this dissertation would have never been possible. I would like to thank my committee members Dr. Bin Zhao, Dr. Charles Feigerle, and Dr. Verlee Keppens for their time and deliberation during this long process. I would additionally like to thank all my colleagues in my current research lab for their companionship and support, especially, Dr. Umesh Shrestha, Dr. Neiko Levenhagen, Dr. Samantha Rinehart, Ms. Leondra Lawson, Mr. Kai Guan, Mr. Connor Perryman, Mr. Jacob Fischer, Mr. Josh Moncada and Mr. Luke Heroux. I would specifically like to thank Dr. Xinhao Feng, Dr. David Harper, Dr. Brian Eduards, Dr. Tyler White, Dr. Tomonori Saito and Dr. Ahmed Hassan for the fruitful collaboration. Additionally, I would like to thank all of the former graduate students who provided a source of hope and inspiration, especially Dr. Halie Martin, Dr. Brad Miller, Dr. Adam Imel, Dr. Eddie Duranty, and Dr. Brian Morgan. Finally, I would like to thank all of the people outside of the University of Tennessee who were by my side and believed in me for all these years.

ABSTRACT

The dissertation presents work that improves our understanding of the impact of soft nanoparticles on the dynamics of linear polymer in all-polymer nanocomposites and the impact of graphene on the thermal and mechanical properties of PLA in fused deposition modeling. Polymer nanocomposites in which soft, polymer-based nanoparticles are dispersed in the polymer matrix have received great interest lately due to their potential use in a range of applications, including drug delivery and self healing materials. However, the impact of this new class of nanoparticles on the dynamics of a linear polymer matrix in an all-polymer nanocomposite is still largely unknown. In the first chapter, we determine the polystyrene soft nanoparticles on the diffusion of high molecular weight linear PS chains as a function of nanoparticle loading. Our results show that at loadings below 1% of the nanoparticle, the diffusion of the linear matrix increases by a factor of two presumably via a constraint release mechanism, while at loadings above 1% the increase in diffusion is mitigated by confinement effects of the nanoparticles. This transition happens when the distance between nanoparticles is similar to the size of the polymer chain of the matrix ($ID/2R_g \sim 1$). The next project presents a protocol for determining tracer diffusion coefficients of soft nanoparticles and correlate its topology to observed dynamics. The results suggest that the nanoparticle softness and deformability dictate its motion. Increasing the crosslinking density of the nanoparticle increases its hardness and suppresses its motion in the linear matrix. The third project examines the effect of graphene on

thermal transport and inter-filament bonding in 3D printing of PLA. The incorporation of graphene at low loadings appears to enhance thermal conductivity and lead to more uniform thermal gradients. Additionally, at low graphene loading, high bed temperatures can be utilized to enhance thermal transfer in the z direction and improve mechanical strength. Finally, the last project evaluates the impact of graphene on irreversible thermal strains of PLA in FDM. The results demonstrate the potential to mitigating warping through graphene incorporation and control of thermal evolution throughout the printing process.

TABLE OF CONTENTS

Chapter 1 Introduction 1
Introduction 2
Soft Polymeric Nanoparticles 7
Polystyrene Soft Nanoparticles 7
Emulsion Polymerization of Soft Nanoparticle 9
Introduction to Additive Manufacturing 13
Nanoscale Additives for 3D Printing 17
Graphene 17
Thermal Conductivity Mechanism in Graphene and Nanocomposites 23
Dissertation Outline and Objective 25
Chapter 2 The Impact of Soft Nanoparticle Concentration on Polymer Chain Diffusion in Polymer Nanocomposites 26
Introduction 27
Experimental 33
Results and Discussion 38
Conclusion 54
Chapter 3 The Importance of Nanoparticle Softness on its Tracer Diffusion Coefficient in a Linear Polymer Matrix 55
Introduction 56
Experimental 59
Results and Discussion 63
Conclusion 86
Chapter 4 Enhancing Inter Filament Bonding of PLA via Graphene Reinforcement in Fused Deposition Modeling 88
Introduction 89
Experimental 94
Materials 94
Composite Fabrication 94
3D Printing and Thermal Characterization 96
Mechanical Testing and Void Space Analysis Using SEM 96
% Crystallinity Evaluation Using Differential Scanning Calorimetry (DSC) 99
Thermal Conductivity 99
Results 100
Tensile Properties 100
Determination of Interfilament Voids 108
Monitoring the Thermal Profile 113
Thermal Conductivity 119
Analysis of Crystallinity 119
Discussion 122
Conclusion 126

Chapter 5 The Effect of Graphene on Residual Stress and Irreversible Thermal Expansion in FDM Printed Samples 128
Introduction 129
Experimental 132
Materials 132
Composite Fabrication 132
3D Printing and Thermal Annealing 133
Results and Discussion 133
Conclusion 142
Chapter 6 Conclusion 143
Conclusions and Future Work 144
The Impact of Soft Nanoparticle Concentration on Polymer Chain Diffusion 145
The Importance of Nanoparticle Softness on its Tracer Diffusion Coefficient 147
Enhancing Inter-Filament Bonding of PLA via Graphene Reinforcement in Fused Deposition Modeling 149
The Effect of Graphene on Residual Stress and Irreversible Thermal Expansion in FDM Printed Samples 151
References 153
Vita 172

LIST OF TABLES

Table 2.1: Structural characteristics of the NP1B nanoparticle as determined from small angle neutron scattering (SANS).[33] 34
Table 3.1: Nanoparticle synthesis method and morphology details from small angle neutron scattering (SANS) results. 62
Table 3.2: Mutual diffusion coefficients determined from fitting the volume fractions to the solution of Ficks second law and the tracer diffusion coefficients as estimated using slow and fast mode theory. 74
Table 3.3: Tracer diffusion coefficient at the longest annealing time calculated using the slow mode theory for all nanoparticles. 76
Table 3.4: Experimental tracer diffusion for soft nanoparticle and theoretical Einstein diffusion for hard sphere of same radius. 85
Table 4.1: Tensile properties of printed samples in the Z (transverse) direction. 102
Table 4.2: % Voids in the XY Direction for all samples. 112
Table 4.3: Thermal properties extracted from DSC curves. 121

LIST OF FIGURES

Figure 1.1: Image of soft nanoparticles with different topology due to different % crosslinking density. Fuzzy gel for 0.81%DVB, Smooth gel for 4.6 % and Dendritic gel for 11%. 11
Figure 1.2: Illustration of micelle formation in emulsion polymerization technique. 12
Figure 1.3: Diagram of a common FDM printer and the incremental fabrication procedure. 15
Figure 1.4: Honeycomb structure of monolayer and few Layer graphene showing sp^2 hybridization network and graphene stacking. 18
Figure 1.5: 2D Peak shift in Raman spectrum based of the layer number in graphene sample. The peak shifts to higher wave number and become broader as the number of layers increases.[50] 20
Figure 1.6: (a) AFM image and thickness of graphene utilized in the study. (b) Raman spectrum showing G/2D ratio.[50] 21
Figure 2.1: Diagram illustrating the reflection of Neutrons at an interface. 37
Figure 2.2: Representative reflectivity curves for dPS /PS with 0.5% NP1B loading annealed at 130°C. 39
Figure 2.3: Representative SLD profiles of the dPS/PS bilayer with 0.5 %NP1B loading annealed at 130°C. 41
Figure 2.4: Volume fraction fitting to double error function for control at 8160 seconds. 42
Figure 2.5: Tracer diffusion coefficients versus annealing time for control dPS/PS. 44
Figure 2.6: Plot of the change in the interfacial width between PS and dPS in the neat bilayer as a function of annealing time. 46
Figure 2.7: Diffusion coefficient for neat polymer and nanocomposites with different NP1B loading. 48
Figure 2.8: An illustration to depict cages and bottle necks as presented by the entropic barrier model.[82] 50
Figure 2.9: Reduced diffusion coefficient as a function of the confinement parameter for different NP1B loadings. 52
Figure 3.1: Depiction of the Nanoemulsion synthesis method for soft nanoparticles used in the study. 60
Figure 3.2: Representative reflectivity curves for hPS-dPS bilayers, the y offset is used for clarity. 64
Figure 3.3: Scattering length density (SLD) profile for hPS-dPS bilayer. 66
Figure 3.4: Representative reflectivity curves for NP3AA-dPS bilayers as cast and after the longest annealing time. 67
Figure 3.5: Representative reflectivity curves for NP1B-dPS bilayers as cast and after the longest annealing time. 68
Figure 3.6: Volume fraction profiles NP1A and NP3A. 70
Figure 3.7: Volume fraction profiles NP3A. 71

Figure 3.8: Tracer diffusion coefficient as function of annealing times for all nanoparticles parameter for different NP1B loadings. 75
Figure 3.9: Tracer diffusion coefficients plotted as function of molecular weight for different crosslinking density. 77
Figure 3.10: Log-log plots of tracer diffusion as function of molecular weight for different crosslinking densities for different crosslinking density. 79
Figure 3.11: The ratio of the tracer diffusion of the linear polymer matrix to the nanoparticle analogue as function of crosslinking density. 80
Figure 3.12: Log-log plot of tracer diffusion versus molecular weight for nanoparticle and their linear analogue. 82
Figure 3.13: Predicted Stokes-Einstein diffusion coefficients for hard spheres as a function of radius and tracer diffusion coefficient of the soft nanoparticles. (blue circles for soft nanoparticle with 0.81% crosslinking density, blue squares for crosslinking density of 1.91% and blue triangles for 4.60 %). ... 84
Figure 4.1: Pictures showing the different stages of graphene composite fabrication and filament extrusion. 95
Figure 4.2: a) Picture of the 3D model of the printed cube and b) diagram showing the geometry of the IR Camera placement. 97
Figure 4.3: Filament orientation in Z-direction and XY-direction tensile specimens. 98
Figure 4.4: Diagram describing the TPS instrument setup and sensor position between sample pieces.[124] 101
Figure 4.5: Ultimate stress of each printed sample for samples printed in the Z direction. 103
Figure 4.6: Modulus of each printed sample for samples printed in the Z direction. 104
Figure 4.7: Ultimate stress of each printed sample for samples printed in the XY orientation. 105
Figure 4.8: Modulus of each printed sample for samples printed in the XY orientation. 106
Figure 4.9: SEM images of the inter-filament voids in the Z orientation for a) PLA printed at 70 C bed temperature b) 0.5% graphene composite printed at 70 °C C) PLA printed at 85 °C bed temperature d) 0.5% graphene composite printed at 85 °C bed temperature. 109
Figure 4.10: SEM images of the inter-filament voids in the XY orientation for a) PLA printed at 70 °C bed temperature b) 0.5% graphene composite printed at 70 °C bed temperature c) PLA printed with an 85 °C bed temperature d) 0.5% graphene composite printed with an 85 °C bed temperature. 110
Figure 4.11: Image J analysis of voids for samples in the XY orientation a) PLA printed on a bed temperature of 70 °C b) 0.5% graphene composite printed on a 70 °C bed. 111
Figure 4.12: Thermal profile of the PLA and graphene composite cubes after 30 minutes of printing at 70 °C bed temperature. 114

Figure 4.13: Thermal profile of the PLA and graphene composites cubes after 1 hour 30 minutes at 70 °C bed temperature. 115
Figure 4.14: Thermal profiles after 1 hour 30 minutes of printing at 85 °C bed. 117
Figure 4.15: Thermal profiles for PLA and 0.5% composite at 70 °C and 100 °C bed temperature after 2 hours. 118
Figure 4.16: Thermal conductivity of printed composites at room temperature as function of Graphene loading. 120
Figure 5.1: a) Illustration of the G code model of samples to monitor irreversible thermal expansion b) Geometry, orientation and dimensions of samples. 134
Figure 5.2: Irreversible thermal strain as a function of graphene loading in the z-direction (top) and xy-plane (bottom). 135
Figure 5.3: Residual stress in the z-direction as function of graphene loading. 137
Figure 5.4: Thermal profiles of PLA and graphene composite samples during printing at bed temperature of 70 C°. 140
Figure 5.5: (a) Correlation of the strain in the Y-direction and the strain in the Z direction (b) The relative change in volume as function of graphene loading. 141

CHAPTER 1

INTRODUCTION

Introduction

The demand for novel materials that exhibit unusual properties continues to grow. Among the variety of materials used in industry, polymers have received significant attention due to their potential applications in a wide range of industrial sectors from automotive and aerospace to medicine. Additionally, the growing 3D printing technology have also contributed to the need for polymers with unusual electric, thermal and mechanical properties. In this regard, polymer nanocomposites have great potential to serve as new materials that can fill the gap between required properties and actual performance of existing polymers.[1,2,3,4]

Polymer nanocomposites can be described as mixtures of a polymer major phase and nanoparticles as a second minor phase. The nanoparticles exhibit dimensions of approximately 1 to 100 nm, where their high surface to volume ratio and large interfacial area between the polymer and the nanoparticle can lead to dramatic improvements and introduce some favorable properties to the polymer.[5] However, the dispersion of these nanoparticles within the matrix has been always an issue. Due to poor interactions between the polymer and nanoparticle, the nanoparticle often aggregates within the matrix leading to difficult processing and poor properties.[2,6,7,8]

Additionally, the impact of the nanoparticles on the dynamics of the polymer and their flow properties can be dramatic, where the shape and size of the nanoparticle are vital factors that direct the dynamic behavior of the linear polymer matrix.[9,10,11,12] Consequently, without a thorough understanding of the effect of

nanoparticle structure and size on the dispersion of the nanoparticle and dynamic properties of the ultimate nanocomposite, the rational design of nanocomposites with targeted properties becomes extremely difficult. Moreover, the impact of the different morphological aspects of the nanoparticle on the dynamics and flow behavior of the nanocomposite in particular may lead to unpredictable macroscopic properties such as glass transitions, modulus and toughness.[13,14,15]

Thus, understanding the structure-property relationship in nanocomposites is critical to address the need to understand the complicated correlation between nanoparticle morphology and the resulting dynamics and macroscopic properties of the final nanocomposite.[16] Several techniques, including light scattering, X-ray and neutron scattering can reveal detailed information about the morphology, nanoscale and meso scale structure of nanoparticles and polymer nanocomposites. Neutron scattering and neutron reflectivity, in particular, are useful, where neutrons can extract structural and dynamic information on length scales that range from segmental to intermolecular. Furthermore, neutron reflectivity is a unique tool that can probe the diffusive motion of polymer chains at different time and length scales due to the match in energies of neutrons and excitations range in soft matter. The difference in the scattering length density between deuterated and protonated nuclei allow labeling specific groups or macromolecules to highlight specific molecules that are of interest. Consequently, through isotopic substitution, the dynamics of a particular component in a complex system can be studied.[17,18,19,20]

Previous studies have been completed to elucidate the impact of nanoparticle shape, size and its interaction with the polymer matrix on the dynamics of polymer chains in a nanocomposite. One key finding is that the length scale that appears to control the dynamic behavior in nanocomposites includes the relative size of the polymer matrix to the nanoparticle. Mangal et al. studied the relaxation dynamics of grafted hairy nanoparticles in a poly(methyl methacrylate) (PMMA) matrix. Their studies reveal a transition in dynamics of the polymer chain from fast diffusive to slow hyper diffusive dynamics with an increase in molecular weight of the PMMA matrix beyond entanglements. However, the relaxation time scale in the entangled system is weakly reliant on the PMMA matrix molecular weight and hence, the motion of the nanoparticle is restricted by frictional forces. Consequently, the mobility of the nanoparticle is then operating on a length scale that is larger than the host polymer tube diameter. The author rationalizes these observations based of the balance forces acting on the nanoparticle, where the nanoparticle can only interrupt the motion of subchain segments that have comparable size to the nanoparticle.[21] Cai et al. study also suggests a model to understand nanoparticle motion in entangled polymer systems, where the diameter of the nanoparticle relative to the tube diameter dictates the nanoparticle relaxation and hopping mechanism within the matrix.[22] Grabowski et al. examined the diffusion of a series of gold nanoparticles in poly(n-butyl methacrylate) using fluctuation correlation spectroscopy. The gold nanoparticles examined cover a range of radii which provides a pathway to examine the importance of the ratio of

the nanoparticle size(R_0) to the tube diameter(d_t) and compare experimental diffusion to theoretical Stokes-Einstein diffusion. The results show a large deviation from Stoke- Einstein for smaller nanoparticles, and the recovery of Stokes-Einstein diffusion seemed to be dictated by the relative size of the nanoparticle and matrix tube diameter, where the full coupling to entanglement relaxation requires $2R_0$~7-$10d_t$.[23]

Among the remarkable changes in physical properties with inclusion of nanoparticles, the unexpected viscosity reduction that deviates from Stokes-Einstein behavior is still quite puzzling and not very well understood. In a striking difference to classical models that predict viscosity increase with the incorporation of nanoparticles, nanoparticles that exhibit diameter comparable to the size of single polymer chains may exhibit viscosity reduction. For instance, Senses et al. studied a nearly athermal system comprised of poly(ethylene glycol) grafted gold nanoparticle in a linear poly ethylene oxide matrix to examine the effect of the presence of the nanoparticle on single chain motion as a function of particle size. Their result reveals an increase in the entanglement tube diameter with inclusion of small nanoparticles, where this behavior is not observed for large nanoparticles. These results further validate the importance of nanoparticle size on the dynamics of the neighboring polymer chains. The disentanglement with unchanged Rouse dynamics is quite unique, has not been extensively studied in the literature, and thus requires further study to more thoroughly understand when this behavior can be expected in order to more carefully exploit this phenomenon.[24]

Other important parameters that dictate the dynamic behavior in polymer nanocomposites are the interaction between the nanoparticle and the matrix as well as the concentration of the nanoparticle. For silica nanoparticle with an attractive interaction to the polymer matrix, the formation of a bound polymer layer on the nanoparticle can slow dynamics and direct the elastic modulus of the composite. As an example, a study by Senses et al. observed a transition from diffusive to hyper diffusive motion of the nanoparticle with a change in the nanoparticle concentration in attractive nanocomposites. In these systems, the interfacial chains are considered highly mobile which permits the uncoupling of the polymer motion with viscoelastic reinforcement in strong confinement regimes. The impact of nanoparticle concentration in attractive and non attractive systems is considered a very critical parameter that needs better evaluation and understanding.[25]

Moreover, the interphase region created in systems that involve bound polymers on nanoparticles showed that the bound layer has a great influence on the local and global dynamics of the polymer chain. Some studies have shown no change in the Rouse relaxations in nanocomposites with a weakly attractive interaction between polymer and nanoparticle. However, for strongly attractive polymer-nanoprticle interactions, and this strongly bound layers, a reduction and strong slowdown in polymer dynamics is reported, emphasizing the important role of the chemical nature of the interphase in dictating the dynamics, disentanglements and polymeric reptative motions in polymer nanocmposites.[26]

Soft Polymeric Nanoparticles

Polystyrene Soft Nanoparticles

Due to the ongoing challenge in dispersion of hard nanoparticles such as metals, clays, and carbon nanotubes, new classes of organic based nanoparticles have been synthesized and examined lately as they should have better miscibility with the polymer base matrix and resolve dispersion problems. For this relatively new class of nanoparticles, understanding the relationship between nanoparticle structure and nanocomposite properties is critical. The topology, size and chemical nature of the nanoparticle can have a great impact on the properties and dynamics of the resulting nanocomposite. This correlation between nanoparticle morphology and nanocomposite dynamics in polymer based nanoparticles is rarely addressed in the literature where many questions remain unanswered. Improved knowledge that correelate nanoparticle size, mobility and topology to the polymer matrix dynamics will aid in the fabrication of nanocomposites with targeted properties and open new venues to apply polymer based nanoparticles and their nanocomposites in drug delivery and self-healing materials.[27,28] For instance, designing self-healing materials where the migration of the nanoparticles to defective sites requires detailed knowledge of the nanoparticle diffusion process. Moreover, the use of soft nanoparticles with different architectures such as dendrimers, stars, rings, as drug nano-carriers requires the understanding of the relationship between topology and nanoparticle mobility.[29,30] Although inorganic nanoparticles as well as polymer grafted inorganic nanoparticles have been extensively studied in the literature, the

dynamics of polymer based nanoparticles and their nanocomposites are less frequently addressed. Few studies examine the impact of soft polymer nanoparticle architecture on component dynamics in nanocomposites. One example is a study by Senses at al. that has shown a direct correlation between topology of the nanoparticle and the viscoelastic behavior of the composite. In this study, inclusion of a star nanoparticle with short arms led to large reduction in viscosity of a polymer nanocomposite at low concentrations where the motion of the linear matrix was altered drastically with the addition of star-polymer fillers. The nanoparticle modified the reptation tube, leading to faster dynamics in comparison with neat linear polymers. The non-linear complex architecture of these fillers create different entanglement behavior with the linear matrix, which alters their friction and dynamics. In these systems, the nanoparticle concentration is critical as below 5% nanoparticle, the viscosity of the composite is lower than that of the neat linear polymer, but becomes higher than that of the neat linear polymer at higher concentrations. The nanoparticle compactness, which is related to the number and length of the arm, also influences the viscosity of the ultimate nanocomposite. These results highlight the possibility of controlling nanocomposite viscosity based on the architecture and concentration of the soft nanoparticles added to a linear polymer matrix. However, our understanding of the the mechanism and crucial length scales that lead to either reduction or increase in viscosity is still in its infancy.[31] In a different study by Mackay, cross-linked soft polystyrene nanoparticles were introduced to a linear polystyrene matrix. A

significant reduction in viscosity was observed and the author correlate these changes to an increase in free volume, which is confirmed by a decrease in the glass transition of the nanocomposite.[28] Moreover, a recent study by Martin et al. tested the impact of PS soft nanoparticles on the diffusion of a linear matrix as a function of linear matrix molecular weight. The soft nanoparticle alter the dynamics of the linear matrix differently based of the molecular weight of the matrix and the size of the nanoparticle, suggesting a length scale factor that needs better understanding.[32] The mechanism of diffusion speed up and its correlation with nanoparticle size, concentration and confinement effects can provide further insight onto the mechanism that control polymer chain diffusion in these systems and provide guide lines to synthesize soft nanoparticles that impart targeted properties on their nanocomposites.

Emulsion Polymerization of Soft Nanoparticle

The PS soft nanoparticles used in this thesis were prepared using conventional micro and nano emulsion polymerization where a hydrophobic styrene monomer is emulsified in water and polymerization is initiated using water soluble initiator. A cross linking agent is copolymerized with the monomer to form crosslinked PS nanoparticles with varied topology. The PS-soft nanoparticle is portrayed as a spherical particle with a crosslinked core and a fuzzy surface of PS chain loops and ends. By increasing the crosslinking density, the softness of the nanoparticle is controlled, where Figure 1.1 is an illustration of 3 distinct

nanoparticle morphologies that have been identified with variation in crosslinking density.[8]

During emulsion polymerization, the hydrophobic monomer is emulsified by a surface active agent or surfactant which is present in excess. As the concentration of the surfactant surpasses the critical micelle concentration, the surfactant aggregates and forms spherical micelles. The initiator starts polymerization within the micelle that continues to grow as more monomer is fed into the reaction vessel. As the polymerization terminates the micelle is considered swollen. Figure 1.2 is an illustration of the emulsion polymerization technique. [33,34]

Our previous studies have shown that control of the rate of monomer addition can controllably alter the size of the nanoparticles formed. The manipulation of a semi-batch method where the monomer is slowly added to the system results in nanoparticles with slightly smaller diameter and lower molecular weight.[33]

Traditionally emulsion polymerization takes place in three intervals. The first interval involves the increase in micelles with growing polymer as nucleation of the droplet occurs. By the end of this interval, the surfactant is depleted. A second interval is considered a particle growth stage where the growing polymer particle increases in size until monomer droplets are exhausted. Interval three starts after the monomer is depleted and the polymer size increases as the latex particles become monomer starved. The addition of the monomer in a very slow rate limits the size of the micelles formed in interval two where there is no excess monomer



Figure 1.1: Image of soft nanoparticles with different topology due to different % crosslinking density. Fuzzy gel for 0.81%DVB, Smooth gel for 4.6 % and Dendritic gel for 11%.

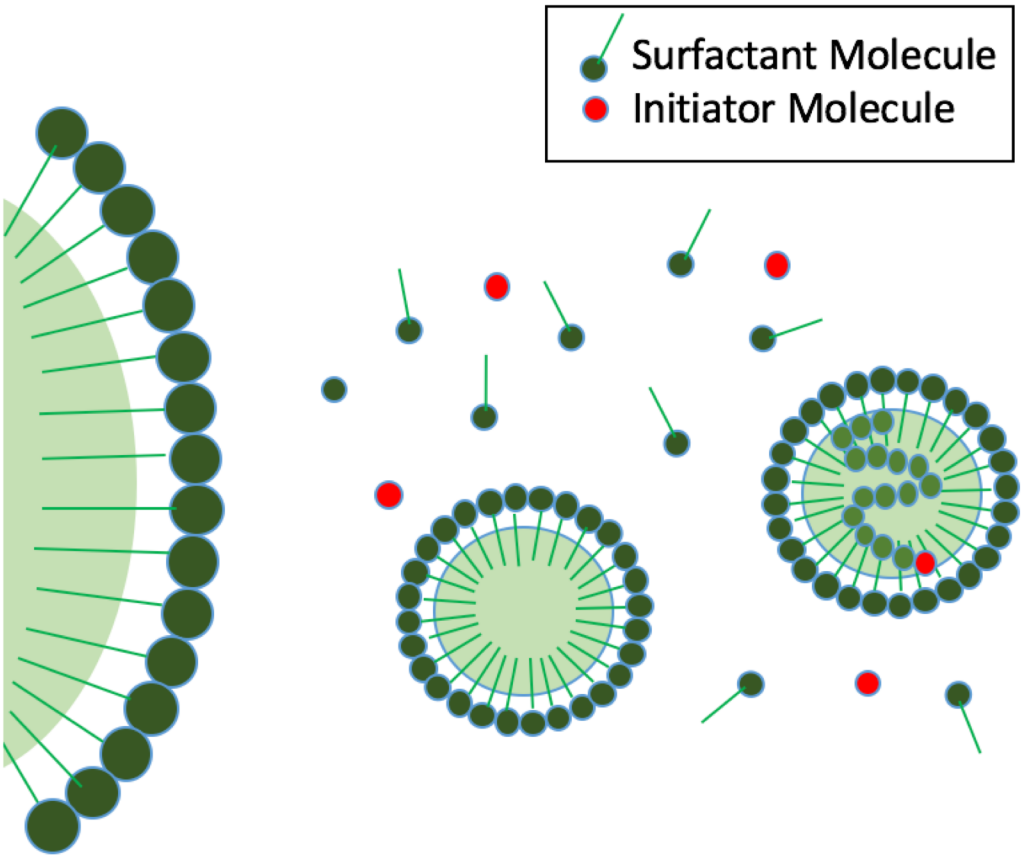

Figure 1.2: Illustration of micelle formation in emulsion polymerization technique.

for the micelle to grow. By adding new monomer with time, new micelles are innoculated and the micelle is never swollen beyond the nano size. The control over the monomer addition rate and the cross linking density is then a versatile route to develop soft nanoparticle with wide range of topologies and sizes.

Introduction to Additive Manufacturing

Additive manufacturing is a growing technology that has the potential to transform industry through fabrication of complicated geometries and structures rapidly and efficiently. Complicated 3D Structures can be built in a layer by layer fashion with high spatial accuracy. Additive manufacturing has evolved from a few starting technologies such as stereolithography (SLA), and powder bed fusion to offer a wide range of newly developed printing techniques including fused deposition modeling (FDM), inkjet printing and contour crafting.[35] FDM is considered one of the most promising and versatile forms of 3D printing, consequently, the technology has gained substantial interest in the past few years. As one of the most cost effective 3D printing techniques, several sectors are interested in FDM prototyping technique including the biomedical, aerospace and automotive industries.[36,37,38] Subsequently, significant research in the area is focused on improving the robustness and mechanical strength of fabricated prototypes in an effort to move the technology towards large scale manufacturing. The FDM printing procedure starts with an AutoCAD model that can be sliced onto layers using a slicing program. The model is then built layer by layer in an incremental fashion from base to top, where a polymer filament is extruded at high

temperature and laid down on a printing bed to cool down and solidify. Figure 1.3 is an illustration of a typical FDM printer. The printing process then relies on thermal energy provided by the extrusion head and printing bed to control polymer solidification and diffusion between layers that provides the physical bonding at inter-filament interfaces.[39,40] A significant challenge that continues to face the technology is poor mechanical properties at the inter-filament interface and poor dimensional accuracy due to warping and residual stress accumulated during printing. Moreover, large voids and pores between the solidified layers are frequently observed in most recent studies, resulting in an anisotropy of the mechanical properties, where the mechanical properties in the direction parallel to the bed (XY) and along the deposition direction are significantly better than those in the perpendicular direction (Z).[41,42,43]

Understanding how thermal properties of a material dictates the thermal history that a material experiences during the printing process, as well as the impact on mechanical properties and residual stress is necessary to improve bonding at the inter-filament interface and enhance dimensional accuracy within the printed samples. Among different polymers utilized in FDM, poly lactic acid (PLA) and acrylonitrile butadiene styrene (ABS) are the most widely used. As most polymers are insulating, these polymers exhibit poor thermal conductivity and high thermal expansion coefficient that lead to poor dimensional stability and fast cooling rates that can inhibit diffusion and weaken adhesion.[44,45,46] A study by Compton et al reveals the direct impact of different printing parameters on the

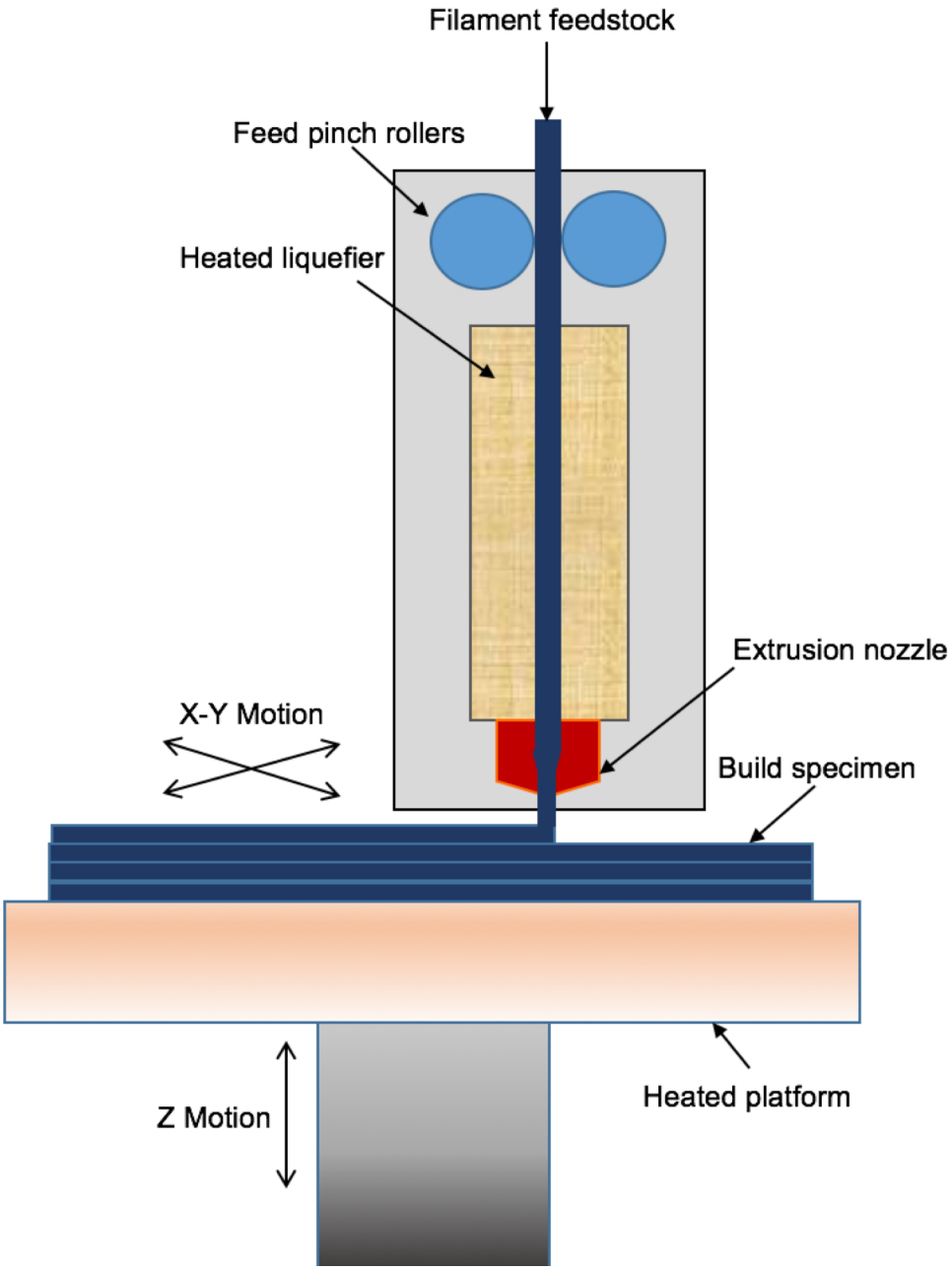

Figure 1.3: Diagram of a common FDM printer and the incremental fabrication procedure.

thermal history and cooling rates of ABS and ABS/carbon fiber during printing. The author used a thermal IR camera to monitor the thermal history of the sample during printing and used these experimental results to build a 1D model that predicts cooling rates and temperature evolution as a function of printing time. The results show very good correlation between thermal conductivity and temperature of the printed layers as well as cooling rates. An important finding is that the bed temperature seems to augment the heating of the printed filament as thermal conductivity of the polymer increases suggesting a pathway in control heat input by the bed and alter layer cooling rates, which in turn can improve polymer diffusion to the inter-filament interface. The study didn't present the impact of thermal history on the mechanical properties of the samples and thus more work is needed in this field to bridge the gap between thermal properties of material, thermal history during printing and the resulting mechanical properties. [44]

Another phenomenon that is critical to the success of FDM printing technology and its progress in large scale manufacturing is potentially catastrophic warping and poor dimensional stability. Due to fast heating and cooling cycles of the material during printing, thermal gradients established during printing lead to trapped residual stress and poor dimensional accuracy. The magnitude of residual stress built up during printing and the influence of material thermal history on such warping phenomena is not well understood. Recent work by Peterson et al. studied the residual stress in ABS and its correlation with layer thickness. Their study reported residual stresses up to 20%. The residual stress also decreased with

increasing layer thickness.[47] This tie between layer thickness and residual stress suggests an impact of residual stress on thermal history and properties that is not fully understood in most recent studies. The material thermal properties and impact of applied shear stress on polymer packing and residual stress needs further experimental work and a more thorough understanding.

Nanoscale Additives for 3D Printing

Graphene

As a new promising material, graphene has received substantial attention recently where the number of publications on graphene-based nanocomposites continues to steadily increase. Due to the exceptional properties that graphene exhibits, the material is considered a promising candidate for a wide variety of applications including components in Li-ion batteries, solar photovoltaics, nano electronics and the aerospace industry. The 2-D material with a honey comb flat structure exhibits a pure sp^2 hybridization network as shown in Figure 1.4.[48] The unusual aspect ratio of graphene is a key factor in its interesting properties. The graphene sheet is the thinnest known material with a theoretical van der Waal thickness of 0.34 nm leading to high intrinsic flexibility. Graphene is distinguished from graphite based of the number of layers. Consequently, characterization tools are needed to distinguish between the different allotropes of carbon. A monolayer and few layer graphene have superior and unusual appealing properties such as the quantum hall effect, high electron mobility and thermal conductivity.[49]

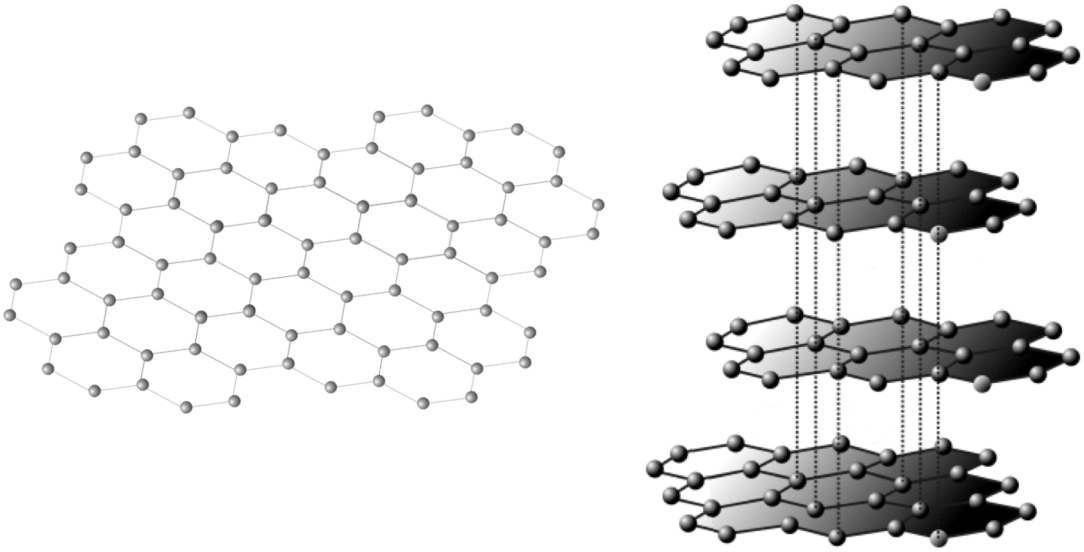

Figure 1.4: Honeycomb structure of monolayer and few Layer graphene showing sp^2 hybridization network and graphene stacking.

To distinguish the number of layers within graphene, and evaluate the extent of defects present in a given sample, several techniques have been developed, among which Raman is one of the most powerful and widely established. Three different peaks can be distinguished within a graphene Raman spectrum. The D peak is at 1320 to 1350 cm^{-1}, which provides information regarding the defects present within the sheets. The G peak is at (1580 to 1605 cm^{-1}) and 2D band is at (2640 to 2680 cm^{-1}). The relative intensities of the D and G deliver information about defects as well and thus it can be used to differentiate between graphene and graphene oxides. Graphene oxide usually shows higher ratio for I_D to I_G. Moreover, the number of layers of graphene present in a sample can be determined based of the position of the 2D Lorentzian peak. For a monolayer graphene, the 2D Peak is present at 2679 cm^{-1}. For a multilayer graphene, the 2D peak moves to higher wavenumber and becomes broader as shown in Figure 1.5. Other prominent features of the graphene Raman spectrum are the ratio of the peak height for G and 2D peaks which is roughly 0.5 for monolayer graphene and increases as the number of layers increases. Figure 1.6 shows the Raman spectrum and AFM image for graphene used in the study. [48,50]

The extraordinary characteristics of graphene include its high thermal conductivity of $5.1x10^3$ $Wm^{-1}k^{-1}$, the highest known intrinsic electric conductivity of $6x10^5$ S m^{-1} and the highest elastic modulus of 1TPa. These properties render graphene as a very promising candidate for polymer reinforcement. To translate these unusual assets to the polymer matrix, a control over dispersion and

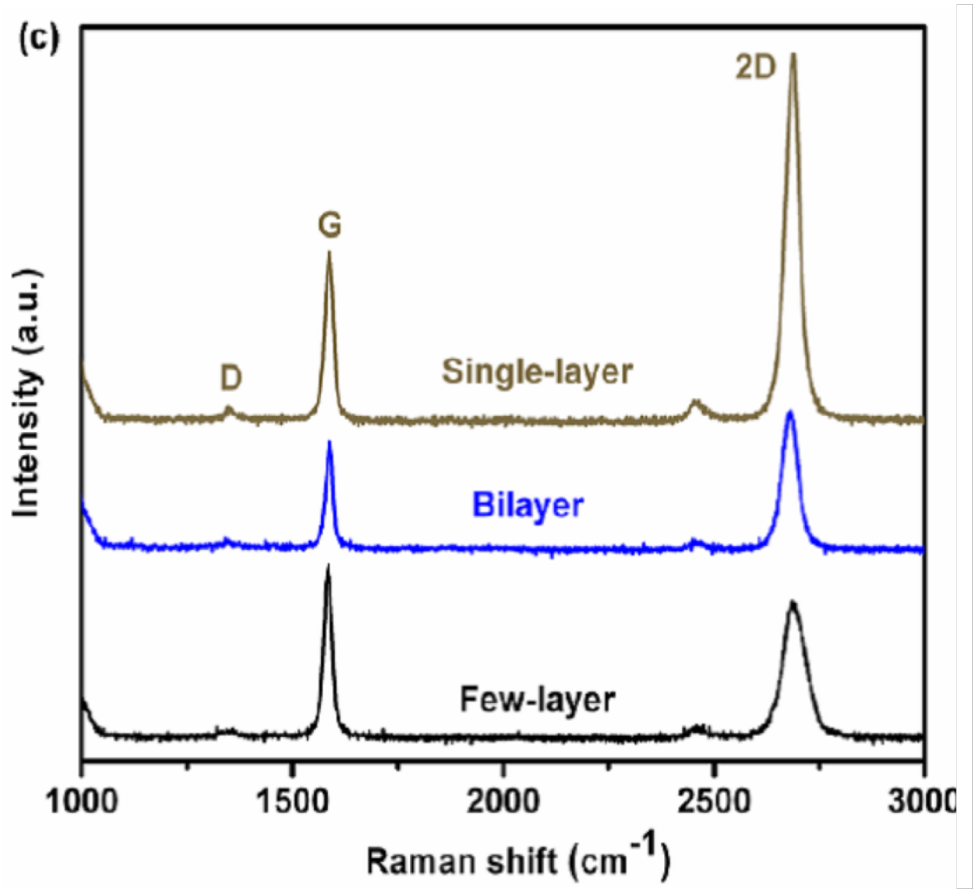

Figure 1.5: 2D Peak shift in Raman spectrum based of the layer number in graphene sample. The peak shifts to higher wave number and become broader as the number of layers increases.[50]

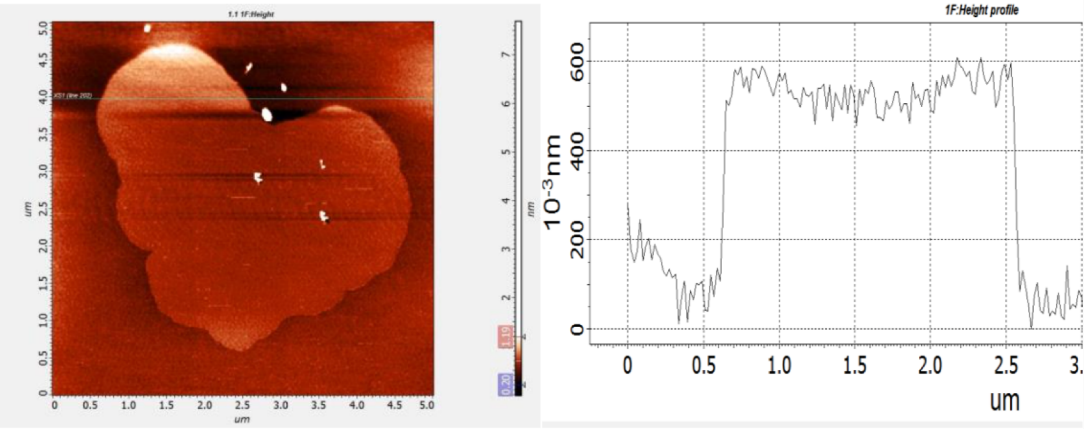

(a)

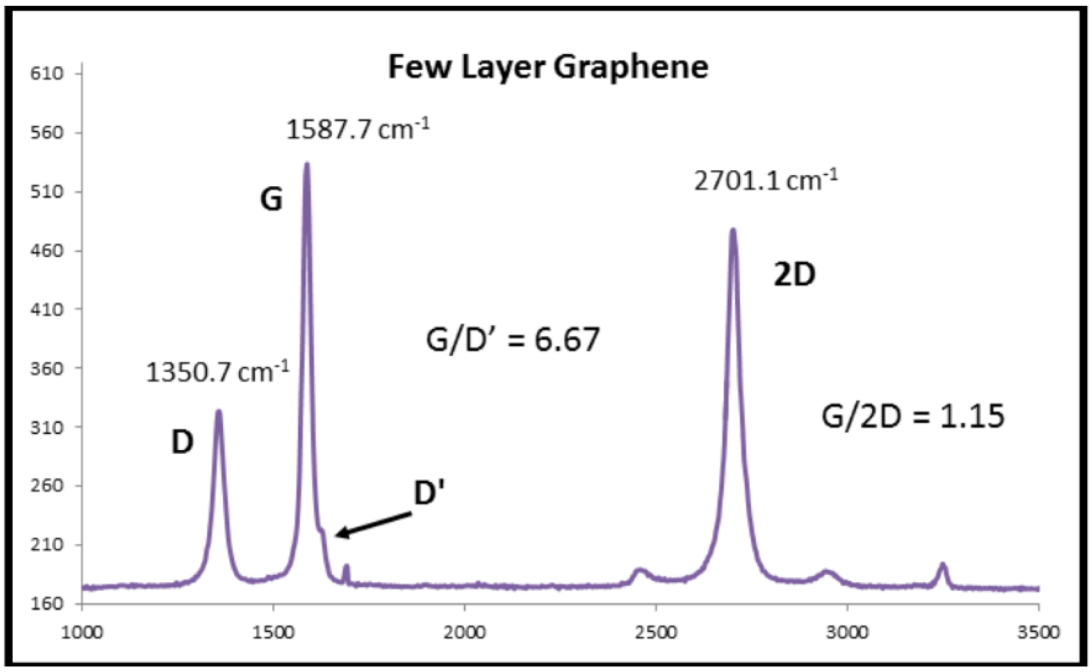

(b)

Figure 1.6: (a) AFM image and thickness of graphene utilized in the study. (b) Raman spectrum showing G/2D ratio.[50]

interactions between the graphene and the linear polymer matrix is critical.[49] The interactions between the polymer and graphene play a key role in translating favorable properties onto the matrix. Common interactions present between graphene and the polymer include weak Van der Waals forces, π-π stacking, and hydrophobic-hydrophobic interactions. Van der Waals forces arise due to transient and permanent dipole moments and are considered weak forces. Due to large specific surface area, the weak Van der Waals forces still contribute significantly to interfacial strength. π-π stacking is also another major contributor to strength and arises from the electron rich aromatic nature of graphene. π-π stacking is especially important for polymers with phenyl rings where it provides a method for strong bonding between polymer and graphene and enhances intermolecular interactions between the nanoparticle and the polymer. [51]

Polymer nanocomposites fabricated by traditional solution casting and melt mixing rely on surface interactions between nanoparticle and polymer to enhance miscibility and dispersion. The oxidation of graphene to form graphene oxide is often used to introduce favorable polar functionalities such as carbonyl, hydroxyl and carboxyl groups, which can form interactions with the polymer to enhance in the matrix. Introducing hydrogen bonding and electrostatic interaction between graphene and the polymer matrix through graphene oxidation can lead to great enhancements of mechanical properties. However, the oxidation deteriorates the thermal and electrical properties of the graphene due to the disruption in the sp^2 network and its aromatic nature by introduction of defects. Consequently, the

reduction of oxidized graphene is essential to restore its beneficial electrical properties.[52]

Among different fabrication techniques, such as melt mixing and in situ polymerization and grafting of the polymer to the graphene, solution casting is still one of the most versatile and efficient techniques to form polymer graphene nanocomposites. Solution processing requires a common solvent for graphene and the polymer matrix. Graphene sheets are often suspended in the solvent using ultra sonication leading to exfoliation of the sheets. The polymer is then dissolved within the common solvent to maximize dispersion. Common problems with this technique are the challenge of finding a common solvent and the difficulty of solvent removal. Also, restacking of graphene sheets can occur during the solvent evaporation process. To prevent restacking, fast precipitation or coagulation of the composite in water or alcohol can be used. This rapid precipitation method can minimize graphene wrinkling and aggregation within the matrix in comparison with traditional, slower, solvent evaporation methods.[53,54]

Thermal Conductivity Mechanism in Graphene and Nanocomposites

Heat transmission in graphene is carried by phonons and electrons, where the major contribution comes from phonons rather than electrons. Due to the structure of graphene, where all carbon atoms are fixed by a covalent bond to a layer, as the carbon atom comes in contact with a heat source, heat transfers rapidly between atoms through vibrations. The vibrations are translated quickly to different atoms through the strong force of covalent bonds leading to rapid heat

transfer from one position to other by phonon waves.[55,56] This heat transfer process is more complicated in the composite and can be influenced by several factors including polymer crystallinity, orientation of molecules and temperature. In polymers, heat doesn't propagate as a wave within a matrix and thus diffuses more slowly, leading to poor thermal conductivities that are usually within the range of 0.1 to 0.5 Wm^{-1} K^{-1}. Moreover, the high surface area of graphene introduces an abundance of interfaces that can prevent heat transfer and increase thermal resistivity. Due to the mismatch between the thermal transport properties of graphene and the polymer matrix, and poor coupling in vibration modes, phonon scattering at the polymer-graphene interface may occur.[57] To reduce this interfacial effect, the graphene loading and dispersion must be adjusted to establish a continuous network of graphene to provide a pathway that maximizes heat transfer. Several works have confirmed that a percolated graphene network above a particular loading substantially increases thermal conductivity as graphene sheets connect with each other within the matrix to form pathways for heat transfer. This percolation threshold varies with the polymer chemical nature and its crystallinity. Khan et al. studies offered strong evidence for the presence of percolation threshold at concentrations below 0.17 weight fraction. Below the percolation threshold, gaps are present between graphene sheets in the matrix and insufficient contact between graphene sheets limits heat transfer. [58]Li et al have also reported similar behavior in graphene-epoxy composites.[59]

Dissertation Outline and Objective

The dissertation presents work that increases our understanding of the effects of soft nanoparticles on polymer dynamics in all-polymer nanocomposites and the impact of graphene on the thermal and mechanical properties of PLA in fused deposition modeling. The first chapter of the dissertation focuses on understanding the impact of soft nanoparticle concentration on the dynamics of an entangled linear polymer matrix that provides important insight into the relative importance of confinement and chain acceleration in all–polymer nanocomposites. Chapter 2 presents a protocol for quantifying the diffusive motion of the soft nanoparticles in all-polymer nanocomposites and correlate its mobility to topology and morphological characteristics. This chapter discusses the possibility of tailoring dynamics through synthesis control. In chapter 3, the effect of graphene on the thermal transport and inter-filament bonding in 3D printing of PLA is examined. In this study the importance of thermal history of the print environment is determined quantitatively and its effect on the adhesion between PLA filaments and the composites is probed. Additionally, the mechanical properties in different directions are tested. Chapter 4 introduces the residual stress phenomenon associated with FDM prototypes and examines the impact of graphene on stress and irreversible thermal strain of PLA.

`

CHAPTER 2

THE IMPACT OF SOFT NANOPARTICLE CONCENTRATION ON POLYMER CHAIN DIFFUSION IN POLYMER NANOCOMPOSITES

Introduction

Studying the dynamics in polymer nanocomposites and the effect of nanoparticle loading on the dynamics of polymers in nanocomposites has gained significant attention recently.[60,61,62,63] Understanding the nanoscale factors that can alter chain motion in the presence of nanoparticles, such as confinement of the chain or acceleration of local chain motion, is necessary to optimize nanoparticle structure, interaction, and loading to form nanocomposites with targeted properties for prospective applications.[9,64,65] Numerous aspects of the nanoparticle, including nanoparticle shape, size and interaction with the polymer matrix affect its dispersion, local interaction and extent of confinement and thus directly impact the local and global dynamics of the neighboring matrix polymer chains.[7,66,67,31,68] Furthermore, the inherent high surface to volume ratio of the nanoparticle can lead to drastic changes in local and global motion of the polymer chain, a relationship that is still not well understood.[4,5,66,68]

The confinement of the polymer chains by the presence of the nanoparticle is unfavorable thermodynamically, as it reduces the number of conformational states, and thus the entropy of the chain. This entropic penalty impacts a wide range of physical properties including mobility, elasticity and miscibility. The extent of confinement varies with the morphology and size of the nanoparticle, where multiple studies have attempted to further understand the relationship between nanoparticle structure and confinement by simulation and experiment.[69,70,71,72] Simulation studies have shown that the polymer-nanoparticle interaction can have

a great impact on confinement and dynamics. A strong interaction between the nanoparticle and the polymer can lead to a strong decrease in polymer chain motion due to formation of a dead layer as polymer adsorbs to the nanoparticle interface. Such interactions may also have a profound effect on the polymer glass transition temperature (T_g) where a significant increase in T_g can be observed at very low nanoparticle concentration in these systems.[12,73,74] Additionally, the macroscopic properties and mechanical behavior of the nanocomposite can be influenced where the interplay between chain packing, nanoparticle interaction, and local dynamics may be detrimental for mechanical reinforcement.[75,15,2,76,1]

The size of the nanoparticle is also a very interesting aspect that can lead to a drastic shift in predicted properties of the nanocomposite.[77] As the nanoparticle diameter decreases below 10~50 nm, unexpected large changes in polymer nanocomposite structural dynamics is observed. For small nanoparticles (1~2 nm) with moderate interactions, the tunable range of T_g is large and the nanoparticle can accelerate local dynamics due to the dissociation of a few weak physical bonds between the nanoparticle and polymer segments.[9,78,79,80,81]

Another important parameter is nanoparticle softness. Previous studies have shown that macromolecular diffusion in the presence of hard impenetrable nanoparticles can be explained using the Entropic Barrier Model (EBM).[82,83,69,6] In this model, the nanoparticles are seen as obstacles to chain motion that create bottle necks where the polymer chains are confined in order to move in between the nanoparticles. This process reduces the possible chain conformations,

significantly lowering the entropy of the diffusing species. The ability of the EBM to accurately describe the diffusion of polymer chains in the presence of hard impenetrable nanoparticles has been tested and shown to accurately capture the polymer chain matrix diffusion behavior.[83,61]

A series of studies used elastic recoil detection to monitor the effect of nanoparticle shape and size on the dynamics of the polymer chain in a nanocomposite in order to elucidate the influence of confinement and test the EBM experimentally.[61] These studies included the determination of the diffusion coefficient of linear polystyrene in the presence of phenyl capped silica nanoparticles. The results show that the diffusion of the matrix chains decreases with increasing nanoparticle concentration and this reduction is stronger for higher molecular weight polymer chains. With D being the diffusion coefficient of the matrix after incorporation of the nanoparticle and D_0 is the diffusion coefficient of the neat matrix, plotting the reduced diffusion coefficient (D/D_0) as a function of the ratio of the spacing between nanoparticles (ID) and the size of the polymer molecule (2Rg), $ID/2R_g$, provides a master curve where the diffusive behavior of polystyrene in a series of nanocomposites collapse onto one curve. Moreover, the normalized diffusion (D/D_0) decreases rapidly as the confinement parameter (ID/2Rg) approaches ~ 1. This scaling of the diffusion with confinement represents good agreement with the EBM.[83]

In a different study, the effect of nanoparticle shape and anisotropy on polymer chain diffusion in nanocomposites was investigated by examining the

diffusion of deuterated polystyrene (dPS) in a nanocomposite containing string like chained nanoparticles that are grafted with PS chains. The chained particles are composed of 5 spheres of Fe_2O_3 connected to form a cylindrical like structure. This study reports that the presence of these anisotropic nanoparticles results in a minimum in diffusion coefficient of the linear polymer chains with a change in nanoparticle loading when the ratio of the polymer chain and cylinder length $2R_g/L$ is less than 1.5, where R_g is the radius of gyration of the polymer and L is the mean length of cylinder formed by the nanoparticle impenetrable cores.[84] This behavior is not universal, as higher molecular weight polymers exhibit a monotonic decrease in diffusion with nanoparticle concentration, consistent with the trends reported for the diffusion of linear polymer chains in the presence of spherical impenetrable nanoparticles.[61] Interestingly, the relative size of the nanoparticle and matrix polymer chains is a crucial parameter that defines whether the minima in polymer chain diffusion with nanoparticle concentration exists. Mu et al. [63] reported a similar response in polymer nanocomposites that contain multiwall nanotubes, where they found a minimum in polymer diffusion with nanoparticle concentration when the size of the matrix chain, $2R_g$, is larger than the diameter of the multiwall nanotube. The minimum is found near the percolation threshold concentration. They attributed this trend to the anisotropic diffusion of the polymer chain near the anisotropic nanoparticle, where the diffusion along the tube is faster than perpendicular to it. Consequently, the continuous path along the nanotube leads to the recovery of a more rapid diffusion above the percolation threshold.

Most previous studies have focused on nanocomposites that contain hard impenetrable nanoparticles or semi-soft nanoparticles that are composed of hard impenetrable core with grafted polymer brushes at the nanoparticle surface.[61,63,85] However, the diffusive behavior of polymer chains in the presence of soft, penetrable organic nanoparticles has been studied less frequently. The diffusive behavior of a polymer chain in the presence of polymer based nanoparticles can be tremendously different as the interaction of the polymer chain and nanoparticle is fundamentally different.[86] The polymer chain may entangle with the nanoparticle, and the interface between nanoparticle and polymer chain is more diffuse. This broad interface means that the depletion of entropy that occurs in nanocomposites with hard nanoparticles is mitigated, and potentially eliminated, in these systems. For instance, previous studies in our group found that the addition of 1% PS soft nanoparticles into 535K linear PS approximately doubles the diffusion coefficient of the polymer chain.[87] Further studies also confirmed that the increase in polymer chain diffusion is not accompanied with an increase in free volume since a very moderate increase in T_g was observed with the inclusion of the nanoparticles. Consequently, simple plasticization of the chain is not the primary mechanism for this increase. The increase in polymer chain diffusion is attributed to the nanoparticle topology that enables a constraint release mechanism in the polymer motion and speeds up diffusion of the matrix.[87] This is interesting as an increase in polymer chain diffusion with the addition of nanoparticles is not commonly observed in polymer nanocomposites. Most studies indicate that the addition of

the nanoparticle acts as an obstacle to polymer diffusion, regardless of its topology and degree of softness.[62,10,6] To more fully understand this unique response, we have monitored the diffusion coefficient of linear polystyrene in the presence of soft nanoparticles as a function of nanoparticle concentration. The goal of these studies is to elucidate the relative importance of the interaction between the polymer chain and nanoparticle, and potential confinement of the polymer chain motion by the nanoparticle in controlling the polymer chain diffusion.

In this study we monitor the diffusion of 535K linear PS as a function of nanoparticle concentration for a lightly crosslinked (~1%) soft polystyrene nanoparticle. This nanoparticle has been shown to consist of a gel like cross linked core with a fuzzy surface of PS chain ends.[33] The molecular weight of the nanoparticle (NP1B) is 238K, which is 2 times lower than the matrix and is ~20 nm in diameter, which is larger than the reptation tube diameter. Furthermore, we examine the importance of confinement by comparing our results to the entropic barrier model to provide a better understanding of the relationship between nanoparticle topology, size of the nanoparticle, and confinement. The study is performed using in-situ real time neutron reflectivity which allows the continuous acquisition of reflectivity profiles while annealing at elevated temperatures to ensure the system attains center of mass diffusion and allows the accurate determination of Fickian diffusion coefficients.

Experimental

Bilayer samples of deuterated and protonated PS 535,000 Daltons (535K) with identical nanoparticle loading were prepared using spin casting. The mass fractions of the nanoparticles were 0.5, 1, 2, 3 and 5%. A control sample that consists of a bilayer of neat deuterated and neat protonated polystyrene was also examined to obtain the diffusion coefficient of the neat linear polystyrene. The protonated and deuterated polystyrene were purchased from Polymer Source. The polymers have number and weight average molecular weights of 535K and 540 K and polydispersity of 1.09. The soft polystyrene nanoparticle used for this study is denoted as NP1B, with a structure that is known to consist of a crosslinked core with a fuzzy interface[33]. Structural characteristics of the nanoparticle are presented in Table 2.1. This nanoparticle was synthesized using semi batch emulsion polymerization where the rate of monomer addition was controlled and maintained at 2ml per hour.

All Si wafers were purchased from Wafer World. Prior to deposition of the bilayer, the Si wafers were cleaned in piranha solution, which is a mixture of sulfuric acid and hydrogen peroxide in the ratio of (3:1). The wafers were then rinsed in deionized water and dried by a stream of dry nitrogen. To further remove any organic contaminants and regrow the oxide layer, the wafers were placed in a UV/Ozone environment for 15 minutes. The solutions used for spin casting were all prepared using toluene at 1% concentration. To form the bilayers, the protonated solution was spun cast onto 2 inch diameter wafer while the deuterated

Table 2.1: Structural characteristics of the NP1B nanoparticle as determined from small angle neutron scattering (SANS).[33]

Rate of monomer addition (ml/hr)	2
DVB cross linker (mol%)	0.81
M_W (x10^6)	0.238
R_g (nm) [a]	10.1
R_h (nm)[b]	18
R_g/R_h	0.56
R_c[c]	3.46
τ_{fuzzy} (nm)[d]	4.62
R_p(nm)[e]	12.69
σ[f]	0.36

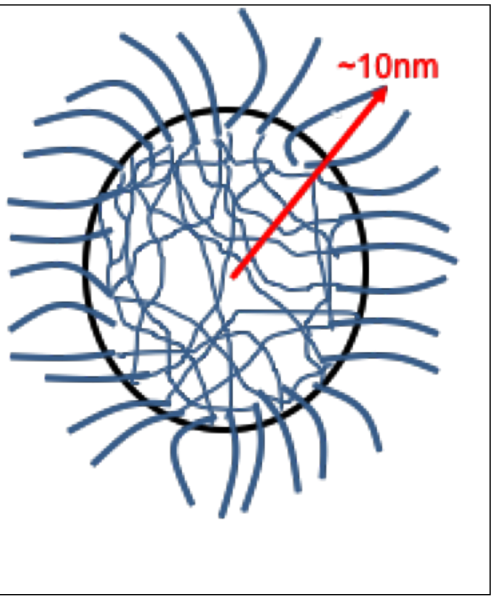

[a] Radius of gyration

[b] Hydrodynamic radius

[c] Radius of the core

[d] Half width of fuzzy interface

[e] R_c+2 τ_{fuzzy}

[f] τ_{fuzzy}/R_p

solution was spun cast to a 4-inch wafer. The deuterated film was then floated on a bath of water and picked up by the protonated film to create the bilayer. All spin casting was completed at 2000 rpm for 30 seconds. With these spin coating parameters, the thicknesses of the films were between 70 to 90 nm.

Ellipsometry is used to estimate the thickness of the spin cast layers, which serve as a baseline for the neutron fitting procedure. All bilayers were kept in a vacuum oven for 24 hours at room temperature after fabrication to remove any residual water or solvent. Neutron reflectivity experiments were then performed using in-situ real time reflectivity at NIST. A temperature controlled box was used to in-situ anneal the samples while acquiring the reflectivity curves. This is better than the annealing and quenching method that is a technically slow process where errors might arise due to adjusting the vacuum oven for each annealing time and continual heating and cooling of the sample. Thus, the reflectivity profiles of the samples were monitored while the sample was in the temperature controlled chamber at 130°C. A reflectivity profile of the as-cast sample was initially collected at 90°C, after which the temperature of the sample was quickly (less than 5 minutes) raised to 130°C with no overshoot and reflectivity curves were then collected every 15 minutes for 4 hours.

The reflectivity of the sample was then plotted as function of q_Z, the scattering vector perpendicular to the surface of the samples; defined by the following equation:

$$q_Z=(4\pi/\lambda)\sin\theta \qquad \text{Equation 2.1}$$

In this equation, θ is the angle of incidence and λ is the wavelength of the incident neutrons. The interaction of the layered material with neutrons is further explained by the rules of optics. Neutrons reflect and refract at the interfaces due to differences in refractive indices as shown in Figure 2.1. [88]

The neutron refractive index of the material is:

$$n = 1 - \delta + i\beta \qquad \text{Equation 2.2}$$

where β is the imaginary part of the refractive index and represents the neutron absorption and can be neglected. δ represents the real part and can be described using Equation 2.3:

$$\delta = \frac{N_A \rho}{2\pi} \lambda^2 \frac{b_{mon}}{M_{mon}} \qquad \text{Equation 2.3}$$

where N_A is Avogadro's number, λ is the incident wavelength of radiation, ρ is the mass density of the monomer, b_{mon} is the neutron scattering length of the monomer, and M_{mon} is the molecular weight of the monomer. Thus, the neutron refractive index of the material is dependent on the neutron scattering length of the material. The scattering length denotes how strongly a material scatters neutrons and is isotope dependent.[89,20]

All data were reduced and fitted using the analysis package MOTO FIT in IGOR PRO. The reflectivity curves provide information about the composition of the film as a function of depth, and thus provides a depth profile of the film. The scattering length density (SLD) and thickness of the layers and roughness between

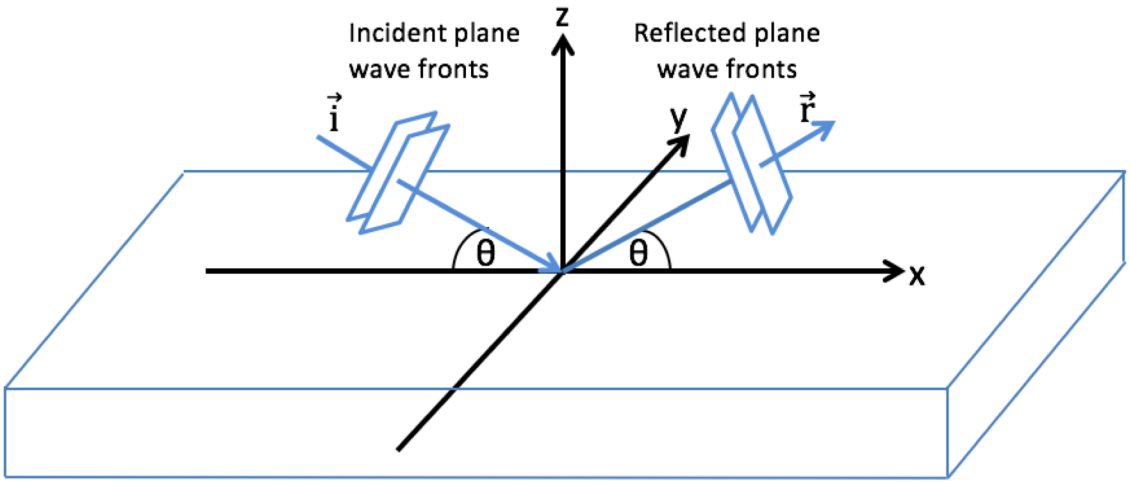

Figure 2.1: Diagram illustrating the reflection of Neutrons at an interface.

layers were all fine-tuned to provide the best fit to the reflectivity curves. The quality of the fitting was assessed statistically through the value of χ^2 that was less than 10 for all analyses. A mass balance check was performed by integrating the area under the SLD profiles for the as-cast and the annealed samples assuring that the variation did not exceed 5%. [89,90]

Results and Discussion

Figure 2.2 shows representative reflectivity profiles for the dPS/PS bilayer with 0.5% nanoparticle loading for the as-cast sample and the sample after annealing for 5211 seconds at 130°C. Fifteen reflectivity curves were acquired over the 4 hours of annealing, but Figure 2.2 only shows 8 curves for clarity. Three representative features of the reflectivity curves correlate to the structural features of the bilayer: the critical angle below which there is total reflection, the distance between minima, and the intensity of the oscillations. The critical angle of the sample correlates to the chemical composition of the top surface, and doesn't change with annealing as shown in Figure 2.2. This makes sense as the changes in depth profile of the bilayer occurs in the bulk of the film around the deuterated polystyrene/protonated polystyrene interface and not at the top or bottom of the layer. The distance between minima is correlated to the thickness of the layers and total film, which show small changes (3-5%) throughout the annealing process. These changes in film thickness with annealing are attributed to relaxation of the polymer from the non-equilibrium spin-cast sample towards equilibrium conformations. Finally, the intensity of reflectivity oscillations correlates to the

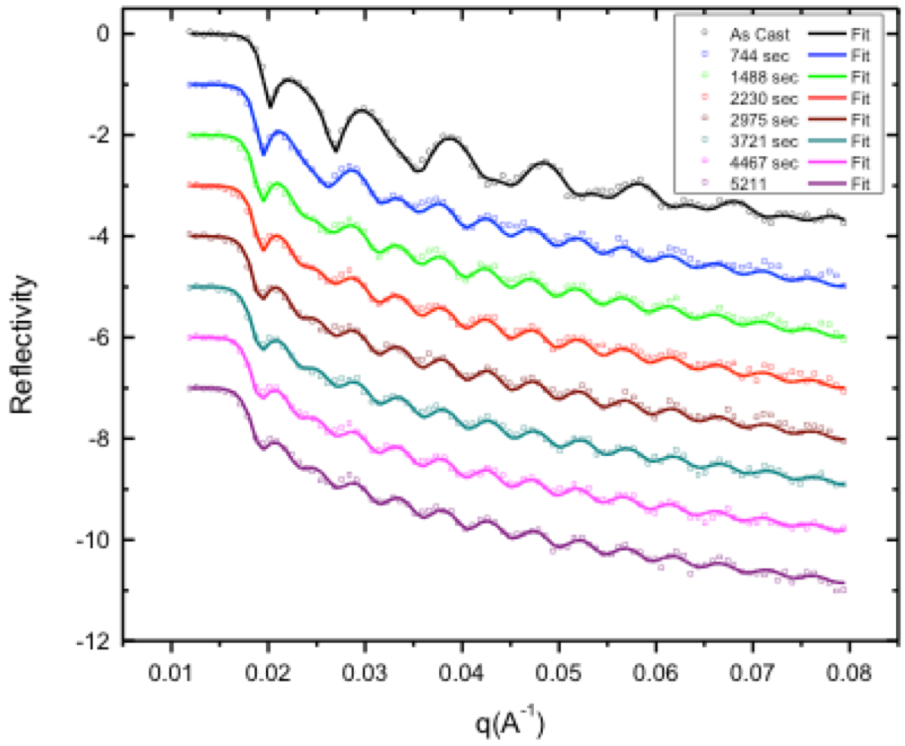

Figure 2.2: Representative reflectivity curves for dPS /PS with 0.5% NP1B loading annealed at 130°C.

roughness of the interfaces in the bilyaer.[91] The intensity clearly decreases with annealing, correlating to intermixing and diffusion of polymers between the two layers. Figure 2.3 shows the SLD profiles of the dPS/PS bilayer with 0.5% SNP loading at different annealing times. The SLD profiles show a symmetric transition where both protonated and deuterated polymers inter-diffuse at the same rate. The SLD profiles are further analyzed to monitor the change in the volume fraction of each component with annealing time, where the SLD profile is translated to a volume fraction depth profile using Equation 2.4.[87]

$$\phi_d(z) = 1 - \frac{SLD_d - SLD_x(z)}{SLD_d - SLD_H} \qquad \text{Equation 2.4}$$

In this equation, $\phi_d(z)$ is the volume fraction of the deuterated component at depth *z*, SLD_d is the scattering length density of the dPS, SLD_H is the scattering length density of protonated PS. $SLD_X(z)$ denotes the scattering length density of the sample at depth *z* at a given annealing time. To further obtain the mutual diffusion coefficient, the volume fraction profiles are fitted to the one-dimension solution of Fick's second law as shown in Equation 2.5.[63,83]

$$\phi_d(z) = \frac{1}{2} c_0 \left[\mathrm{erf}\left(\frac{h - z}{\sqrt{4 D_m t}} \right) + \mathrm{erf}\left(\frac{h + z}{\sqrt{4 D_m t}} \right) \right] \qquad \text{Equation 2.5}$$

In this equation, *t* is the annealing time in seconds while *h* is the dPS thickness. Figure 2.4 shows the fitting of the volume fraction profile to Equation 2.5 for the neat polymer at 8160 seconds of annealing at 130 °C. The calculated mutual diffusion for the neat polymer determined from these fits is then plotted as a

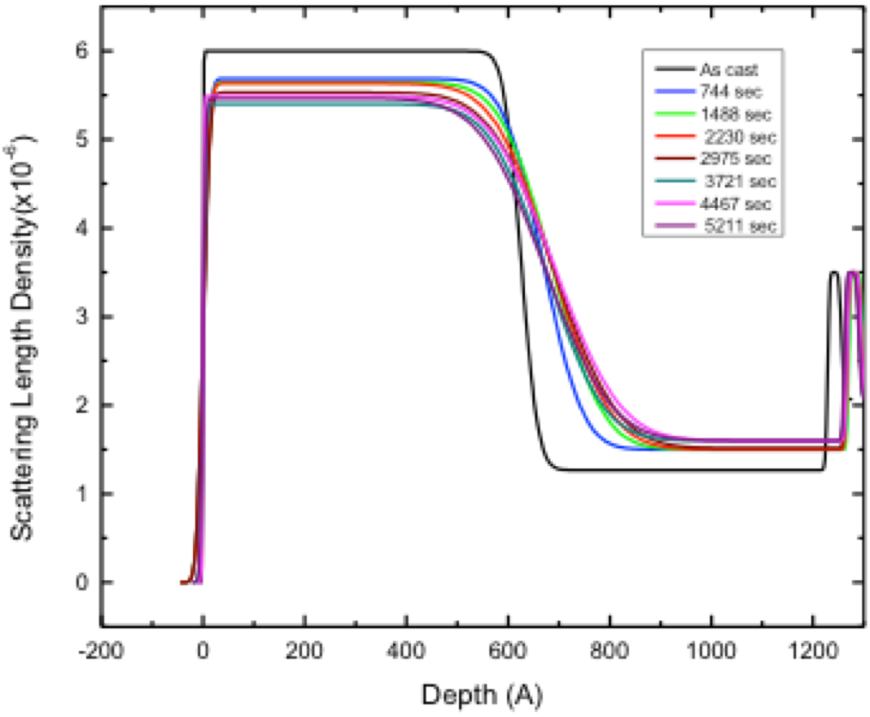

Figure 2.3: Representative SLD profiles of the dPS/PS bilayer with 0.5 %NP1B loading annealed at 130°C.

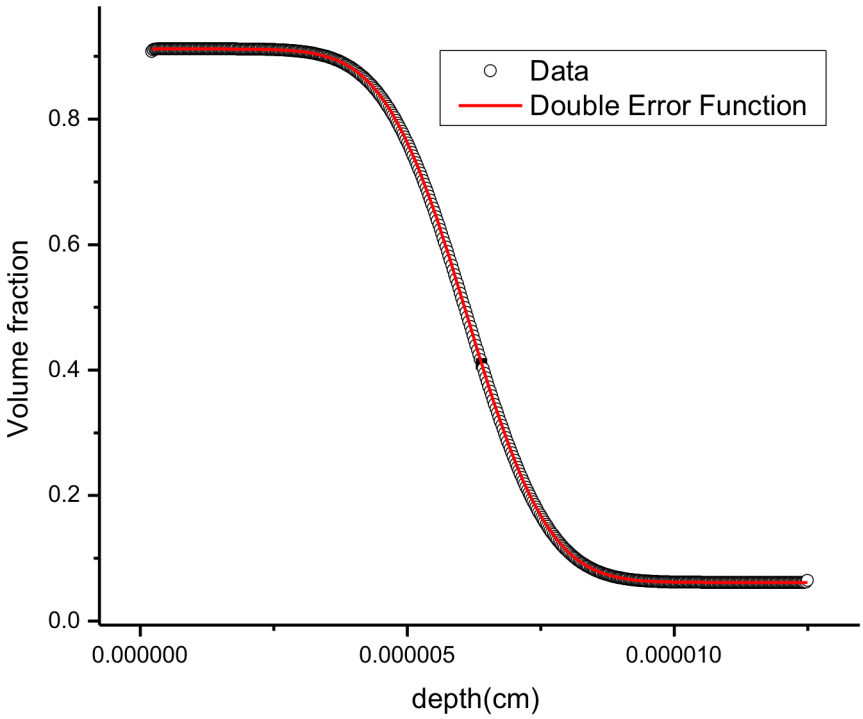

Figure 2.4: Volume fraction fitting to double error function for control at 8160 seconds.

function of annealing time in Figure 2.5. The nominal diffusion coefficient decreases rapidly with short annealing times and levels off around ~6000 seconds. This behavior occurs because at early times, the polymer has not reached the diffusive regime, and the changes in the depth profile are monitoring local, Rouse-like motions, rather than center of mass diffusion. Thus, the values provided at these early times are not accurate diffusion coefficients. It is only at long annealing times (> ~ 6000 – 7000 s) that the diffusion coefficient levels off with annealing time, which indicates that the polymer has attained diffusive motion.

Several previous studies have confirmed the hierarchal manner of the dynamics of entangled polymers where polymers obey the Rouse model at short times, and transition to reptation dynamics model at longer times.[92,93,94] In the reptation domain, the diffusion coefficient varies with molecular weight, M, as M^{-2}.[87] The reptation model describes the motion of a polymer chain that is restricted to a tube imposed by the confinement of surrounding chains. In this model, the reptation time, τ_r, represents the time required for the chains to escape the tube.[60]

The diffusion coefficient of the neat polymer as determined from this analysis is 8.07 $x10^{-17}$ cm^2/second. A self-consistent check of this analysis can be completed by monitoring the change in the interfacial width between the PS and dPS as a function of annealing time. The interfacial width increases with the mean square displacement of the polymer across the interface, which can be monitored by following the change in interfacial roughness. Equation 2.6 shows the

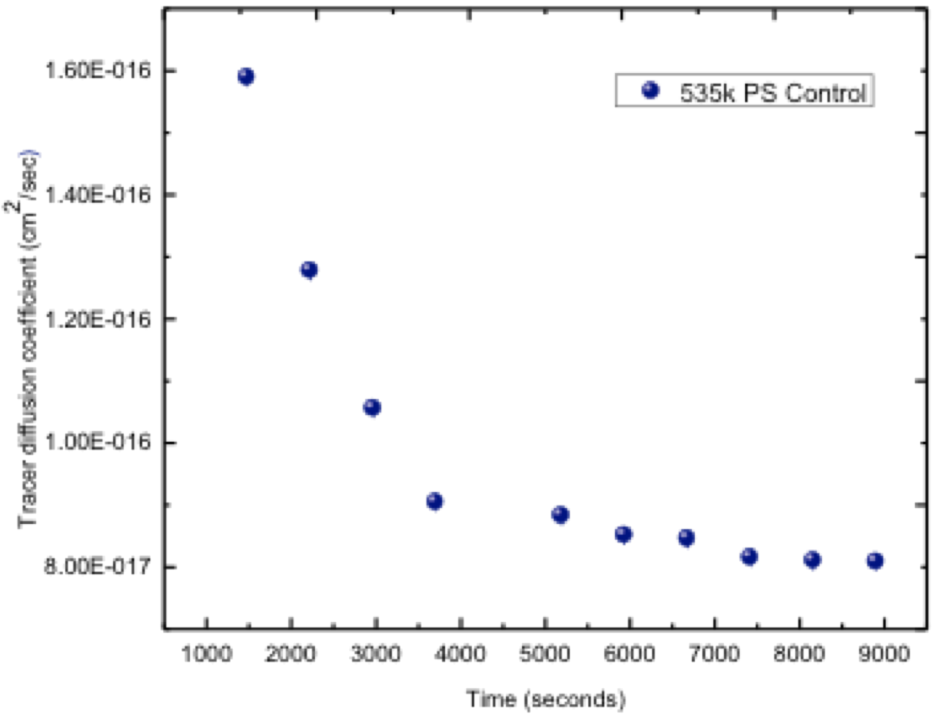

Figure 2.5: Tracer diffusion coefficients versus annealing time for control dPS/PS.

relationship between the interfacial width, W, and the interfacial roughness, σ, that is determined from the fit of the reflectivity profile.[20]

$$W = (2\pi)^{1/2}\,\sigma \qquad \text{Equation 2.6}$$

Figure 2.6 shows the log-log plot of the interfacial width as a function of annealing time for the neat polymer. The interfacial width shows the expected $t^{1/4}$ dependence at early times, which transforms to $t^{1/2}$ for longer annealing times. This transition is consistent with a transformation from Rouse dynamics to the reptation regime. The transition to reptation dynamics with this analysis is consistent with the leveling off of the diffusion coefficient in Figure 2.5, verifying the validity of both analyses. The slope in the $t^{1/2}$ regime is then used to calculate diffusion coefficient providing a value of 8.5 $X10^{-17}cm^2$/second, consistent with the value reported from the data in Figure 2.5.

We further check the diffusion coefficient of the neat polymer by comparing it to other diffusion coefficients of polystyrene that are reported in literature. Unfortunately, there are few studies that have monitored the diffusion of polystyrene at 130°C at similar molecular weights, and thus we must correct the literature values for differences in annealing temperatures and molecular weight. Equations 2.7 is used to account for variations in temperature while Equation 2.8 accounts for variation in polystyrene molecular weight.

$$D_2 = D_1 \left(\frac{T_2}{T_1}\right) exp\left[2.3B\left(\frac{1}{T_1 - T_\infty}\right) - \left(\frac{1}{T_2 - T_\infty}\right)\right] \qquad \text{Equation 2.7}$$

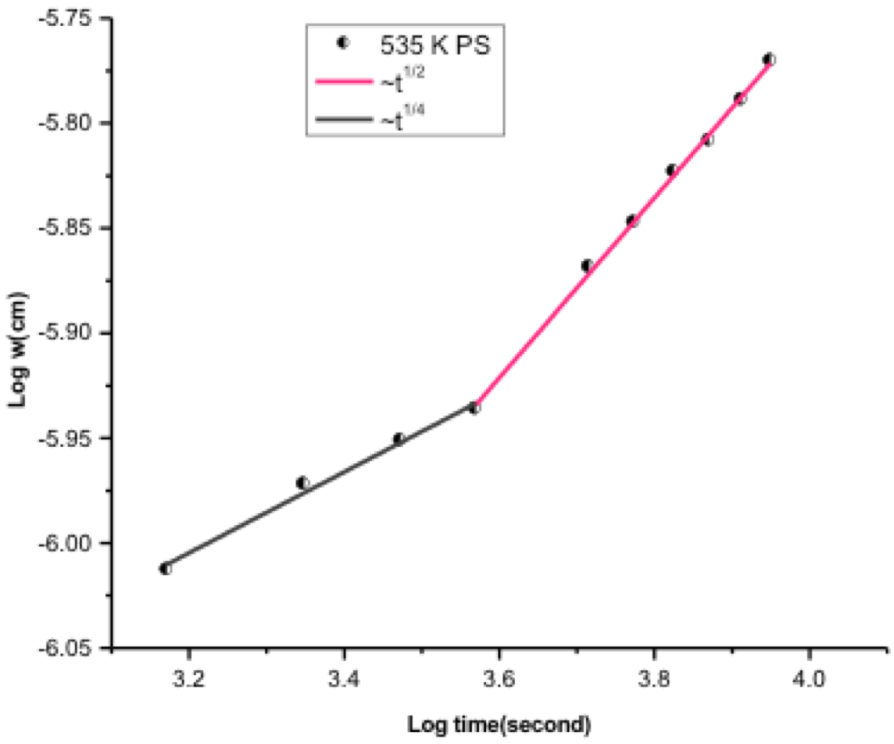

Figure 2.6: Plot of the change in the interfacial width between PS and dPS in the neat bilayer as a function of annealing time.

$$D_2 \sim D_0 M^{-2}$$ Equation 2.8

In Equations 2.7 and 2.8, T_2 and T_1 are the two temperatures at which diffusion is monitored. T_∞ is the Vogel temperature of 322K and constant B=983K while M is the polystyrene molecular weight.[63]

Our results are consistent with these values reported in the literature and the diffusion coefficient reported by Karim et al.[95] for PS (5.45×10^{-18} cm^2/second) at 120°C and M_w of 233K. After correcting for molecular weight and temperature differences, the diffusion coefficient from Karim's study is 8.7×10^{-17} cm^2/second at 130°C for 535 K compared to 8.07 $\times 10^{-17}$ cm^2/second obtained from our experiment. The similarity in these values provides additional validation that the experiment and that the described analyses accurately monitor the diffusion coefficients of polystyrene in the neat sample and in the nanocomposites.

Figure 2.7 shows the diffusion coefficient for the polystyrene chain in the neat sample and the nanocomposites with different nanoparticle loading. The diffusion coefficient increases at low nanoparticle concentrations, for instance it increases from 8.07 $\times 10^{-17}$ for the neat polymer to 1.35 $\times 10^{-16}$ for the 0.5% nanoparticle nanocomposite and increases further for the sample with 1% nanoparticle loading. Overall, the diffusion coefficient increases by a factor of 2 for the sample with 1% nanoparticle loading. Above 1%, denoted as φ critical, the diffusion coefficient decreases steadily with increasing concentration and approximately retrieves the diffusion of the neat polymer at 5% loading. In order to

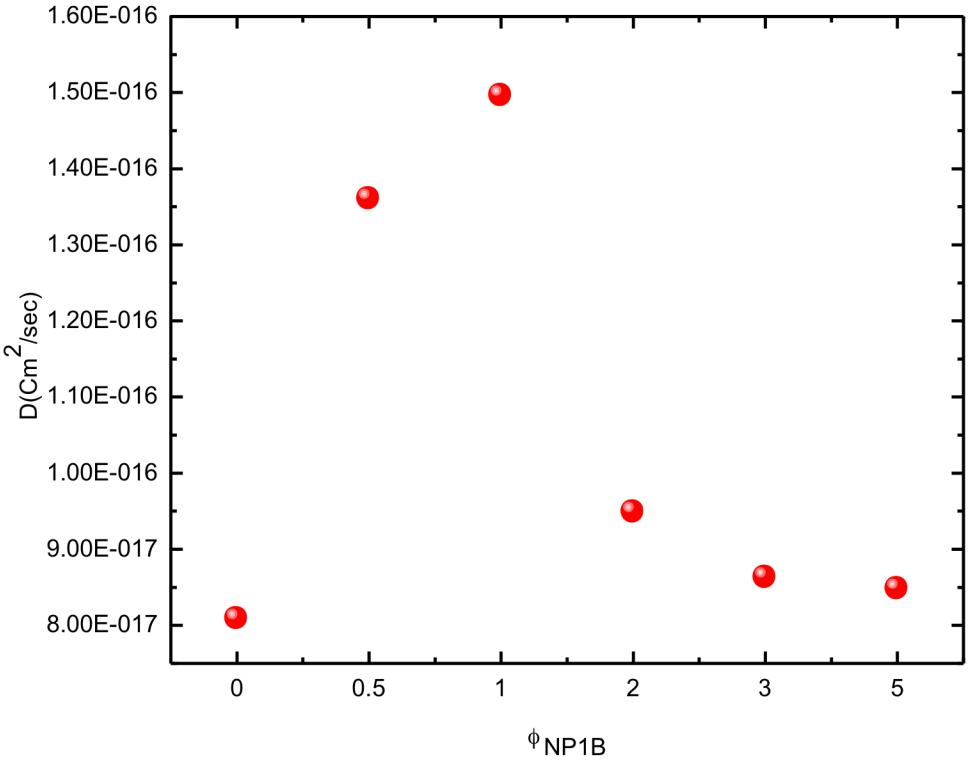

Figure 2.7: Diffusion coefficient for neat polymer and nanocomposites with different NP1B loading.

explain the speed up in diffusion below φ critical, we invoke the idea of constraint release. As we have previously discussed, the nanoparticle interface includes a corona of short chain ends. These chain ends move faster than the reptating polymer, which provides a mechanism for entanglements to vanish before the polymer reptates through the whole tube, thus the reptation tube is altered and the motion of the polymer chain speeds up.[87] This interpretation is also consistent with the motion of polymer chains in the presence of star polymers.

In order to gain additional insight into the relationship between the soft nanoparticle loading and confinement, and interpret the results above ϕ critical, we further apply the entropy barrier model that explains polymer dynamics near obstacles and has successfully described polymer diffusion through porous glasses and gels[3]. The model defines the nanoparticles as an impenetrable barrier that separates accessible cavities as illustrated in Figure 2.8. The polymer chains have more entropy when they exist inside the cavities due to the freedom to adopt a larger number of configurations. As the chain moves from one cavity to a different one, it passes through a bottle neck where it is confined, reducing its entropy. Consequently, the bottle necks are seen as entropic barriers through which the polymer has to squeeze in order to diffuse via the paths between nanoparticles, while the cavities act as entropic traps.[82,83] It is important to note that there are several assumptions proposed within the model. First, the bottle neck formed in between particles is short enough to be dominated by the entropic barrier. Second, the enthalpic interactions are minimized, and finally the distance between traps

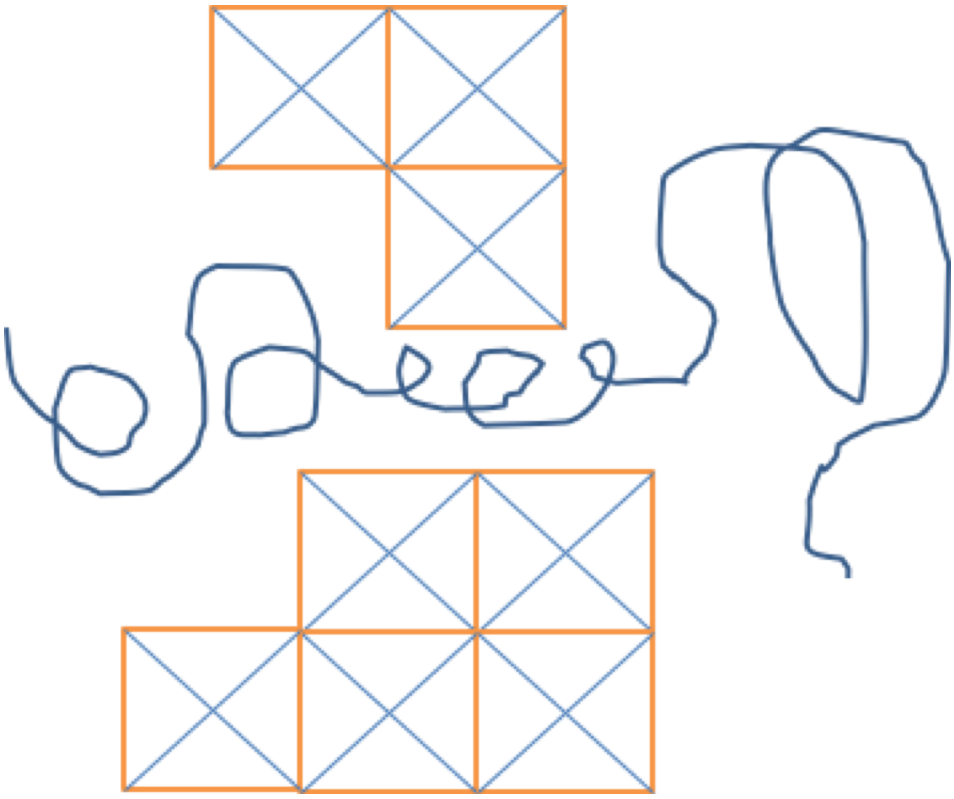

Figure 2.8: An illustration to depict cages and bottle necks as presented by the entropic barrier model.[82]

(ID) is considered fixed and can be estimated using Equation 2.9 [83]

$$ID = d[\left(\frac{2}{\pi\varphi_{NP}}\right)^{\frac{1}{3}} - 1] \qquad \text{Equation 2.9}$$

where *d* denotes the diameter of the nanoparticle and φ_{NP} is the volume fraction of the nanoparticle. The confinement parameter is then defined as a ratio between ID and the diameter of gyration of the polymer matrix ($2R_g$) and defines the available volume of the melt for polymer chains to diffuse between nanoparticles. Plotting the reduced diffusion (D/D_o) as a function of the confinement parameter results in a curve for polymer chain diffusion among hard impenetrable nanoparticles.[2,3] It is clear that our results don't follow this model at low concentrations, since the diffusion rate is increased. However, at higher nanoparticle concentration, the polymer chain diffusion decreases to approach that of the neat polymer chain, and the entropy barrier model may provide some insight to this change in diffusion behavior. Thus, to further interpret our data, we calculate the inter particle distance for our system using Equation 2.10 where the diameter of the nanoparticle is known from previous SANS experiments to be ~20nm.[33] To estimate the confinement parameter, we calculate R_g of the linear polystyrene matrix using the following equation[87]

$$Rg = \frac{a\sqrt{N}}{\sqrt{6}} \qquad \text{Equation 2.10}$$

where N is the degree of polymerization and *a* is the statistical segment length (0.67 nm for PS), where R_g is estimated to be 20 nm. Figure 2.9 shows a plot of

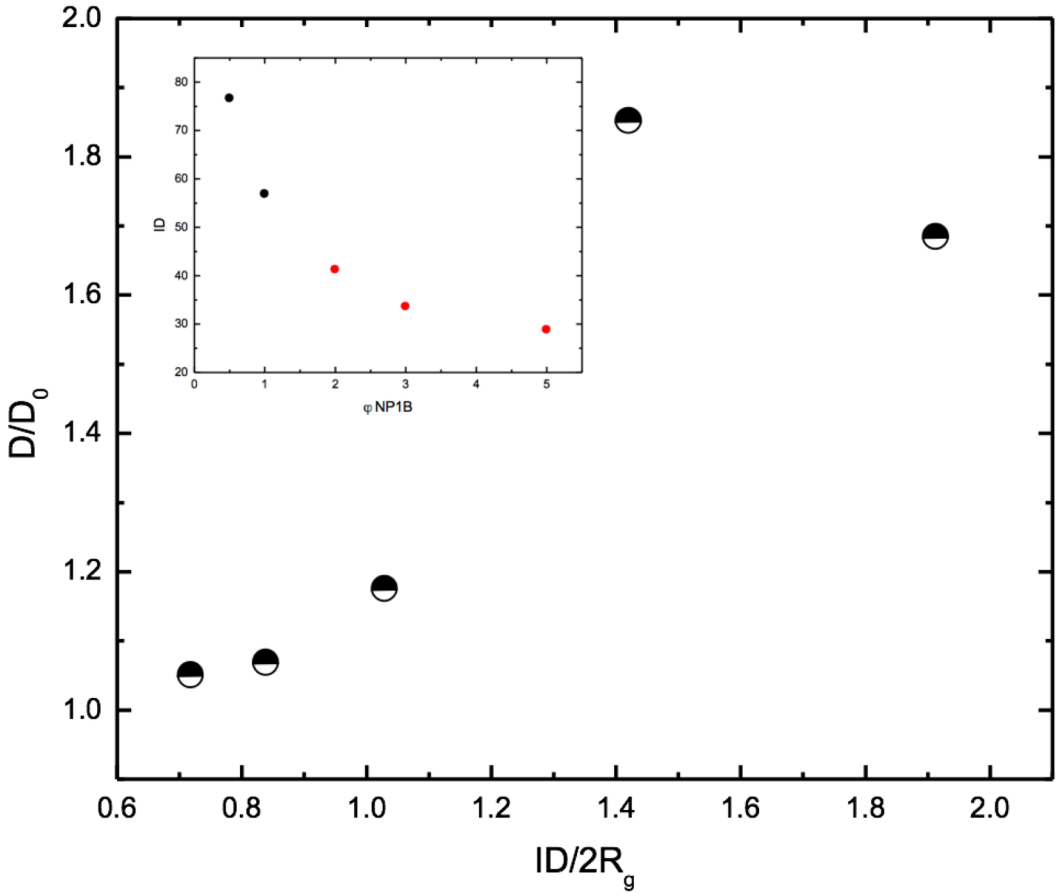

Figure 2.9: Reduced diffusion coefficient as a function of the confinement parameter for different NP1B loadings.

the reduced diffusion of the linear polymer chain D/D_o as a function of the confinement parameter $ID/2R_g$., where the inset shows the change in ID with nanoparticle loading. Inspection of this plot shows that at low nanoparticle loadings (0.5% and 1%) $ID/2R_g$ is much greater than one, which suggests the linear polymer chains are not confined in their motion. At higher nanoparticle loadings (> 2%), $ID/2R_g$ approaches and becomes smaller than one, indicating that the motion of the polymer begins to become confined.

It is interesting that the diffusive behavior of the polymer chain also appears to transition when the distance between nanoparticles is similar to the size of the polymer chain ($ID/2R_g \sim 1$). Absent confinement effects, the diffusion of the polymer chain is enhanced by the presence of the soft nanoparticles, presumably by a constraint release mechanism. As the pathways for diffusion become smaller with more nanoparticles, this enhancement appears to be mitigated by the confinement which results in an attenuation of the increase in diffusion so that the motion of the polymer chain at higher nanoparticle loadings is similar to that of the neat polymer. It is worth emphasizing that these results do not show a diffusion of the polymer chain that is slower than that of the neat polymer, a common response of the motion of polymer chains in the presence of hard impenetrable nanoparticles. Rather the balance of the beneficial constraint release and adverse confining effects are on the same magnitude and essentially cancel each other out at higher nanoparticle loading, with the enhancing effects slightly outweighing the attenuating confining forces.

Conclusion

We investigate the dynamics of polymer nanocomposites with varying soft nanoparticle loadings using in-situ real time neutron reflectivity. Our results show that the diffusion coefficient of linear PS matrix increases by a factor of 2 with the nanoparticle loading below 1% however, above 1% the diffusion of the linear chain is attenuated as the nanoparticles confine the polymer chain. Thus at these higher nanoparticle loadings, the diffusion of the linear polymer chain is controlled by the balance of the enhancement of chain motion, presumably by constraint release, and the attenuation of chain motion due to confinement of the polymer by the neighboring nanoparticles.

The fact that the diffusion of the polymer chain in the nanocomposite is never less than that of the neat polymer indicates that the enhancement effects are dominant in determining the diffusion of the linear polymer chain. This is because if the confinement effects dominated, the diffusion of the polymer chain would be slower than that of the neat polymer. The similarity of the diffusion of the polymer chain in the highly loaded nanocomposite and that of the neat polymer suggests that the attenuating confinement effects and enhancement processes are of similar magnitude. Moreover, this behavior in polymer chain diffusion in the presence of nanoparticles is unusual and fundamentally different than what has been reported for nanocomposites with inorganic nanoparticles, suggesting a new venue for these materials where the control of loading can alter the dynamics of the matrix in a distinctive manner.

CHAPTER 3

THE IMPORTANCE OF NANOPARTICLE SOFTNESS ON ITS TRACER DIFFUSION COEFFICIENT IN A LINEAR POLYMER MATRIX

Introduction

With the fourth industrial revolution, there is a growing interest in polymer nanocomposites as a mean of achieving novel materials. A variety of nanoparticles and fillers have been utilized to enhance desired specific properties for a polymeric material leading to its potential application in aerospace, automotive and pharmaceutical industries.[5,15,96,97,51,98] Most current research focuses on hard impenetrable nanoparticles that provide enhancements in mechanical and electrical properties while modifying the polymer dynamic and flow properties.[66,99,60,79] Dispersing these hard nanoparticles has always been a challenging task where aggregate formation and lack of favorable interactions lead to failure in translating the desired improvements onto the polymer matrix. Additionally, difficult processing conditions invoke further obstacles that limit their use.[6,85,2] These challenges lead to the demand of a new class of nanoparticles that are organic in nature, that can provide beneficial interactions and aid in homogenous dispersion. Uncommon changes in dynamics and flow properties have been observed with these organic based nanoparticles due to their unique topology, and hence their complicated dynamics is still not well understood.[33] Several efforts have studied the changes in the dynamics of of polymer melts with the inclusion of soft and hard nanoparticles. For instance, Mackay et al., have shown unexpected viscosity reduction of a linear polystyrene (PS) entangled matrix with incorporation of soft nanoparticles. This reduction in viscosity was attributed to a reduction in free volume demonstrated in the change of glass

transition temperature. Increasing the concentration of the nanoparticle further leads to strong increase in viscosity at all frequencies as well as an increase in the plateau modulus which is attributed to abrupt changes in the entanglement mesh.[28]

Moreover, previous work in our group has shown an increase in diffusion of linear PS with incorporation of 10 nm soft cross-linked PS nanoparticles in contrast to hard nanoparticles that usually lead to a reduction in diffusion and suppression in the motion of polymer chains. Surprisingly, no increase in free volume was confirmed, indicating that simple plasticization cannot be the underlying mechanism. We attributed this unique behavior to a constraint release that speeds up the molecular motion similarly to star polymers.[87] This behavior is drastically different than what has been reported with hard nanoparticles. For instance, Winey et al reported that the addition of carbon nanotube (CNT) at different concentrations decreases the tracer diffusion of linear PS matrix until a minimum is reached at 0.4%, after which the diffusion of the matrix recovered.[63] Analogous results were also found in systems that incorporate grafted nanoparticles, where Composto et al. reported an even stronger slowdown in diffusion of the PS matrix with the incorporation of PS grafted silica nanoparticles.[99] They attributed this effect to the fact that with high grafting density on the nanoparticles, the free polymer chains can't penetrate through the grafted chains, in this case the effective particle diameter is larger than the core size leading to stronger confinement and a slowdown in the matrix dynamics.[84]

It is clear that a better understanding of the impact of soft nanoparticles on the dynamics of the polymer, as well as the effect of softness, size and deformability of nanoparticles on their motion, is needed to enhance their potential use. Although significant research has been implemented to study the dynamics of the polymer in vicinity of hard nanoparticles, the literature on nanocomposites containing entirely organic nanoparticles is still scarce.[85,31,100] This is due to the fact that it is hard to quantify the motion of these soft nanoparticles which are relatively slow compared to the linear polymer. Also, tuning contrast between the nanoparticle and the matrix can be difficult. Consequently, we have developed a protocol to measure the diffusion coefficient of soft nanoparticles in order to quantify their mobility. Our results show that these soft nanoparticles are mobile, not stationary and that the overall mutual diffusion of these systems can be described using the slow mode theory.[86] For this previous study, a set of soft cross linked PS nanoparticles was synthesized through nano-emulsion polymerization using a batch method where the rate of monomer addition was not controlled.[8] We then expanded our control over the soft nanoparticle structure, which enables this study that examines a new set of soft nanoparticles that vary in molecular weight, but retain the same crosslink density, and thus softness, of the original nanoparticles. The study of the diffusive behavior of these nanoparticles provides a pathway to separate the effects of the molecular weight and nanoparticle softness on its diffusive behavior to more precisely define the impact of nanoparticle softness on its translational motion.

Experimental

The examined samples were all bilayers of deuterated polystyrene on top and protonated nanoparticle on bottom. A control sample that is a bilayer of deuterated and protonated polystyrene was also prepared and examined under the same conditions to obtain the tracer diffusion coefficient of the linear polymer. The protonated and deuterated polystyrene were purchased from Polymer Source. Both have number average molecular weight of 535000 and polydispersity of 1.09. The soft polystyrene nanoparticles were synthesized by nano-emulsion polymerization of styrene where divinyl benzene, DVB, was added to the emulsion as a crosslinking agent. The synthesis process is shown in Figure 3.1. The DVB locks the polymer chain into a nanoparticle-like conformation. The first set of nanoparticles were synthesized by implementing a batch polymerization technique with no control over the rate of monomer addition and only crosslinking density was modified.[8] For each nanoparticle, variation in DVB added to the emulsion provided nanoparticles with crosslink densities of 0.80 mol % for NP1A, 1.91 mol % for NP2A and 4.60 mol % for NP3A. In these nanoparticles, as the crosslinking increases, the hardness of the nanoparticle increases. The morphology of the particles is best portrayed as a micro-gel with cross-links from the DVB producing a distinct core and a fuzzy interfacial shell consisting of free chain ends and loops. The increase in the amount of DVB generally decrease the radius of gyration of the nanoparticles and decrease its fuzziness. For the second set of nanoparticles,

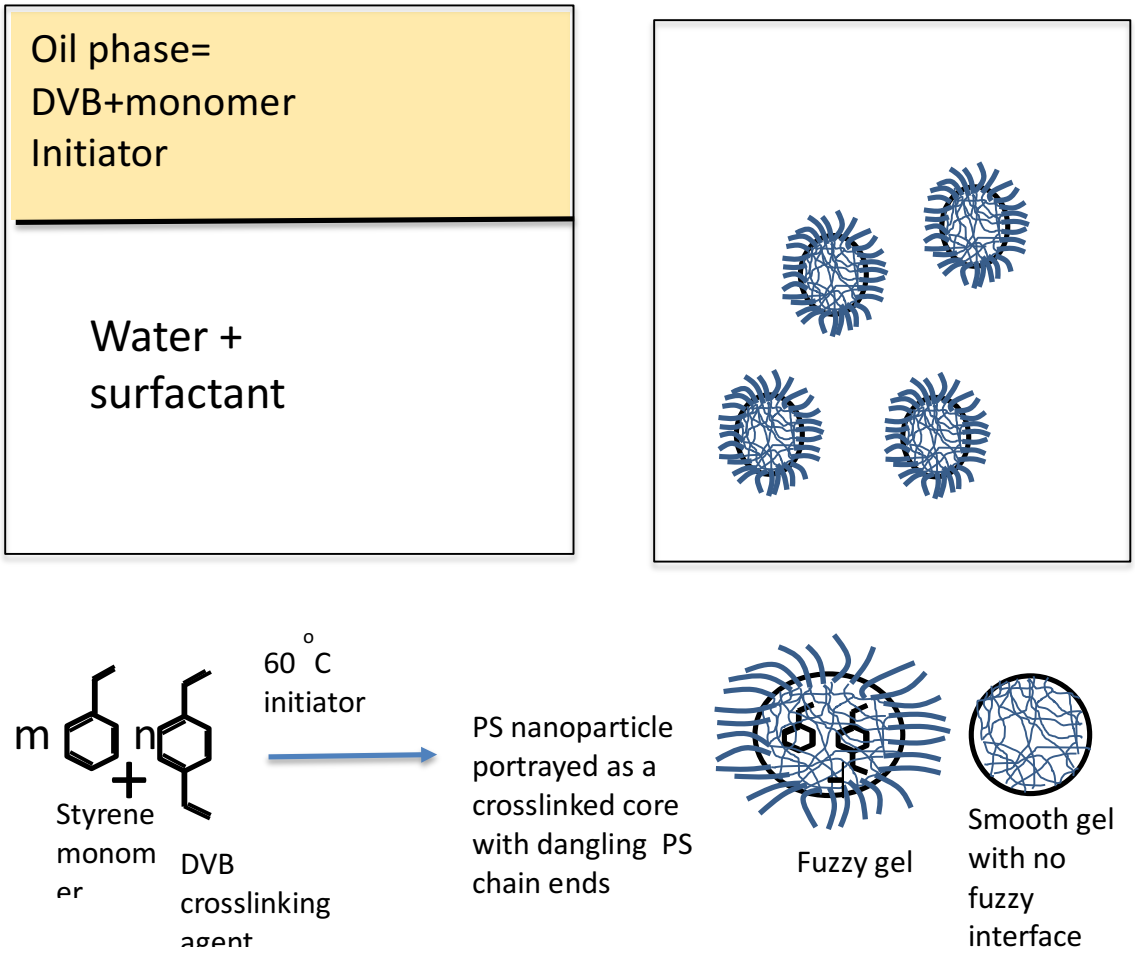

Figure 3.1: Depiction of the Nanoemulsion synthesis method for soft nanoparticles used in the study.

a semi batch technique was utilized where the rate of monomer addition is adjusted with the same DVB %.[33]

This method resulted in nanoparticles with similar morphology but with varying molecular weight. It is worth mentioning that using a semi-batch method and a very low rate of styrene addition at 4.60% DVB resulted in a nanoparticle with a slightly different morphology, referred to as smooth gel with no fuzzy interface. This specific nanoparticle NP3AA exhibits a very small R_g and zero fuzziness. The details of the nanoparticle molecular weight and topology are presented in Table 3.1.[33,8]

All Si wafers were purchased from Wafer World. Prior to bilayer casting, the Si wafers were cleaned in piranha solution of sulfuric acid and hydrogen peroxide in the ratio of (3 :1). The wafers were then rinsed in deionized water and dried. To further remove any organic contaminates, the wafers were placed in UV/ozone for 15 minutes. 1% to 1.5 % solutions of nanoparticle were prepared in toluene and used for spin casting. The solution was spin cast onto a wafer that is 2 inch in diameter and 6mm in thickness. All films were cast at 1500 rpm for 30 seconds to obtain the desired film thickness. For the deuterated layer, a 1% solution in toluene was spin cast onto a 4 inch wafer and then floated on water. The deuterated film was then picked up on the protonated layer forming a bilayer. All bilayers were then kept in a vacuum oven at room temperature for 24 hours to remove residual solvent. Neutron reflectivity experiments were then performed on the liquids reflectometer at Oak Ridge National Lab utilizing beamline 4. All samples were

Table 3.1: Nanoparticle synthesis method and morphology details from small angle neutron scattering (SANS) results.

Nano-particle	DVB [mol%]	Synthesis Method	Mw (g/mol) X10^6	Rg (nm)	Effective Fuzziness μ	Rg/Rh	
NP1A	0.81	Batch	0.78	12.9	0.30	0.65	
NP2A	1.91	Batch	0.81	11.3	0.22	0.60	
NP3A	4.60	Batch	1.21	9.85	0.15	0.66	
NP1B	0.81	Semibatch	0.238	10.1	0.36	0.56	
NP2B	1.91	Semibatch	0.175	6.83	0.22	0.68	
NP3B	4.60	Semibatch	0.419	7.0	0.16	0.79	
NP3AA	4.60	Semibatch	0.25	7.32	0	0.57	

measured as cast and after annealing for different times. The annealing process was completed in a vacuum oven at 150 °C. After each annealing time, the samples were quickly quenched on a cooling block to stop the diffusion process. The reflectivity of the sample was then measured and plotted as function of q_Z, which denotes the scattering vector perpendicular to the surface of the samples and is defined by the following equation:[20,18]

$$q_Z=(4\pi/\lambda)\sin\theta \qquad \text{Equation 3.1}$$

In this equation, θ is the angle of incidence and λ is the wavelength of the incident neutrons. All data were reduced and fitted using the analysis package MOTO FIT in IGORPRO. The reflectivity curves provide information about the surface and depth profile of the bilayer film. The scattering length density (SLD), thickness of the layers and roughness are all fine-tuned to provide the best fit for the reflectivity curves. The quality of the fitting is assessed statistically through the value of χ^2 that was less than 10 for all fits.[20,19] A mass balance check is performed by integrating the area under the SLD profiles for the as-cast and the annealed samples assuring that the variation does not exceed 5%.

Results and Discussion

Our first experiments monitored the mutual diffusion of a bilayer of linear PS and dPS 535K. This sample served as a control where the tracer diffusion coefficient of the linear matrix is determined and used in the analysis of the diffusion in the soft nanoparticle/linear chain bilayers. Figure 3.2 shows the reflectivity curve with clear fringes for the as cast sample, that decrease with

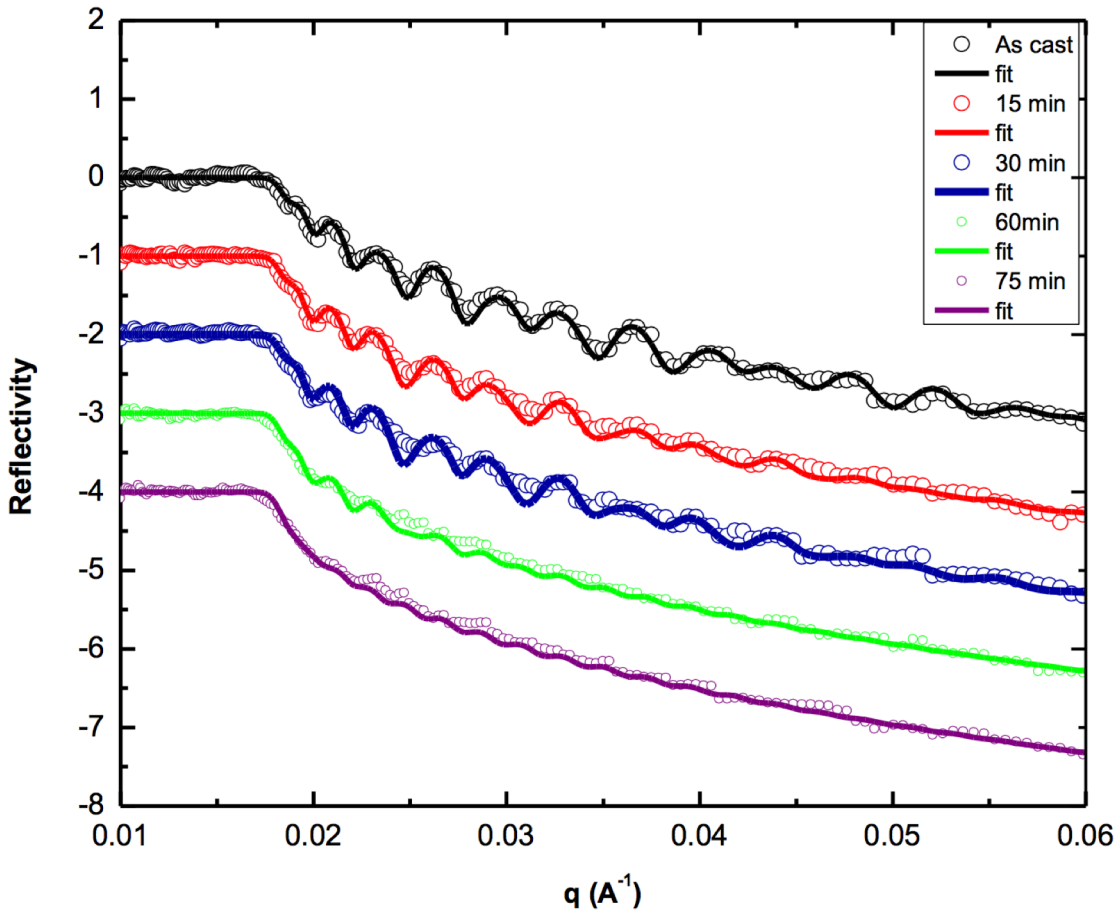

Figure 3.2: Representative reflectivity curves for hPS-dPS bilayers, the y offset is used for clarity.

annealing. The increase in roughness and dampening of fringes is an indication of the interdiffusion of the two layers. The scattering length density profiles in Figure 3.3 shows a sharp interface that broadens with annealing where both the deuterated and protonated polymers are moving at the same rate.

Similar experiments were then completed to monitor the inter-diffusion of bilayers of dPS 535K and the soft nanoparticle. The mutual diffusion of these samples represents the inter-diffusion of the nanoparticle into the linear polymer and vice versa. All nanoparticles diffuse into the linear matrix except for the Np3AA. Figures 3.4 and 3.5 show the reflectivity curves for NP1B and Np3AA, where dampening of the fringes with annealing was not observed for NP3AA suggesting that this nanoparticle is stationary, where the lack of fuzziness seems to suppress its motion. Moreover, to determine the mutual diffusion coefficient of the two components, the time evolution of the bilayer is monitored at different annealing times and fitted using the one-dimension solution of Fick's second law shown in Equation 1.2.[101]

$$\phi_d(z) = \frac{1}{2} c_0 \left[\mathrm{erf}\left(\frac{h - z}{\sqrt{4 D_m t}} \right) + \mathrm{erf}\left(\frac{h + z}{\sqrt{4 D_m t}} \right) \right] \qquad \text{Equation 3.2}$$

In this equation, t and h are the annealing time in seconds and the initial dPS thickness, respectively. Fitting the density profile of the deuterated material, $\phi_d(z)$ to Equation 3.2 provides the mutual diffusion coefficient of the linear polymer and nanoparticle.

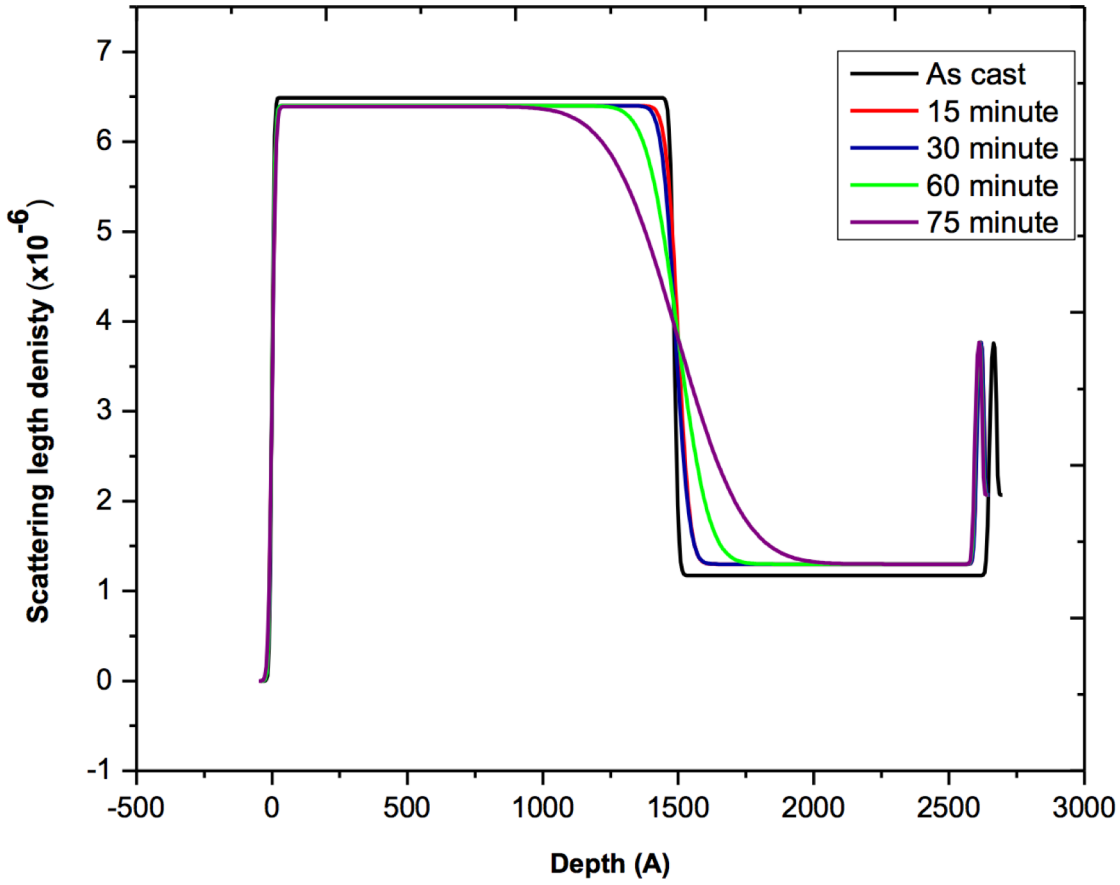

Figure 3.3: Scattering length density (SLD) profile for hPS-dPS bilayer.

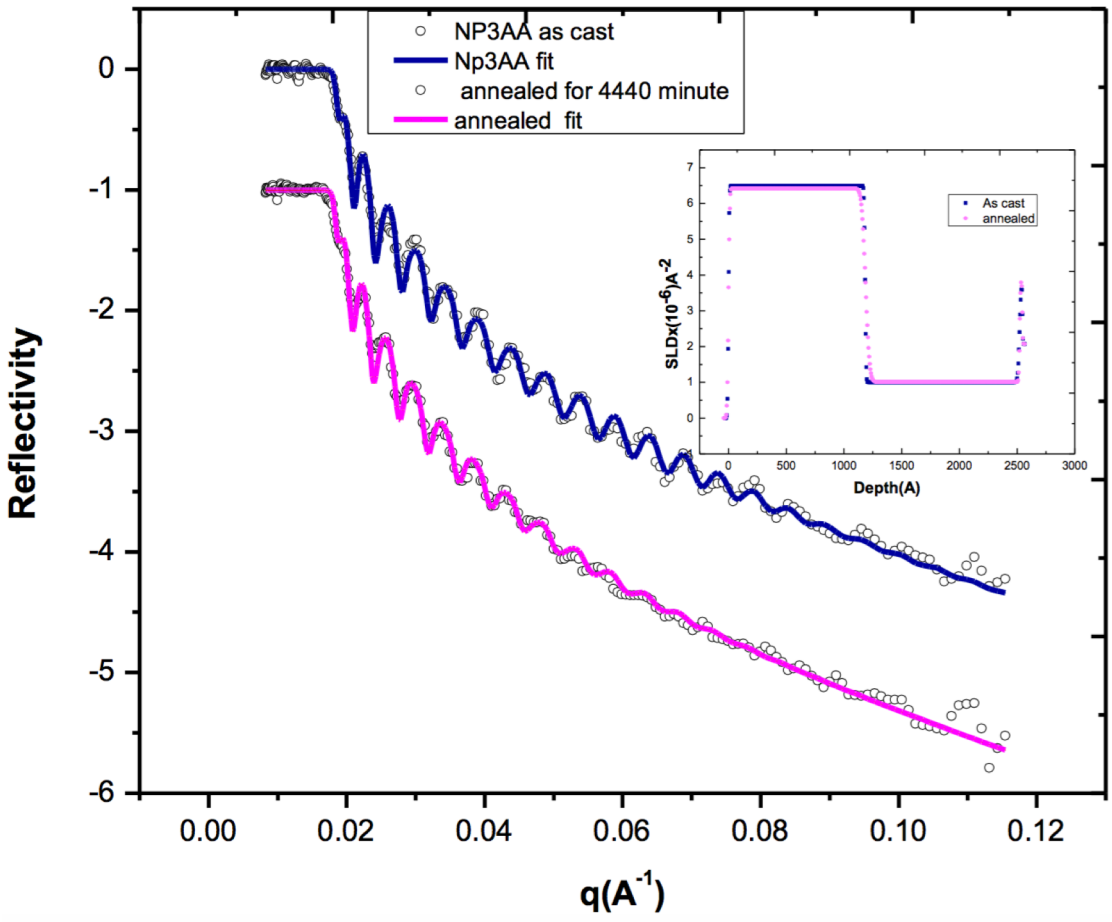

Figure 3.4: Representative reflectivity curves for NP3AA-dPS bilayers as cast and after the longest annealing time.

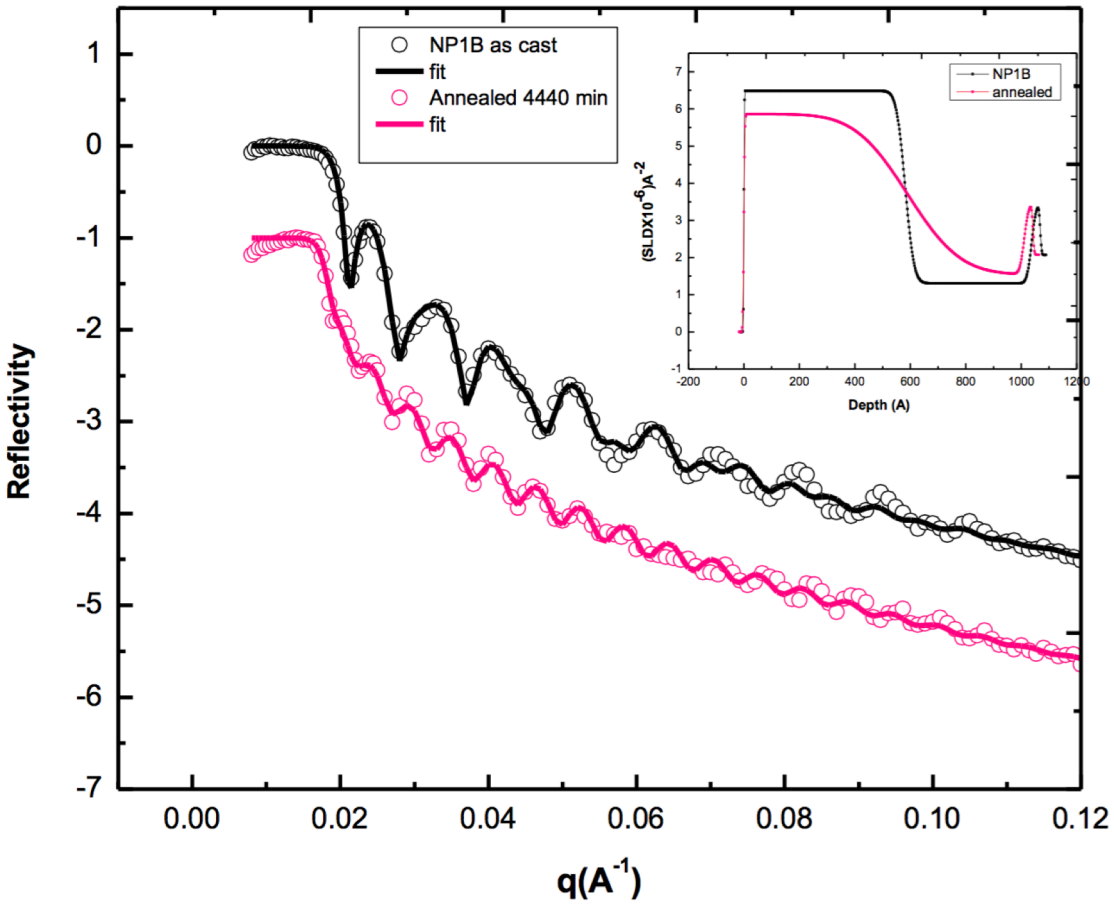

Figure 3.5: Representative reflectivity curves for NP1B-dPS bilayers as cast and after the longest annealing time.

The scattering length density profiles SLD_m (z) extracted from fitting the reflectivity data were used to determine the density profiles of the deuterated material using Equation 3.3

$$\phi_d(z) = 1 - \frac{SLD_d - SLD_m(z)}{SLD_d - SLD_H} \qquad \text{Equation 3.3}$$

Figures 3.6 and 3.7 show the volume fraction profiles for the NP1A and NP3A bilayers as cast and after the longest annealing time of 63 hours. NP1A and NP3A exhibit sharp transitions between layers for the as-cast samples that tend to roughen with annealing due to interdiffusion of both dPS and protonated nanoparticle layers. However, NP1A exhibits a broader interface with annealing in comparison with NP3A. It is qualitatively clear from the volume fractions that the diffusion process is asymmetric where the polymer and the nanoparticle are moving with different rates.

The mutual diffusion coefficient (D_M) can then be correlated to the Onsager transport coefficient (D_T) using the following equation [102,103]

$$D_M = 2(\chi_s - \chi)\phi_1\phi_2 D_T \qquad \text{Equation 3.4}$$

where χ is the Flory-Huggin interaction parameter between polymer and nanoparticle and ϕ is the volume fraction. The segment-segment interaction parameter χ is estimated to be zero since the matrix and the nanoparticle are chemically analogous. Furthermore, χ_s that denotes the interaction parameter at the spinodal can be calculated using Equation 3.5.[102]

$$\chi_s = \frac{1}{2}\left(\frac{1}{\phi_1 N_1} + \frac{1}{\phi_2 N_2}\right) \qquad \text{Equation 3.5}$$

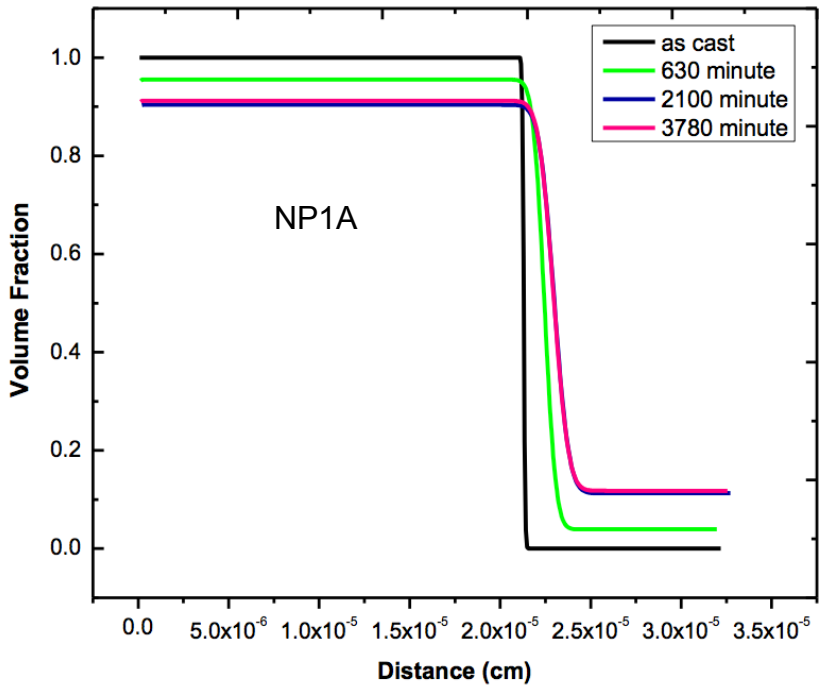

Figure 3.6: Volume fraction profiles NP1A and NP3A.

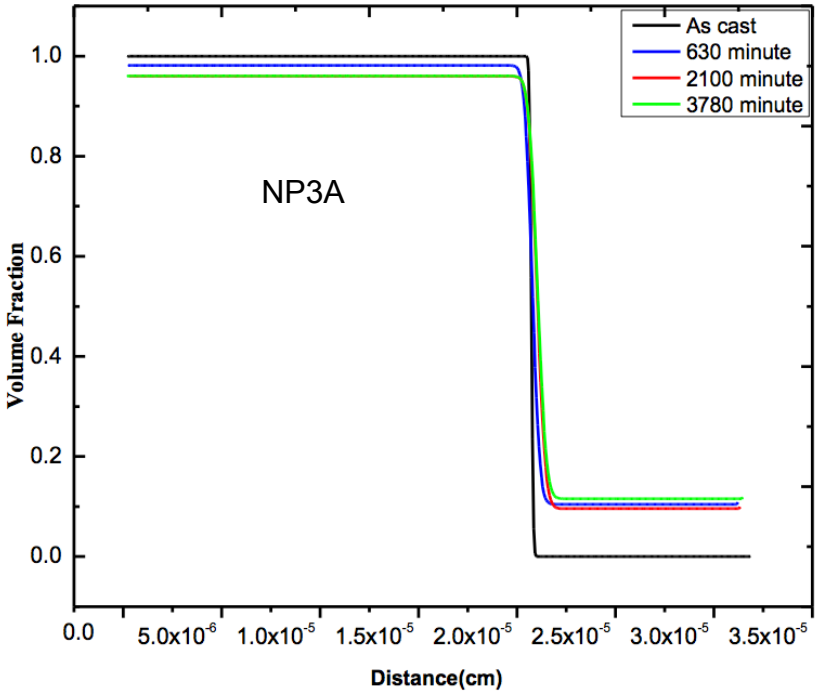

Figure 3.7: Volume fraction profiles NP3A.

The mutual diffusion coefficient extracted from this analysis represents the change of concentration gradient of both species however, in order to identify the tracer diffusion coefficient which represents the discrete motion of the nanoparticles, two models were considered.[104,105] The fast mode theory developed by Kramer is a model for a system where the overall diffusion is controlled by the fast component and is represented by the following equation [104]

$$D_T = \phi_{NP} D_{PS} N_{PS} + \phi_{PS} D_{NP} N_{NP.} \qquad \text{Equation 3.6}$$

where NP and PS are the nanoparticle and the linear polystyrene matrix while D represents the tracer diffusion coefficients of the different components. N is the degree of polymerization and φ represents the volume fraction at the inflection point which is set to 0.5. Analysis of the mutual diffusion coefficient using the fast mode theory leads to negative and unreasonable values for the tracer diffusion coefficient, so it is not considered further and the slow mode theory is used for correct evaluation of the relationship between the mutual diffusion coefficient and tracer diffusion coefficients of the polymer and nanoparticle.

The slow mode theory presented by de Gennes relates the Onsager transport coefficient to the tracer diffusion coefficients of polystyrene and the nanoparticle using the following equation[104 ,106]

$$\frac{1}{D_T} = \frac{\phi_{NP}}{D_{PS} N_{PS}} + \frac{\phi_{PS}}{D_{NP} N_{NP}} \qquad \text{Equation 3.7}$$

With knowledge of the tracer diffusion coefficient of the linear matrix and χ_s, all variables in the equation are known and the tracer diffusion of the nanoparticle can

be determined. Table 3.2 shows the tracer diffusion coefficients of the first set of nanoparticles as determined using both theories.

It is well established that the slow mode theory is more consistent with high molecular weight polymers while the fast mode theory is more reliable for low molecular weight systems.[106] Interestingly, our high molecular weight system confirms this view where the slow mode theory provides more realistic diffusion coefficients demonstrating that the measured mutual diffusion in our system is controlled by the slow nanoparticle. Figure 3.8 shows the tracer diffusion coefficients as a function of annealing times for both sets of nanoparticles where the tracer diffusion levels off and equilibrates at long annealing times. At short annealing times the tracer diffusion changes rapidly and denotes the transition of the motion of the particles from sub-diffusive to diffusive motion. Thus, to evaluate the tracer diffusion correctly, it is crucial to anneal the samples for long times and confirm that the particles pass the sub diffusive regime. Table 3.3 lists the tracer diffusion coefficients that are experimentally determined for all nanoparticles using the slow mode theory at the longest annealing time.

In Figure 3.9, the tracer diffusion coefficients of the soft nanoparticles are plotted as a function of molecular weight for each crosslinking density. Interestingly, there is a clear trend with cross linking density where increasing crosslinking density leads to a decrease in the tracer diffusion of the nanoparticle for a given molecular weight. This result verifies that decreasing the deformability of the nanoparticle reduces its mobility regardless of nanoparticle molecular

Table 3.2: Mutual diffusion coefficients determined from fitting the volume fractions to the solution of Ficks second law and the tracer diffusion coefficients as estimated using slow and fast mode theory.

	D_m (x 10^{-17}) cm^2s^{-1}	$D_{t,slow}$ (x 10^{-18}) cm^2s^{-1}	$D_{t,fast}$ (x 10^{-16}) cm^2s^{-1}
NP1A	1.35	5.56	-4.58
NP2A	1.81	7.31	-4.33
NP3A	4.05	12.9	-2.66

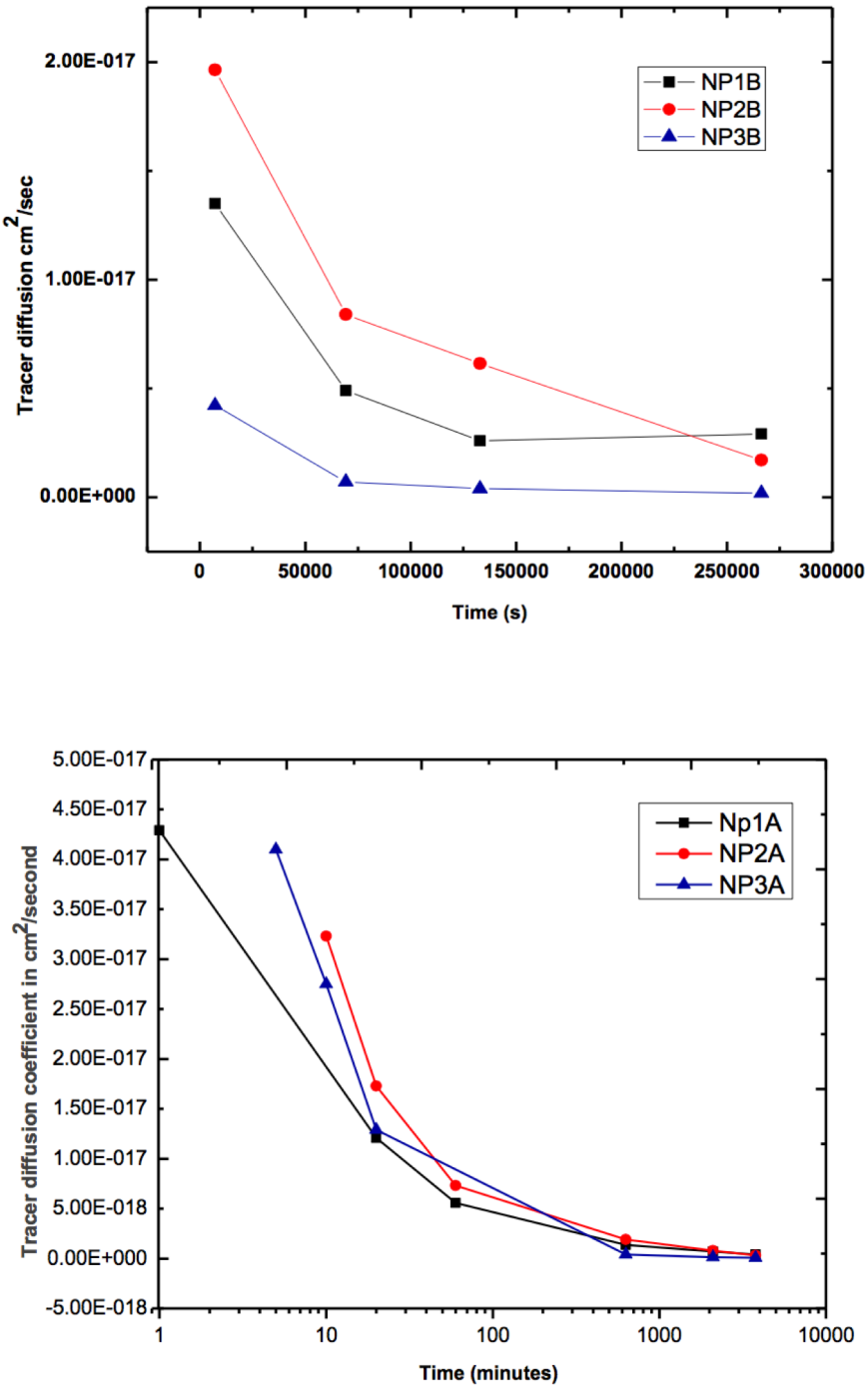

Figure 3.8: Tracer diffusion coefficient as function of annealing times for all nanoparticles parameter for different NP1B loadings.

Table 3.3: Tracer diffusion coefficient at the longest annealing time calculated using the slow mode theory for all nanoparticles.

	Molecular weight (g/mol) x 10^{-6}	**DVB%**	**Tracer diffusion $D_{t,slow}$ (x 10^{-20})**
NP1A	0.78	0.81	39.5
NP2A	0.81	1.91	30.8
NP3A	1.21	4.60	7.03
NP3AA	0.25	4.60	-
NP1B	0.238	0.81	291
NP2B	0.175	1.91	170
NP3B	0.419	4.60	19.3

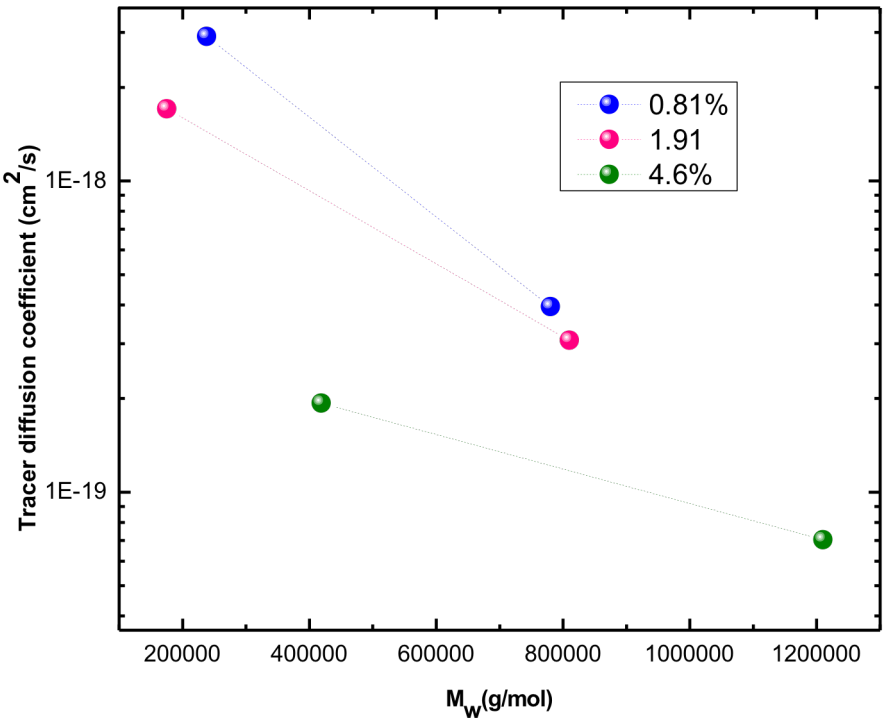

Figure 3.9: Tracer diffusion coefficients plotted as function of molecular weight for different crosslinking density.

weight. A more highly cross-linked core increases the nanoparticle hardness, which leads to the nanoparticles being less able to deform and fit into the available spaces within the matrix and hence, their motion in highly entangled system is suppressed. Increasing the cross-linking density from 0.81 to 1.91 decreases the tracer diffusion by a factor of ~2 while increasing the crosslinking density to 4.6% reduces the mobility further. Another interesting trend is the great reduction in nanoparticle mobility with increasing molecular weight for all crosslink densities.

The molecular weight dependence is further shown in Figure 3.10 where log-log plots of the nanoparticle tracer diffusion as a function of molecular weight are presented. Qualitative inspection of these plots provides further insight onto the mechanism of diffusion. The molecular weight dependence is stronger for low cross-linked nanoparticles which further validates the assumption that deformable nanoparticles diffuse faster due to its ability to distort and fit into spaces. Another factor that needs to be taken into consideration is the effective fuzziness that is reduced with increasing the cross-linking density. These dangling chain ends could also lead to disentanglement and dilation of the reptation tube of the linear matrix and further facilitate diffusion of the nanoparticle. NP3AA nanoparticle with no fuzzy interface does not move over similar timescales, suggesting that the smooth nanoparticle interface can lead to increased friction between nanoparticle and linear chain that significantly inhibits its motion.

In Figure 3.11, the ratio of the diffusion coefficients of linear analogues to that of the nanoparticle is plotted as function of crosslinking density for all

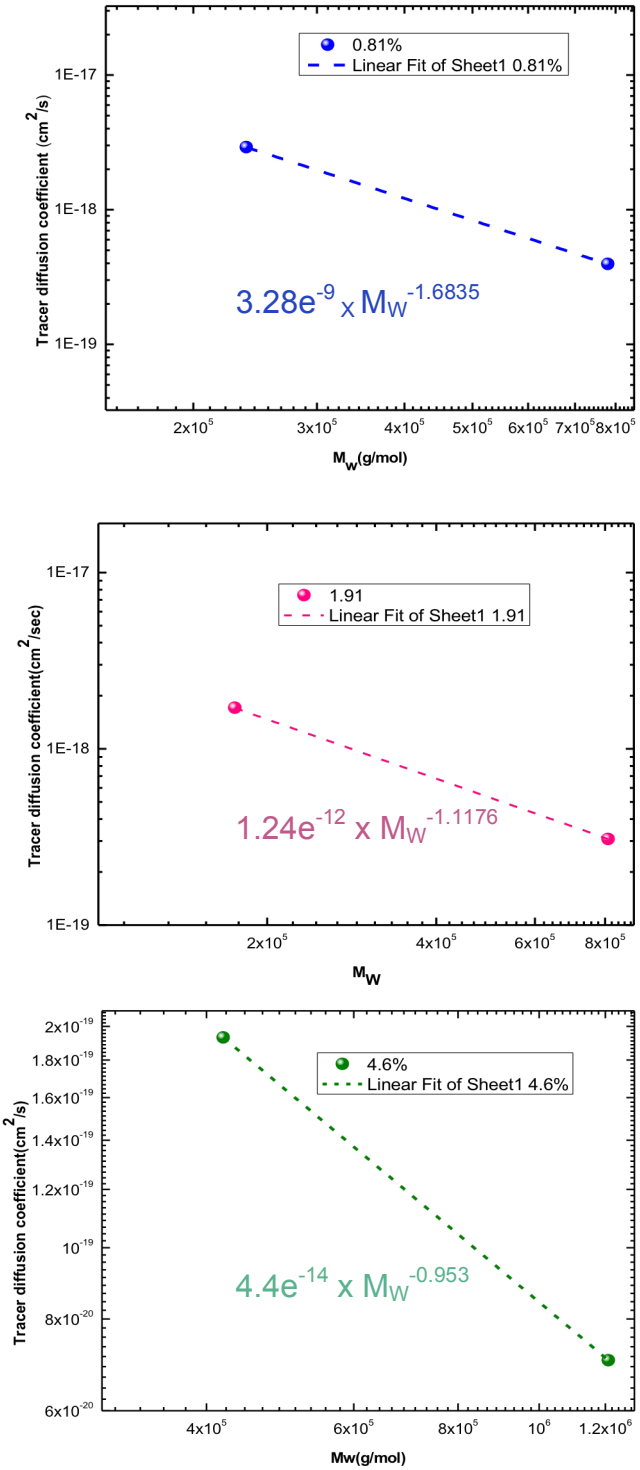

Figure 3.10: Log-log plots of tracer diffusion as function of molecular weight for different crosslinking densities for different crosslinking density.

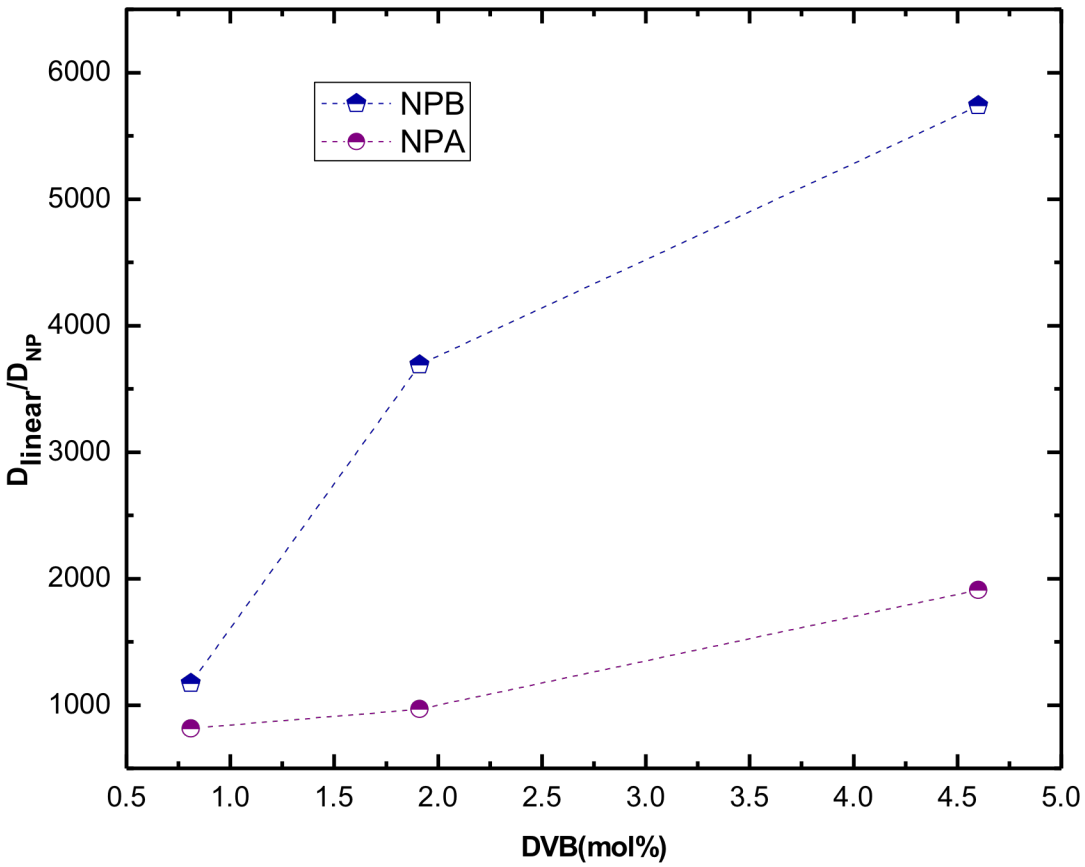

Figure 3.11: The ratio of the tracer diffusion of the linear polymer matrix to the nanoparticle analogue as function of crosslinking density.

nanoparticles. The increase in this ratio with cross linking density for all nanoparticles validates the importance of softness of the nanoparticle on its mobility regardless of molecular weight. Our previous results showed that incorporation of these nanoparticles onto 535K linear dPS leads to an increase in diffusion of the linear matrix, where this result is explained in terms of constraint release similar to what has been reported in the literature with star polymers.[87,86,92] Surprisingly, our nanoparticles don't exhibit an exponential molecular weight dependence of the diffusion coefficient that is expected for star polymers.[107,108] Thus, while these particles appear to exhibit some similarity in their behavior to star like polymers, their nanoscale structure is sufficiently different that these nanoparticles diffuse by a different mechanism than stars.

Figure 3.12 shows the tracer diffusion coefficient of the nanoparticle plotted along with D_T of their linear analogues. The nanoparticles diffuse much slower than a linear matrix. This result is consistent with our previous interpretation suggesting that the soft nanoparticle motion is more similar to fractal microgels rather than star polymers and thus, require a cooperative motion of the polymer chain to diffuse.[109,110] The deformability of these nanoparticles can additionally lead to different conformations adopted by the nanoparticles depending on the degree of entanglement of the matrix and hence lead to different mechanisms of diffusion, somewhat similar to pinned and unpinned cyclic polymers that may follow linear reptation in some cases and in other scenarios diffuse via arm retraction seen in stars.[92] It will be interesting to monitor the diffusion of the nanoparticle in different

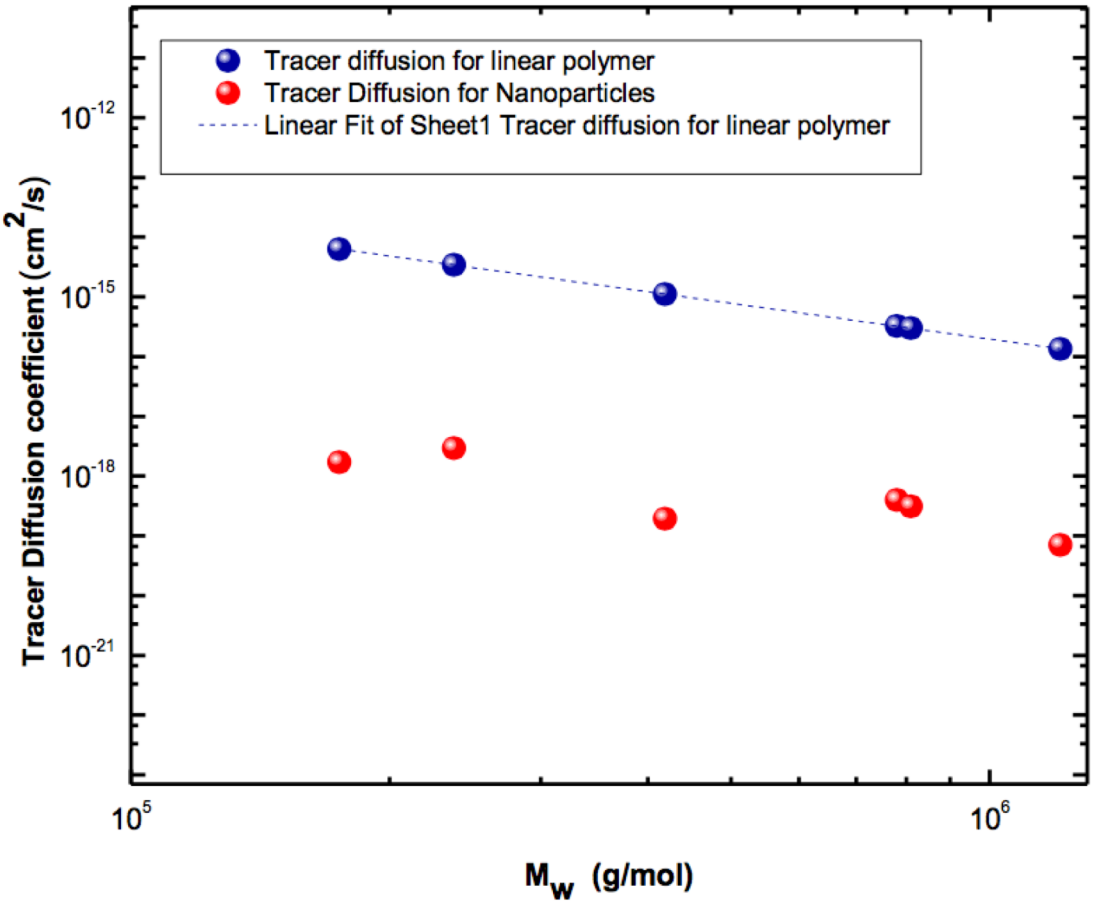

Figure 3.12: Log-log plot of tracer diffusion versus molecular weight for nanoparticle and their linear analogue.

molecular weight matrices to capture their mechanism of diffusion, where they may deform differently depending on the level of entanglement.

Figure 3.13 compares the diffusion coefficient of the nanoparticles to the theoretical Einstein diffusion for a hard sphere of similar radii. The diffusion coefficients of the spherical nanoparticles are related to its mean square displacement using the following equation

$$\mathrm{MSD} = \frac{1}{N-n}\sum_{i=0}^{N-n}((\chi_{i+n}-\chi_i)^2+(y_{i+n}-y_i)^2) \qquad \text{Equation 3.8}$$

where (χ_i, y_i) are the coordinates of a particle at the ith step. The diffusion coefficient is then defined in two-dimension space as

$$MSD(t) = 4D_T t \qquad \text{Equation 3.9}$$

The classical Stokes-Einstein behavior is then represented by Equation 3.10 where K_b is Boltzman constant, T is the temperature, η is the fluid viscosity of the matrix and d is the diameter of the particle. The viscosity of neat PS was measured using rheology to be approximately 5.75×10^5 Pa

$$D_T = \frac{k_b T}{3\pi\eta d} \qquad \text{Equation 3.10}$$

Equation 3.10 is then used to estimate the diffusion coefficient of hard spheres that are the same size as these nanoparticles. These results are shown in Figure 3.13, where the Stokes-Einstein value is shown in black, while the experimental values for the soft nanoparticle diffusion coefficient are represented by the blue symbols. The results are also listed in Table 3.4. It is interesting that these soft nanoparticles all exhibit diffusivities that are slower than

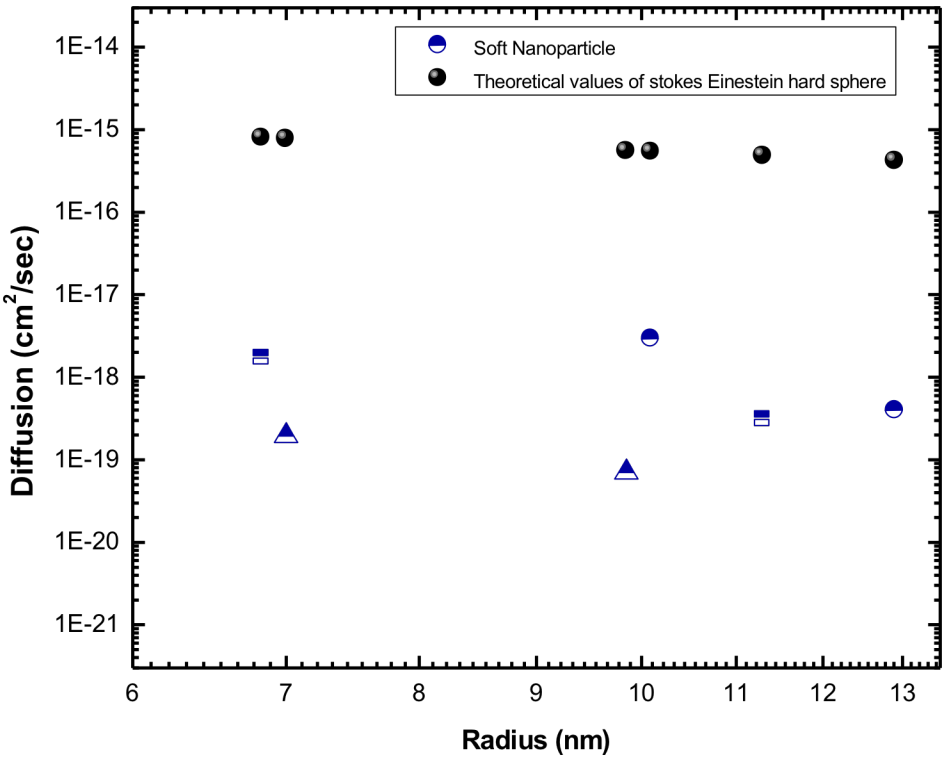

Figure 3.13: Predicted Stokes-Einstein diffusion coefficients for hard spheres as a function of radius and tracer diffusion coefficient of the soft nanoparticles. (blue circles for soft nanoparticle with 0.81% crosslinking density, blue squares for crosslinking density of 1.91% and blue triangles for 4.60 %).

Table 3.4: Experimental tracer diffusion for soft nanoparticle and theoretical Einstein diffusion for hard sphere of same radius.

	Radius of nanoparticle (nm)	Crosslinking density %	Stocks Einstein Theoretical Diffusion ($x10^{-16}$)	Soft nanoparticle Experimental Diffusion ($x10^{-20}$)
NP1A	12.9	0.81	4.18	39.5
NP2A	11.3	1.91	4.77	30.8
NP3A	9.85	4.60	5.48	7.03
NP1B	10.1	0.81	5.34	291
NP2B	6.83	1.91	7.90	170
NP3B	7.0	4.60	7.70	19.3

that predicted by the Stoke-Einstein equation, indicating that simply accounting for friction fails to capture the motion of these nanoparticles and highlight the importance of the fuzzy interface that allow further interactions between the nanoparticle and the matrix. The short polymer chains on the nanoparticle surface may entangle with the matrix leading to further suppression in the nanoparticle motion in comparison to bare spheres.

Conclusion

We present a novel methodology to determine the diffusion coefficient of organic based nanoparticles in order to elucidate the dynamics and physics controlling their behavior in a linear polymer matrix. Monitoring the diffusion coefficient of nanoparticles with identical crosslink density, and thus softness, for multiple molecular weights provides a pathway to tease out the importance of nanoparticle softness on its diffusive properties.

These results show that the motion of the nanoparticle is linked to its softness and therefore deformability. For a given molecular weight, increasing the crosslinking density of the nanoparticle increases its hardness and suppresses its diffusive motion in linear matrix, emphasizing the importance of the deformability of the nanoparticle as well as their effective fuzziness on the nanoparticle motion. Moreover, the nanoparticle molecular weight dependence varies with nanoparticle softness and deviates from the exponential molecular dependence for star polymer diffusion. Thus, it appears that the diffusion of these nanoparticles resembles fractal microgels that can take advantage of the cooperative motion of the matrix

to open pathways for the nanoparticle to diffuse. Comparison of the experimental values to those predicted from Stokes Einstein theory shows great deviation where the nanoparticles diffuse slower than a hard sphere. This indicates a possibility of some existing entanglements between the nanoparticle surface and the matrix that possibly suppress the nanoparticle motion. Consequently, simple friction in Stokes-Einstein formula can't represent the motion of the nanoparticle precisely. Further studies of the diffusion of these nanoparticles in lower molecular weight matrices are underway to provide further insight onto the role of the matrix entanglements on diffusion and conformations adopted by the nanoparticle inside the matrix.

CHAPTER 4

ENHANCING INTER FILAMENT BONDING OF PLA VIA GRAPHENE REINFORCEMENT IN FUSED DEPOSITION MODELING

Introduction

Additive manufacturing (or 3D printing) has gained substantial interest recently as a versatile form of manufacturing that may transform industries and increase the speed of production. Fused deposition modeling (FDM) is a common form of 3D printing where polymer filament is extruded at high temperature and laid down to cool and solidify, forming structures in a layer by layer fashion. Compared to other methods of additive manufacturing, such as selective laser sintering (SLS) and stereolithography (SLA), FDM is one of the more cost effective methods and hence widely used.[36] Several fields can benefit from improved FDM technology including biomedical, construction and automotive industries.[36,111,44,35,112] Hence, a significant amount of research is employed in this area to enhance the robustness of prototypes produced so that the technology may translate from bench top production to large scale manufacturing.

In FDM, a prototype is built layer by layer in an additive fashion from base to top, where a polymer filament is extruded at high temperature and laid down to cool and solidify. This process usually results in large voids and pores between the solidified layers. As a result, FDM prototypes exhibit anisotropy, where mechanical properties in the direction parallel to the bed (XY) and along the deposition direction are significantly better than those in the perpendicular direction (Z). This anisotropic behavior is a challenging problem, especially for large scale manufacturing where mechanical strength is a priority.[36,41,42]

Several polymers are utilized in FDM, where poly lactic acid (PLA) and acrylonitrile butadiene styrene (ABS) are among the most commonly used. Since PLA is a biodegradable and biocompatible polymer, it can be utilized in various applications and represents a special interest of medical fields. However, both polymers exhibit poor thermal conductivity and high thermal expansion which may lead to warping and delamination of layers due to weak bonding, exacerbating poor mechanical properties in the z direction.[44] Several factors can contribute to this issue, for instance, the fast cooling rates of the extruded layers to temperatures below glass transition temperature (T_g), the slow rate of polymer chain diffusion during the cooling process, and finally minimal polymer entanglements between layers that promote physical bonding at the interface and lead to better interfacial adhesion. [113,114]

Several studies have addressed this issue, where some work focused on varying printing parameters such as raster angle, infill density and printing speed to decrease structural anisotropy.[41] While some improvement in overall mechanical properties were achieved in these studies, the anisotropy problem persists. Other work focused on enhancing interlayer adhesion chemically through the introduction of thermally reversible crosslinking at the interface. For instance, Smaldone et al. designed partially crosslinked terpolymers that incorporate reversible furan-maleimide Diels-Alder (fm-DA) functionalities. These systems produce thermally reversible cross-links. During printing at elevated temperatures, the system undergoes depolymerization through retro-DA reactions and then

repolymerization after cooling through fm-DA adduct formation, creating new covalent bonds. The authors reported improvement in inter filament strength, however the mechanical strength was still quite affected by printing orientation. [115]

Previous research in our group has also tackled this problem through introducing bimodal molecular weight blends composed of a bulk polymer poly lactic acid (PLA) and additives which are identical but smaller polymer chains synthesized in our lab.[42,114,116] Improvement in interlayer adhesion and more isotropic samples were successfully achieved with the incorporation of the low molecular weight chains. Our group attributed these results to an improvement in entanglements across layers as those small chains diffuse more readily across the filament interface during the thermal history of the printing process. Interestingly, these improvements were observed for additives with specific molecular weights and also with specific loadings demonstrating the importance of a balance between the plasticization effects and the length requirement for these additives to entangle. This study clearly shows that diffusion and dynamics across interfaces during the printing process play a significant role on the creation of physical bonding and adhesion between layers.[114]

Other studies attempted to improve the poor mechanical properties of prototypes produced by FDM through the introduction of fillers[37] such as, carbon fibers[117,118,38], graphite[119] and cellulose nanocrystals to the bulk polymer.[120,121] Carbon fibers have been used extensively as a promising filler that can reduce thermal expansion and enhance dimension stability. Although carbon fibers can

lead to mechanical reinforcement and decrease warping, when a large car chassis was printed using ABS/ carbon fiber, delamination and cracking between layers developed in thin sections due to the fact that these sections were susceptible to fast cooling rates. For large scale manufacturing, the rapid cooling rates of the extruded layers and the developed thermal gradient can significantly impact dimensional stability, warping and mechanical strength.[44] Thus, several thermal models were developed to understand the evolution of the thermal profiles of FDM and the changes in thermal gradient in the printed part developed with different printing parameters including, extrusion temperature, bed temperature, ambient conditions and printing speed.[39,45,122] For instance, Compton et al. monitored the thermal evolution of the printing of large scale ABS/ carbon fiber composites using a thermal imaging camera and used the data to build a 1D heat transfer model of the build process. Several assumptions are required in the model that differ from the 3d printing environment and thus some discrepancy in experimental results with the model are observed.[44] Due to the 1D nature of the model, it under estimates the heat transfer by conduction and predicts that higher thermal conductivity can lead to faster cooling rates and heat loss. These predictions are not observed in recent experimental work[113] which necessitates more effort in determining the thermal evolution during a 3D printing process experimentally and correlating this to the material thermal properties.

In a different study, Dinwiddiee et al., monitored the temperature profile of printed samples that consist of neat ABS or ABS-carbon fiber composites on bench

top and manufacturing size printers (Solidoodle and Big Area Additive Manufacturing (BAAM) printers) using IR thermal cameras. The results of this work revealed that the addition of carbon fiber to ABS increased the required extrusion temperatures and slowed down the cooling rate of newly deposited layers. However, the impact of these thermal improvements on strength in the z-direction was not presented. [113]

Ultimately, the inherent thermal conductivity of a printed material will impact the thermal profile found during printing, as well as the development of residual stresses inside printed samples. However, there remains large gaps in our understanding of how thermally conductive fillers impact the thermal profile and thermal history of the material during printing. Moreover, the correlation of the high thermal conductivity of carbon based fillers to their enhancement of mechanical properties and potential improvement of inter-layer adhesion is still unclear.

The aim of this work is to evaluate the role of incorporating graphene as a filler for PLA in fused deposition modeling on the anisotropic mechanical properties, thermal conductivity and history, and inter-filament adhesion of the printed structure. In this study, PLA composites with different graphene loadings were fabricated, extruded to filaments and used in 3D printing. An IR thermal camera is then used to monitor the thermal evolution of the prototypes during printing, as well as record the thermal gradient in the printed sample with increasing bed temperature. These thermal properties are then correlated to the tensile properties and extent of interfilament diffusion in the printed samples to

provide a fundamental understanding of the role of the graphene on the alteration of the structure and properties of the printed samples.

Experimental

Materials

Natureworks PLA 4043D pellets (Filabot), Graphene Composite grade (Celtig), and Dimethyl Formamide (DMF) (Fisher Scientific), were all used as received.

Composite Fabrication

To fabricate composites with well dispersed graphene, a well documented coagulation method was used. In this procedure, the graphene was added to DMF to give a concentration of 0.25mg/ml, which was sonicated in a sonication bath for 24 hours to disperse the graphene sheets. PLA pellets were first dried and then added to the graphene solution to achieve graphene loadings of 0.5, 1 and 2%. The solution was then gently heated and magnetically stirred to allow PLA to dissolve. The suspension was then dripped into a large amount of deionized water (V_{DMF}/V_{water}=1:5) in a blender. Due to poor solubility of PLA in water, PLA precipitated immediately trapping the graphene sheets. This quick precipitation method inhibits the re-stacking of the graphene sheets.[53] The composite was then filtered and left to dry in a vacuum oven at 120 °C for 24 hours. The dried composite was then pelletized and extruded at 168 °C using Filabot single screw extruder. The filament diameter was maintained at 2.85 ± 0.1mm. The samples during the composite fabrication process are shown in Figure 4.1.

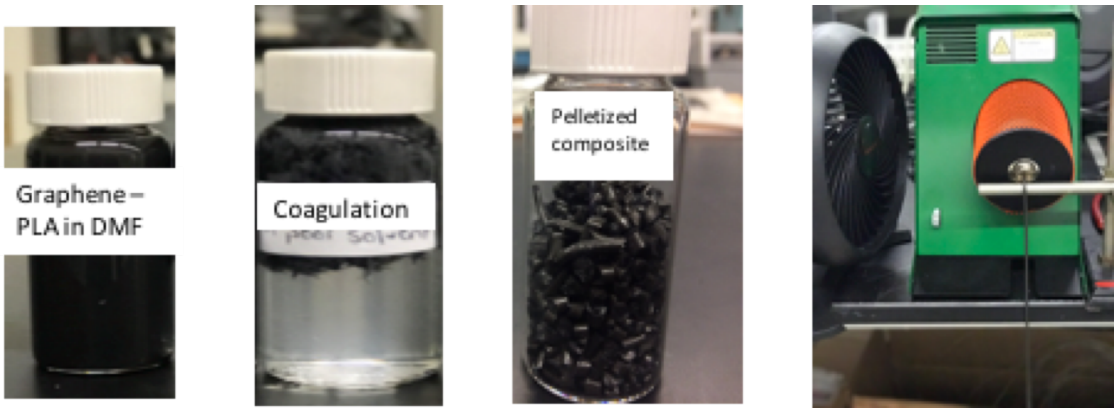

Figure 4.1: Pictures showing the different stages of graphene composite fabrication and filament extrusion.

3D Printing and Thermal Characterization

The printing process starts by creating a 3D CAD model of a cube that has dimensions of 70 × 70 × 70 mm. The cube was then sliced using slic3r program to generate a G-Code. All cubes are 233 layers with a layer height of 0.3mm. The printing speed was set at 45 mm/second and with a concentric infill. A LulzBot TAZ5 3D printer with 0.5mm nozzle is used to print the samples. All cubes, whether made of PLA or the graphene composite, were printed at the same extrusion temperature of 190 °C. The impact of changing the build plate to 70, 85, or 100 °C on the thermal profile of the printed sample and resultant mechanical and structural properties was also studied. A FLIR A35 long wave IR camera positioned approximately 40 cm from the central portion of the cube recorded the thermal profiles of the structure during printing. The camera is equipped with a 28mm lens and capture video at a frame rate of 1/s. The temperature profiles at different times in the printing process can then be readily extracted from these videos using Research IR software. The 3D model and IR camera setup is shown in Figure 4.2.

Mechanical Testing and Void Space Analysis Using SEM

Dog bones according to ASTM D638-V standard were cut from the printed cubes using a laser cutter. The tensile specimens were cut in two orthogonal orientations as shown in Figure 4.3 where the filament orientation is either parallel or perpendicular to applied stress. Six specimens were tested for each printing condition to obtain good statistics. The tensile properties of these dog bones were determined on an Instron universal testing machine using a 100 kN load cell and

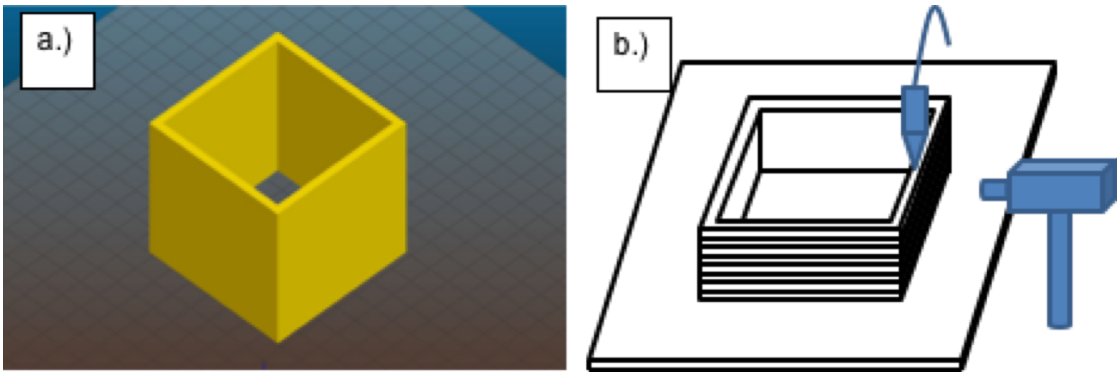

Figure 4.2: a) Picture of the 3D model of the printed cube and b) diagram showing the geometry of the IR Camera placement.

.

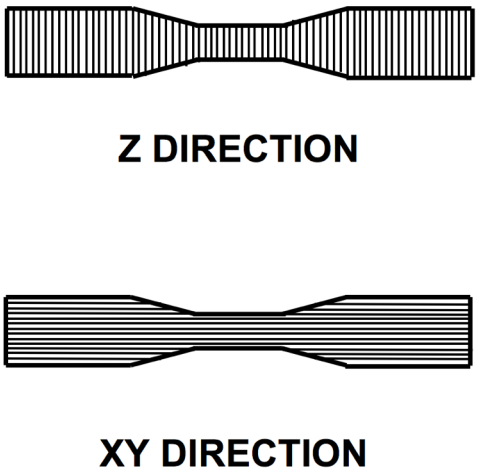

Figure 4.3: Filament orientation in Z-direction and XY-direction tensile specimens.

.

wedge grips with an extension rate of 1.00 mm/min. Void spacing between filaments at the fractured surface of tensile specimens were imaged using a Zeiss EVO MA15 with variable pressure and Bruker eFlash Electron Back Scattered Detector. All samples were gold sputtered prior to imaging.

% Crystallinity Evaluation Using Differential Scanning Calorimetry (DSC)

Differential scanning calorimetry was used to determine the amount of crystallinity in the printed samples using a TA instruments DSC Q2000. 10 mg of sample was heated in a cyclic program in which the sample was heated from 10 °C to 180 °C with a ramp rate 10 °C/ min and then cooled at a rate of 20 °C/min. The percent crystallinity is found by dividing the heat of melting on heating by the standard heat of melting of PLA (75 J/g).[42]

Thermal Conductivity

The thermal conductivity of each sample was determined using the double-sided transient plane source method (TPS) with a hot disk TPS 2500S. The measured specimens were disks with dimensions 20mm in diameter and 4 mm in thickness. All disks were cut from 3d printed walls with concentric infill to insure minimal changes in porosity. The samples were heated using a 0.8 W power input for 1 second. The TPS technique is based on a transiently heated plane sensor. The sensor is composed of electrically conductive nickel that is in the shape of a double spiral and sandwiched between two insulating sheets of Kapton, where the temperature increase of the sensor can be deduced accurately from its resistance. During the measurement, the sensor is placed between two identical discs of the

specimen as shown in Figure 4.4. An electric pulse is then passed through the sensor to increase its temperature several degrees. The sensor then acts as a heat source and a dynamic temperature sensor. The time that the current pulse should be applied has to be short enough that the sensor is considered in contact with a finite solid during data recording. The resistance of the sensor will increase as the current is applied leading to drop in voltage.[123,124] The voltage and current are then recorded over time, where information regarding heat flow between sensor and material is acquired. The technique allows determination of thermal conductivity K and heat capacity C_p of the sample.

Results

Tensile Properties

To test the influence of graphene on the mechanical properties and structural anisotropy, the tensile properties of each sample were determined in both the XY (longitudinal) and Z (transverse) directions. Table 4.1 presents the tensile properties, including ultimate strength, modulus and elongation at break for all of the samples in the Z orientation. Figures 4.5 - 4.8 show the ultimate stress and modulus of the PLA and graphene composites with different graphene loadings for both the XY and Z directions at different bed temperatures.

The ultimate strength in the Z direction for the composite shows a slight increase with different graphene loadings relative to PLA when printed on a bed that is 70 °C. The ultimate strength in the XY direction shows a ~17% increase with 0.5% graphene loading relative to the pure PLA sample, when printed on a

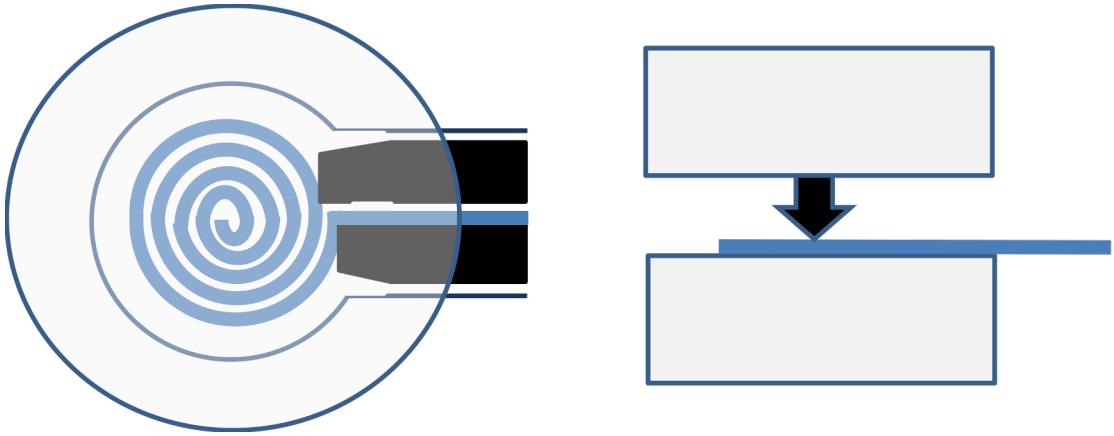

Figure 4.4: Diagram describing the TPS instrument setup and sensor position between sample pieces.[124]

.

Table 4.1: Tensile properties of printed samples in the Z (transverse) direction.

	Ultimate strength (MPa)	Modulus (GPa)	Elongation(mm)
PLA Z 70	28.5	0.65	0.042
PLA Z 85	36.2	0.63	0.083
PLA Z 100C	24.8	0.6	0.041
Gra Z 0.5% 70C	28.6	0.72	0.064
Gra Z 0.5% 85C	44.6	0.82	0.090
Gra Z 0.5% 100C	40.9	0.59	0.089
Gra Z 1% 70C	31.1	0.65	0.051
Gra Z 1% 85C	30.4	0.6	0.059
Gra Z 2% 70C	30.2	0.67	0.050
Gra Z 2% 85C	22.9	0.62	0.040

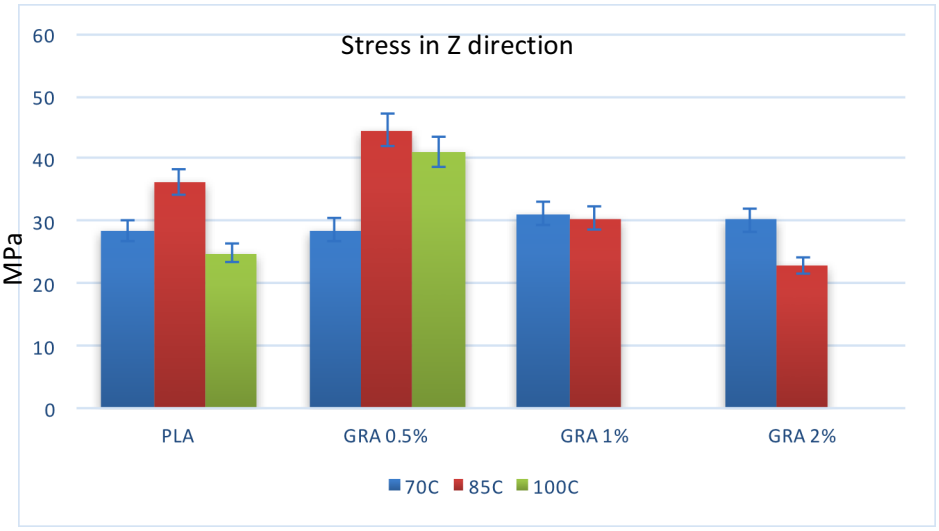

Figure 4.5: Ultimate stress of each printed sample for samples printed in the Z direction.

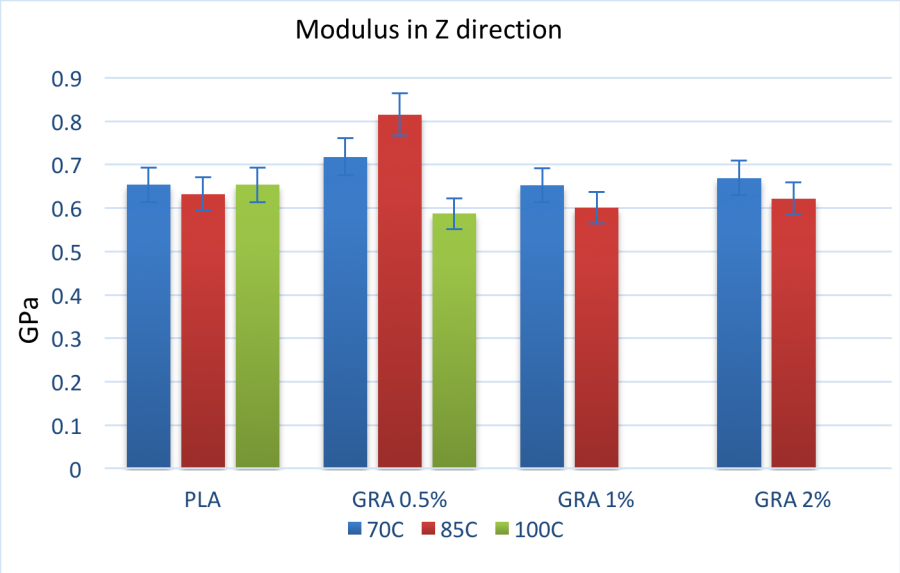

Figure 4.6: Modulus of each printed sample for samples printed in the Z direction.

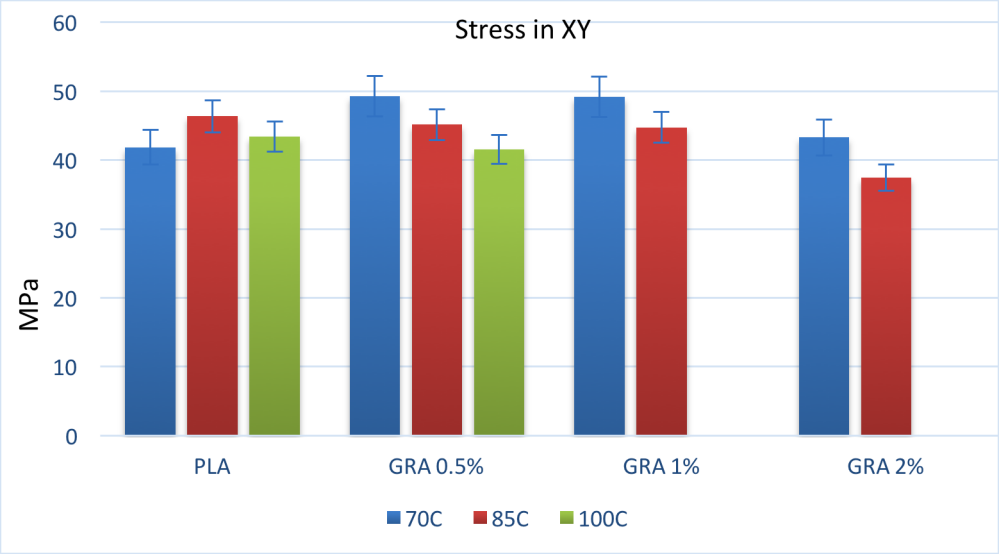

Figure 4.7: Ultimate stress of each printed sample for samples printed in the XY orientation.

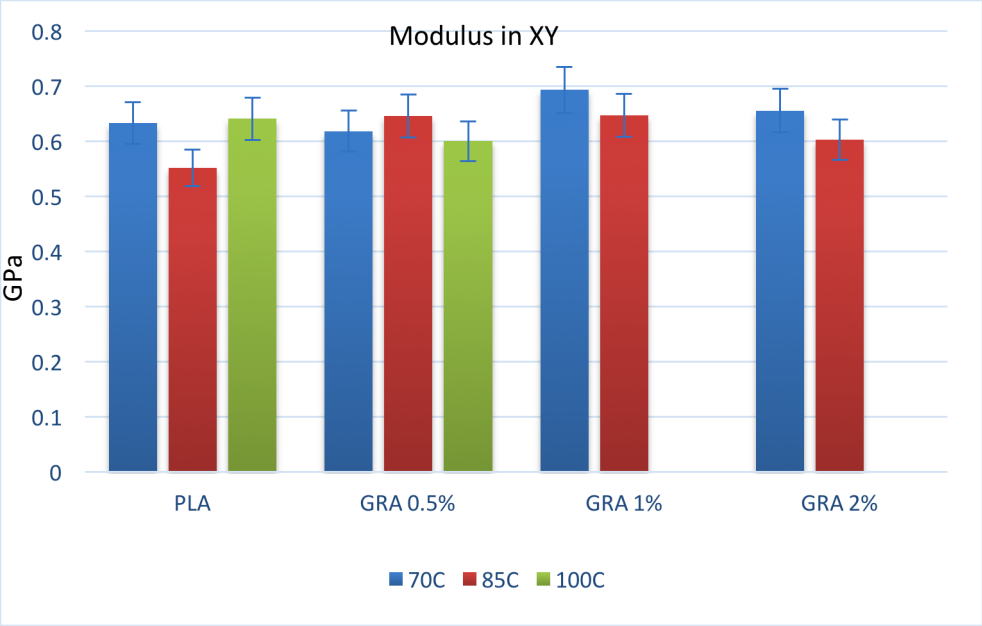

Figure 4.8: Modulus of each printed sample for samples printed in the XY orientation.

bed temperature of 70 °C. However, all samples exhibit anisotropic behavior when printed on the bed that is 70 °C. Interestingly, increasing the bed temperature from 70 to 85 °C increases the ultimate strength in the Z direction by 27% for PLA and by 56% for the 0.5% graphene composite and a more isotropic sample is achieved with 0.5% graphene. The modulus in both the Z and XY direction also increased by as much as ~25% with increasing bed temperature for the 0.5% graphene sample. This interesting result highlights the effect of the graphene and thermal properties of the printed polymer during printing and its influence on the Z strength, where the incorporation of graphene and the increase in heat input by the bed lead to significant improvement in Z strength. It is worth noting that increasing bed temperature didn't show further enhancements in strength for the XY orientation demonstrating that improvements in heat transfer primarily affect the structure and properties in the Z direction. Another important observation is the deterioration in Z strength with increasing bed temperature from 85 to 100°C for the pure PLA. This could be attributed to increase in warping and roughness of the surface as PLA deforms significantly at high temperatures. However, increasing the bed temperature for the 0.5% graphene did not reduce Z strength as significantly. Additionally, the improvements in strength of the sample in the Z direction with increasing bed temperature did not continue with increased graphene loadings of 1% and 2%. This could be attributed to segregation of graphene at the interface with higher loadings above 0.5%, which may inhibit inter-filament diffusion. Moreover, segregated graphene sheets at the interface can act as stress points

and weaken the interface and inhibit entanglements. Similarly, the addition of the graphene may increase the viscosity of the composite and slow down of polymer chain diffusion at higher loadings. It is also important to note that at low graphene loadings, reasonable dispersion can be achieved and the graphene sheets can form a network inside the polymer and significantly impact thermal properties of the materials.[59]

Determination of Interfilament Voids

In order to provide a foundation to understand the changes in the mechanical properties with incorporation of graphene, SEM was used to quantify the amount of voids in the printed samples. Figures 4.9 and 4.10 show the void spaces between filaments in neat PLA and in the 0.5% graphene composite in the Z direction and XY direction, respectively, for samples printed with a bed temperature of 70 and 85°C. Large voids are present in the pure PLA specimens, which results in weak adhesion between layers due to the limited inter-filament polymer diffusion that occurs during the printing process. The addition of graphene leads to significant reduction in void spacing in between filaments for both bed temperatures, which should result in improved interlayer adhesion. The amount of voids in the samples was quantified using Image J software to analyze these SEM images. Figure 4.11 shows the analysis of the SEM images and Table 4.2 presents the percent voids that exists in the pure PLA and the graphene composites. These results show that there is a significant reduction of more than 80% in void space for the 0.5% graphene sample relative to pure PLA. It is interesting that the higher

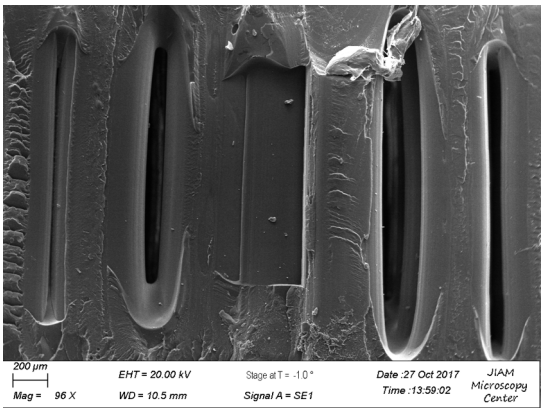

(a)

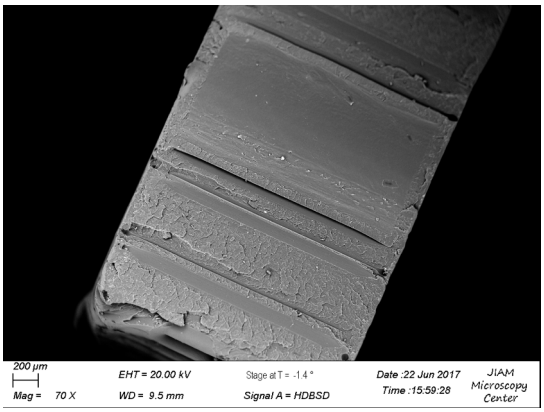

(b)

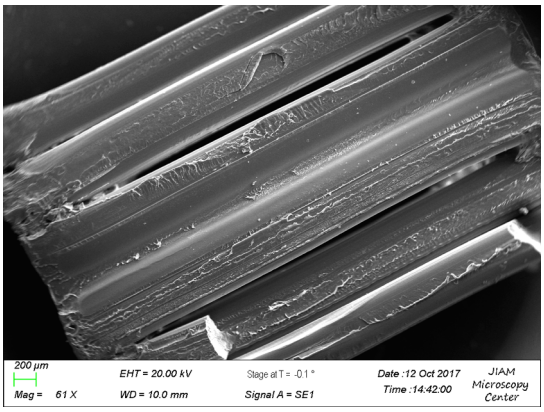

(c)

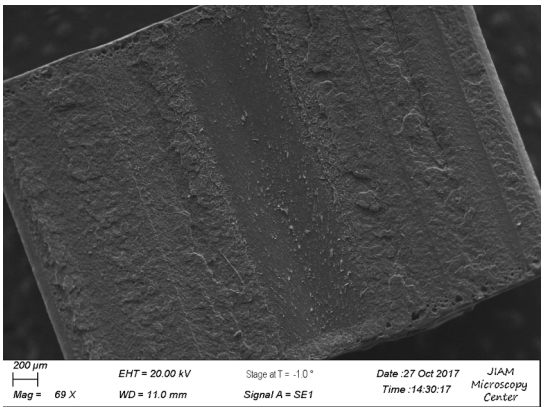

(d)

Figure 4.9: SEM images of the inter-filament voids in the Z orientation for a) PLA printed at 70 C bed temperature b) 0.5% graphene composite printed at 70 °C C) PLA printed at 85 °C bed temperature d) 0.5% graphene composite printed at 85 °C bed temperature.

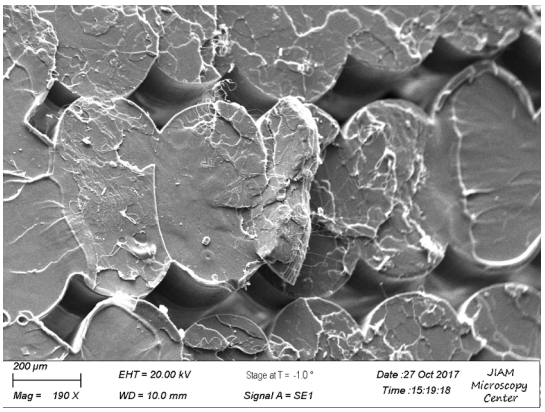

(a)

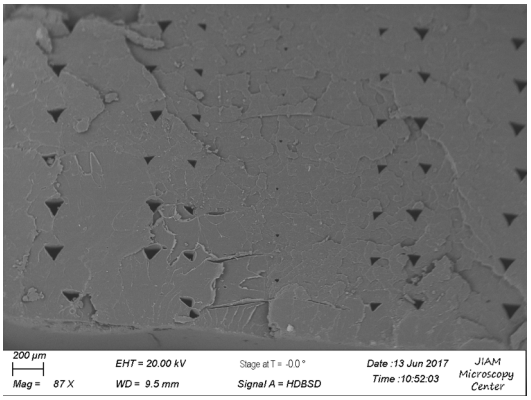

(b)

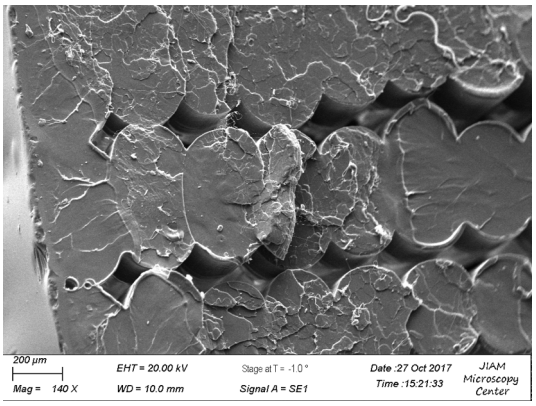

(c)

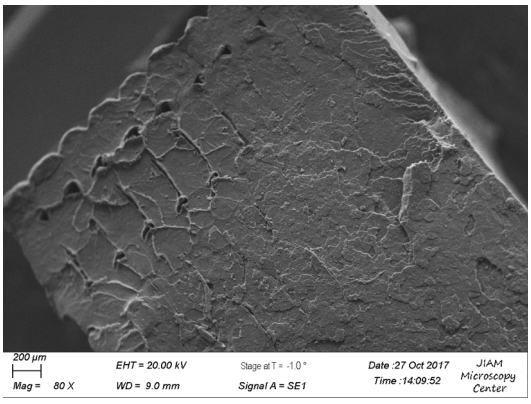

(d)

Figure 4.10: SEM images of the inter-filament voids in the XY orientation for a) PLA printed at 70 °C bed temperature b) 0.5% graphene composite printed at 70 °C bed temperature c) PLA printed with an 85 °C bed temperature d) 0.5% graphene composite printed with an 85 °C bed temperature.

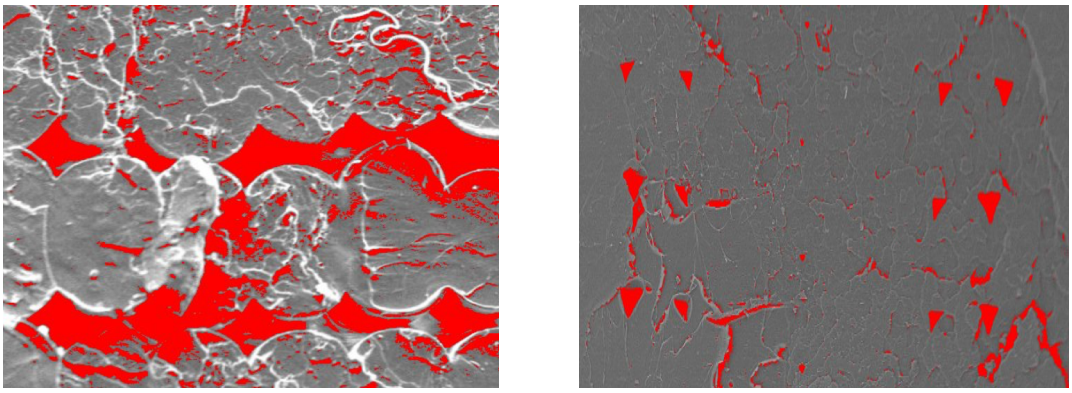

(a) **(b)**

Figure 4.11: Image J analysis of voids for samples in the XY orientation a) PLA printed on a bed temperature of 70 °C b) 0.5% graphene composite printed on a 70 °C bed.

Table 4.2: % Voids in the XY Direction for all samples.

Sample	Percent Void (70°C bed)	Percent Void (85°C bed)
PLA	22.5	11
0.5% Graphene	8	4
1% Graphene	17.5	12
2% Graphene	19	14

graphene loadings show only modest reduction in the amount of voids (15-22%) and that the amount of voids qualitatively correlates to the mechanical properties of the samples.

Monitoring the Thermal Profile

Thermal profiles were extracted from videos captured at different printing times. Figures 4.12 and 4.13 show the thermal profiles of the PLA and graphene nanocomposites cube at two different times during printing. These prints all had the same extrusion temperature of 190°C and bed temperature of 70°C. In Figures 4.12 and 4.13 the thermal profiles of the cube are plotted as function of pixel, which correlates to the height of the cube from the print bed, where pixel 0 is at the bed and thus the first layer. The temperature at pixel 20 in Figure 4.12 monitors the temperature of the top layer as soon as the extrusion head moves away. Several interesting phenomena are clear in these plots, including that the temperature of top layer varies between 135°C for PLA and 140°C for the 2% graphene composite. The variation in the top layer temperature between PLA and the composites also increases with increasing printing time as shown in Figure 4.13. This can be explained by the improved heat transfer in the graphene composites, where the filament is heated to a higher temperature for a given print head temperature and residence time. Another key feature, is the bowed nature of the thermal profiles where the temperature of the cube is elevated at the bed and near the print head, but levels off in the middle of the cube. As the wall height increases the temperature for the middle layers drops to a steady temperature ~ 41°C for

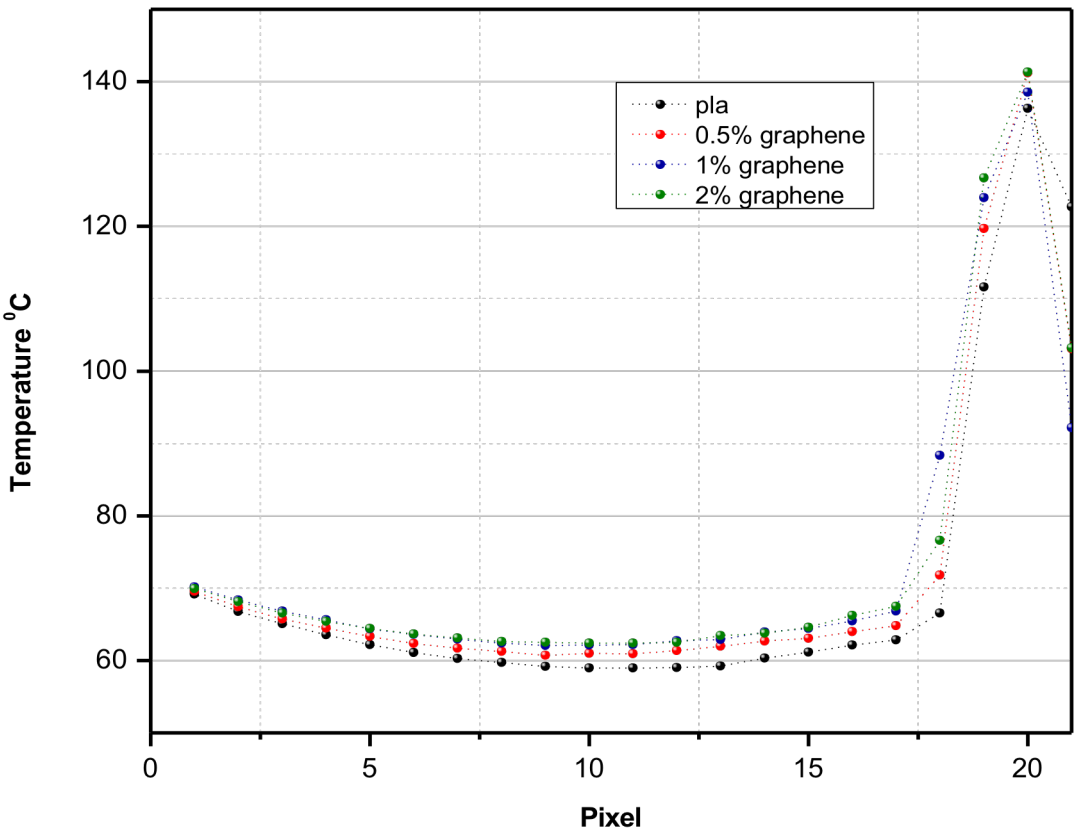

Figure 4.12: Thermal profile of the PLA and graphene composite cubes after 30 minutes of printing at 70 °C bed temperature.

.

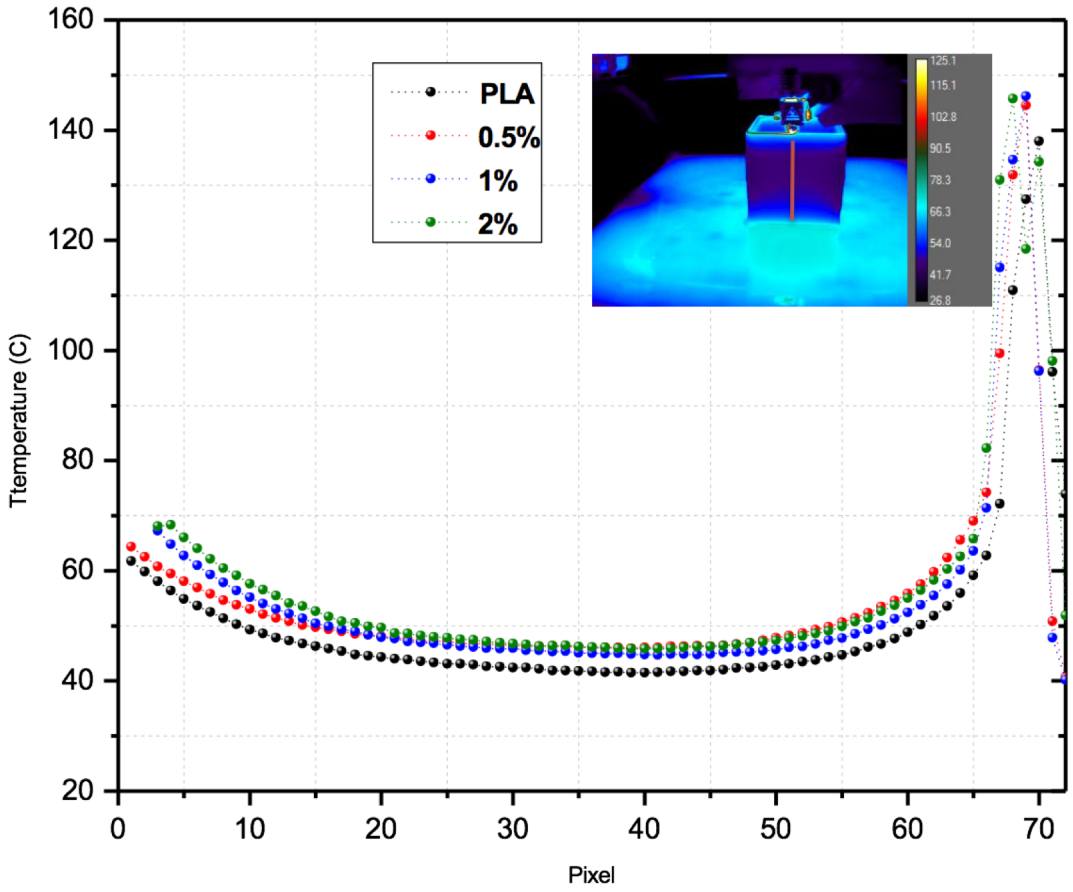

Figure 4.13: Thermal profile of the PLA and graphene composites cubes after 1 hour 30 minutes at 70 °C bed temperature.

PLA which is below the bed temperature, but this steady state value appears to increase with graphene content. Furthermore, the variation of temperature between neighboring filaments will contribute to the residual thermal stress built during printing where a more uniform profile should result in less residual stress.

Figure 4.14 shows the thermal profiles of the PLA and graphene composite cubes when the bed temperature is increased to 85°C. Increasing the bed temperature leads to an increase in the steady state temperature in the middle of the cube and an increase in the top layer extrusion temperature, particularly for the graphene composites.

Figure 4.15 compares the thermal profile of the PLA and 0.5% graphene composite cubes when printed on a bed temperature of 70°C and 100°C. Inspection of these thermal profiles reveals that the incorporation of graphene allows the print bed to input more heat onto the cube, leading to higher steady state temperature in the middle of the cube. The increase in the steady state temperature influences the top deposited layer temperature as well, suggesting that the incorporation of the graphene improves the heat transfer between filaments throughout the printing process, which in turn should improve the polymer diffusion and inter-filament bonding at the interface.

The improved heat transfer in the Z direction can be explained by an increase in thermal conductivity of the material upon incorporation of graphene. Although increasing the thermal conductivity may lead to quick initial heat decay for the deposited layers due to heat loss to surrounding ambient air through

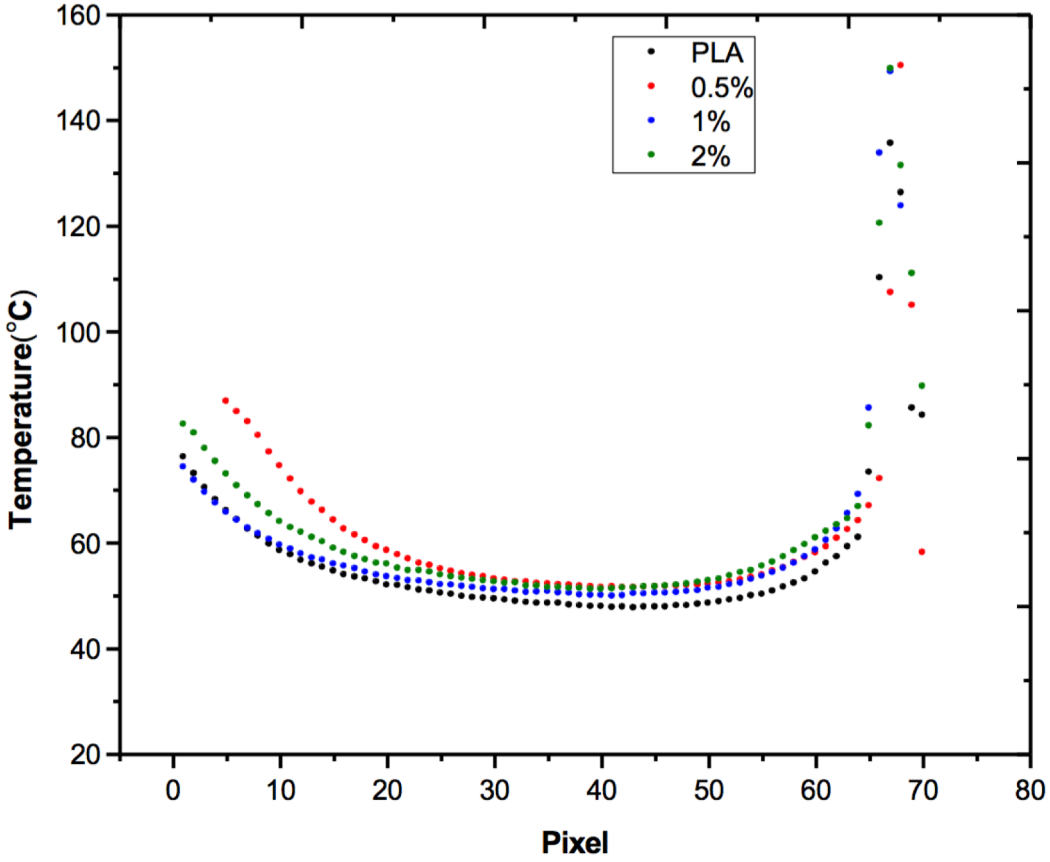

Figure 4.14: Thermal profiles after 1 hour 30 minutes of printing at 85 °C bed.

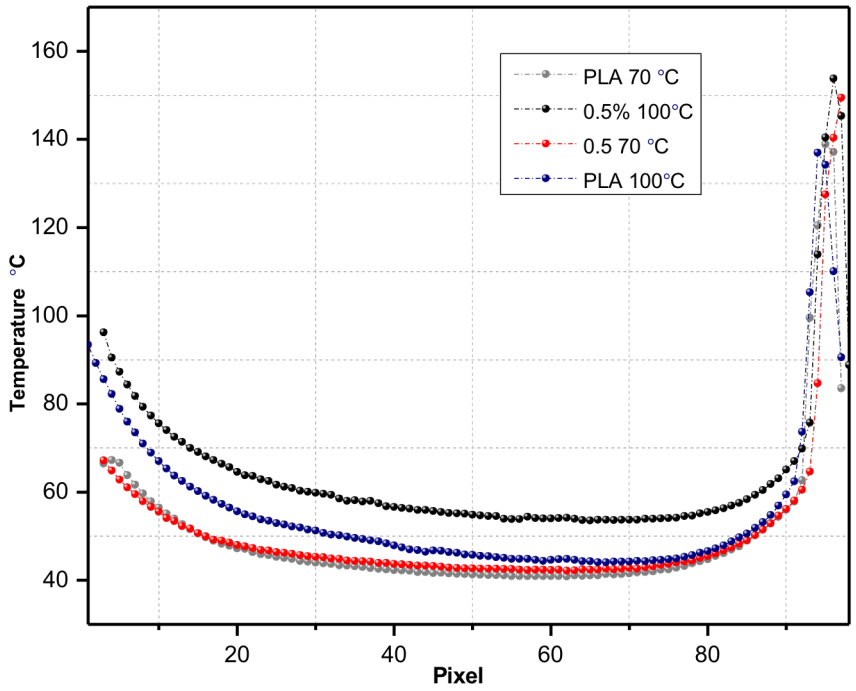

Figure 4.15: Thermal profiles for PLA and 0.5% composite at 70 °C and 100 °C bed temperature after 2 hours.

.

convection, the thermal profile appears to be dominated by the improved heat transfer from the bed and most recently deposited layer to maintain a higher steady state temperature in the middle of the cube through conduction.

Thermal Conductivity

Figure 4.16 shows the thermal conductivity of the PLA and graphene nanocomposites as measured at room temperature where a 20% increase in conductivity is achieved with the addition of graphene.

Analysis of Crystallinity

To further ensure that improvements in Z strength are not a result of changes in crystallinity of the PLA, DSC was used to evaluate the amount of crystallinity (X_c) in the pure PLA and the graphene composites, where Table 4.3 presents the percent crystallinity and thermal properties as evaluated from the DSC experiments. The addition of graphene does not significantly impact the T_g, which is not unexpected at such low loadings. To determine the percent crystallinity of the PLA, Equation 4.1 was used where ΔHm is enthalpy of fusion at T_m , and ΔHm^0 is the ideal enthalpy of melting for a 100% crystalline PLA sample which is 75 J/g. [42]

$$\%\ Crystallinty = \frac{\Delta Hm}{\Delta Hm^0} \text{ x } 100\% \qquad \text{Equation 4.1}$$

The addition of graphene up to 1% does not significantly alter the PLA crystallinity. Although some previous work has indicated that graphene can act as a nucleating agent and increase crystallinity, our results demonstrate that incorporating 2% graphene reduces crystallinity. [125] This may be attributed to the

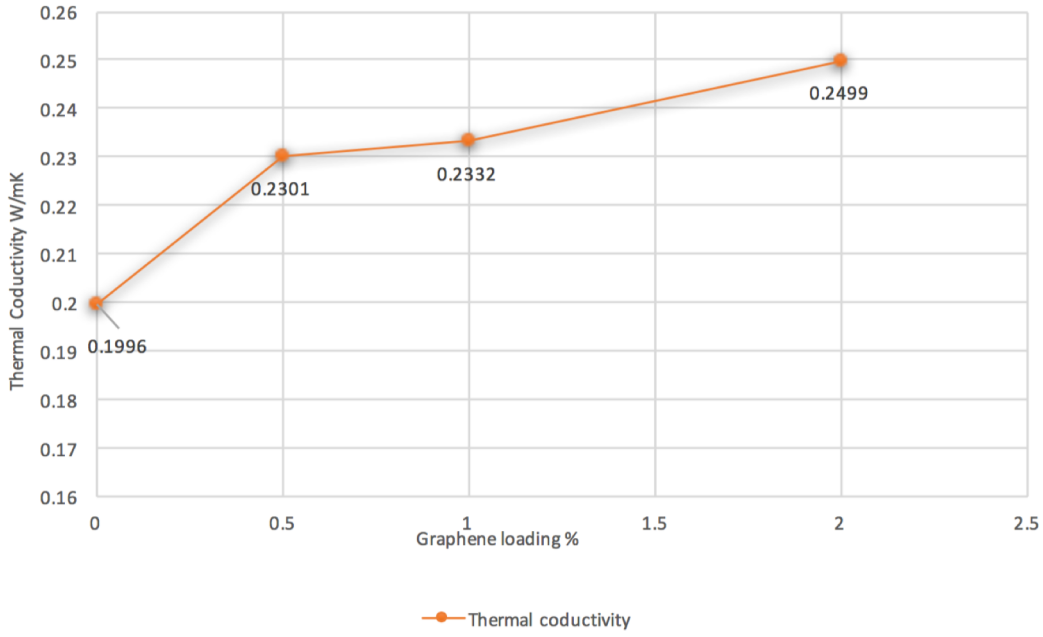

Figure 4.16: Thermal conductivity of printed composites at room temperature as function of Graphene loading.

.

Table 4.3: Thermal properties extracted from DSC curves.

	Tg	**T_m**	**ΔH_C**	**ΔH_m**	**X_c**
PLA	57.46	152.06	17.37	18.51	19.8
0.5%	57.56	150.70	18.76	18.49	19.8
1%	57.07	150.89	19.51	18.46	19.7
2%	57.60	151.82	12.77	12.07	12.9

formation of a graphene network that inhibit polymer chain motion and limits crystallization. It is clear that the changes in crystallinity do not correlate to the changes in mechanical properties, and thus, these changes are not related to variation in crystallinity.

Discussion

We present a set of results that document the effect of adding graphene to PLA in 3D printing, including the mechanical properties of printed objects and its impact on thermal profiles captured during printing. These results show that the incorporation of graphene in low concentrations can successfully enhance thermal conductivity of PLA as shown in Figure 4.16. These enhancements in thermal conductivity appear to alter the heat transfer in the Z direction during printing as demonstrated in the thermal profiles, which show that the sample may remain above T_g for longer time than pure PLA. Figure 4.15 shows a 10°C difference in steady state temperature between PLA and the 0.5% graphene composite printed at same bed and extrusion temperature. The temperature of the deposited top layer seems to also be influenced by the bed temperature, where the graphene composite shows an increase in the top layer temperature relative to that of PLA printed at same bed temperature. While improvements in heat transfer by conduction in the Z direction at a 70°C bed temperature led to a slight increase in Z–strength, increasing the bed temperature to 85 and 100°C lead to a 50% increase in strength for the 0.5% graphene composite where an isotropic sample is achieved. Surprisingly, these improvements are not observed with the 1 and 2%

composite. Although, the 2% composite exhibits a 20% improvement in thermal conductivity, the mechanical strength did not significantly improve with bed temperature. This result can be attributed to an inhibition of polymer chain diffusion between filaments with inclusion of higher graphene concentrations. Moreover, this may be exacerbated by the segregation of graphene to the filament interface that can further inhibit entanglements between filaments and lower the strength of the printed sample. The addition of carbon based fillers has been shown in the literature to have a profound effect on polymer diffusion, where the graphene nanoparticles can slow down dynamics and reduce polymer chain motion. Due to the 2D nature and anisotropic structure of the graphene sheets, they can act as large blockades to polymer motion and confine polymer chains.[63,99] Moreover, non covalent interactions that might occur between the graphene sheets and the polymer may also inhibit flow properties. [79,126,85]

It is worth mentioning that increasing the bed temperature didn't show any impact on the strength in the horizontal direction which further emphasizes the correlation between heat transfer by conduction in the Z direction and the strength across the inter-filament interfaces. To verify that the mechanical enhancements are not related to crystallinity changes within the composites, the crystallinity of the neat PLA and the composites were monitored. The data in Table 4.3 show very slight changes in crystallinity with different graphene loadings. Thus, it is clear that the variation in the Z strength are correlated more strongly to enhancements in

thermal conductivity and heat transfer that increase the extent in of inter-filament polymer diffusion.

This interpretation is further buttressed by the observed increased coalescence between solidified filaments and decrease in inter-filament void space. SEM provides direct evidence of the reduction in voids between filaments for the samples with 0.5% graphene loading. This data show a strong correlation between the reduction in void volume and bed temperature. Interestingly, the 1 and 2% graphene samples exhibit a more attenuated void reduction, which we ascribe to confinement of polymer chain motion by the higher loadings of the graphene, which limits inter-filament diffusion.

Current sintering models predict that slower cooling times of filaments increases neck growth and wetting between filaments. For ABS, extended periods of time above T_g allow for more molecular diffusion, and this directly affects inter-filament bonding.[39] However, in a polymer nano-composite, the addition of graphene may complicate this picture. Since diffusion is thermally driven and can be enhanced by increasing temperature, adding fillers that can improve thermal conductivity of the polymer might enhance diffusion and thus inter-filament coalescence. However, these same fillers may also confine the polymer chains that can slowdown the molecular dynamics of the polymer chains. The balance between these two factors appears to be very critical to successfully maximize interfilament bonding and adhesion at the inter-filament interface. The results presented here strongly suggest that 0.5% graphene loading balances these two

completing factors, but at 1 and 2% graphene loading, the slowing of polymer chain diffusion governs the inter-filament coalescence,

The importance of the print bed temperature on the observed thermal and structural properties is also interesting. Recent work with ABS suggests that the bed temperature is less important in determining inter-filament cooling rates than extrusion temperature.[17] This may differ for PLA due to its lower melting temperature. Our results demonstrate a direct correlation between the temperature profile of the printed filaments and bed temperature where this correlation is stronger for the composite due to its higher thermal conductivity. This discrepancy can be explained based of the theoretical models that describe the thermal evolution of the printed sample during printing. A commonly referenced model used to describe the cooling process of a filament upon leaving the extrusion head is a 2D model proposed by Rodriguez, that assumes perfect contact between filaments.[127] This has evolved to a 1D model where the filament cross section shape is modeled as an ellipse. This 1D model assumes a number of questionable assumptions, including a filament with finite length and infinite width, that the temperature is constant through the printed sample, and heat transfer between filaments is ignored.[44] These assumptions are not met in most samples printed by FDM, resulting in an underestimation for the heat transfer between filaments by conduction and its role on inter-filament bonding.[45,128] Our results demonstrate that increasing the thermal conductivity of the filament can lead to increase in heat transfer throughout the sample. This impacts the temperature of the top layer,

subsequently deposited layers, and their cooling trajectory. Thus, tuning the bed temperature combined with enhancing thermal conductivity of the composite and heat transfer between filaments can lead to drastic enhancements in interlayer adhesion and coalescence, which translates to improves interfilament adhesion and more robust printed structures.

Conclusion

The addition of graphene to PLA filament improves inter-filament bonding because of improved thermal conductivity, where the improved thermal transport translates to longer times at elevated temperatures. This increase in thermal conductivity improves the heat transfer in the z direction and creates a more homogeneous thermal profiles, especially at high bed temperatures where the composite samples remain above Tg for longer times during the print process. This results in more inter-filament diffusion of the polymers that manifests as stronger filament-filament interfaces, more robust and isotropic samples and fewer inter-filament voids. For instance, the samples printed at 85°C bed temperature with 0.5% graphene show significant improvement in the Z strength where an isotropic sample is produced.

However, the improvement only occurs at lower graphene loadings (~ 0.5%) because at higher loadings any increase in inter-filament polymer diffusion appears to be slowed by the presence of the graphene sheets – a well-known phenomenon in polymer nanocomposites. Thus, the results presented here indicate that using fillers with high thermal conductivity provides pathways to tailor

the thermal transport and profile during printing, effectively controlling heat transfer and offering a rational method to optimize the inter-filament interfaces and structural mechanical properties of printed structures.

CHAPTER 5

THE EFFECT OF GRAPHENE ON RESIDUAL STRESS AND IRREVERSIBLE THERMAL EXPANSION IN FDM PRINTED SAMPLES

Introduction

Due to the incremental nature of FDM and fast heating and cooling cycles of the material, a residual stress is accumulated inside the printed objects.[44,129,130] This accumulated stress can lead to delamination, warping, poor dimension accuracy, part distortion and consequently influence the quality and strength of the printed object. Moreover, the residual stress and thermal gradients that develop during the fabrication of prototypes by 3D printing are challenging problems that can lead to catastrophic failures for large scale printing. Several reports confirm that this accumulated residual stress can be relieved through annealing printed objects above T_g, where the polymer chains are free to move and can relieve stress through irreversible thermal expansion. For instance, annealing ABS printed rectangular prototypes at temperatures above T_g leads to thermal expansion in the Z direction (the direction perpendicular to the bed) and contraction in the y direction (direction parallel to the bed).[131] Residual stress and irreversible thermal strains were used interchangeably in literature where both are related through elastic coefficient of the material.

Although several works confirm this phenomenon as an inherent trait in FDM, the relation between printing parameters, filament orientation and material properties on the observed irreversible thermal strain are not very well understood. Previous studies investigated the effect of printing parameters such as raster angle, layer thickness and printing orientation on residual stress.[132] Peterson et al. examined irreversible thermal expansion in printed ABS with varying layer

thickness and examined the influence of layer thickness on mechanical properties and flexural strength of the printed objects. Their results suggest a strong correlation between layer thickness and residual stress with annealing. Decreasing layer thickness leads to an increase in irreversible thermal strain and poor mechanical properties. Samples that exhibit layer thickness below 0.35 mm show irreversible thermal strains up to 22% which implies a significant role of the interface on the observed strains. Interestingly, the calculated thermal strains based of the known thermal expansion coefficient of ABS is much less than experimentally obtained values, which suggests a strong and direct relation between printing parameters and observed thermal strains. [47]

In a different study, Karalekas et al. used a Bragg grating optical sensor to measure residual strains in FDM prototypes formed after cooling from the printing process. The sensor was embedded in the specimen mid-plane and internal strains were measured as a function of applied temperature. Their work studied the effect of raster angle and layer thickness on thermal strain. The recorded strains for samples with 0° raster angle (filament roads oriented in the specimen long direction) were lower relative to those with 90 ° and 45° raster angle for specimens with layer thickness of 0.25mm. Surprisingly, the raster orientation effect diminishes for specimens with 0.5mm layer thickness. These results demonstrate a strong correlation between layer thickness and residual strains where, layer thickness can impact how fast it cools down in air and affect overall thermal gradient developed in the printed samples. [132]

The material properties of the printed object, such as crystallinity and thermal conductivity, can have a great effect on the residual strains that are realized in FDM printing. Most recent work has confirmed large residual stresses in amorphous polymers such as ABS. However, semi crystalline polymers and composites have not been sufficiently investigated experimentally. For instance, cooling rates can have drastic effects on irreversible thermal strains in PLA due to changes in crystallinity and free volume.[129] The volume change in thermoplastic polymers can greatly depend on crystallinity. Change in volume of amorphous polymers is primarily due to changes in chain orientation and packing during cooling down from printing to ambient temperatures. In semi crystalline polymers volumetric changes can also be influenced by changes in polymer crystallization, which may increase residual stress and complicate the picture further. Since, PLA has promising applications in the biomedical industry where dimension accuracy is critical, more studies that address the problem of residual stress and provide solutions that can lead to residual stress reduction and better dimension stability are needed.

In this work we examine the effect of the addition of graphene to the filament on the residual stress in PLA objects that are fabricated by FDM. PLA filaments with different graphene loadings are used to print rectangular samples with the longest axis perpendicular to the bed. The samples were then annealed in an oven at 85 °C, after which irreversible thermal strains were recorded and correlated to

residual stress in the printed object to gain insight onto the effect of the material thermal properties of the nanocomposite filament on irreversible thermal strains.

Experimental

Materials

Natureworks PLA 4043D pellets (Filabot), Graphene Composite grade (Celtig), and Dimethyl Formamide (DMF) (Fisher Scientific), were all used as received.

Composite Fabrication

Graphene was added to DMF to give a concentration of 0.25 mg/ml. A sonication bath was then used for 24 hours to disperse the graphene sheets. PLA pellets were first dried and then added to the graphene solution to achieve loadings of 0.5, 1 and 2% graphene relative to the PLA. The solution was then gently heated and magnetically stirred to allow PLA to dissolve. The suspension was then dripped into a large amount of deionized water (V_{DMF}/V_{water} = 1:5) in a blender. Due to the poor solubility of PLA in water, the PLA precipitated immediately trapping the graphene sheets dispersed in the PLA matrix, where the quick precipitation method prevented graphene sheets from restacking. The composite was then filtered and left to dry in vacuum oven at 120°C for 24 hr. The dried composite was then pelletized and extruded at 168°C using Filabot single screw extruder. The filament diameter was maintained at 2.85 ± 0.1mm.

3D Printing and Thermal Annealing

A TAZ 5 3D printer was used to print the samples. The nozzle temperature was set at 190 °C and bed temperature was set at 70 °C for PLA and the composites. The sample dimensions of the rectangular structure were 50 mm (Z-axis) X 10 mm (Y axis) X 2mm (X axis) as shown in Figure 5.1.

The samples were printed with the Z axis perpendicular to the bed and with the raster angle 0°/90°. The layer thickness was 0.35 mm. After printing, the samples were allowed to cool down to ambient conditions prior to removing from the print bed. All samples were printed with a raft to allow better adherence to the bed. The samples were then annealed in an oven at 85°C for 30 minutes and an hour to record deformations of the samples. The annealing temperature was chosen to be slightly above the T_g of PLA as measured by DSC to be approximately 57°C. The dimensions of the samples were recorded before annealing and after cooling down from the annealing process. For the x and y axis, the measurements were taken at the z axis ends. Deformation due to release of the residual stress can then be calculated using the following equation.[131]

$$\varepsilon_{irrevrsible,thermal} = \frac{L_{annealed} - L_{innitial}}{L_{innitial}} \qquad \text{Equation 5.1}$$

Results and Discussion

Figure 5.2 show plots of the irreversible thermal deformation for PLA and the graphene nanocomposites as a function of graphene content for two annealing times. All samples show expansion in the Z direction with annealing and

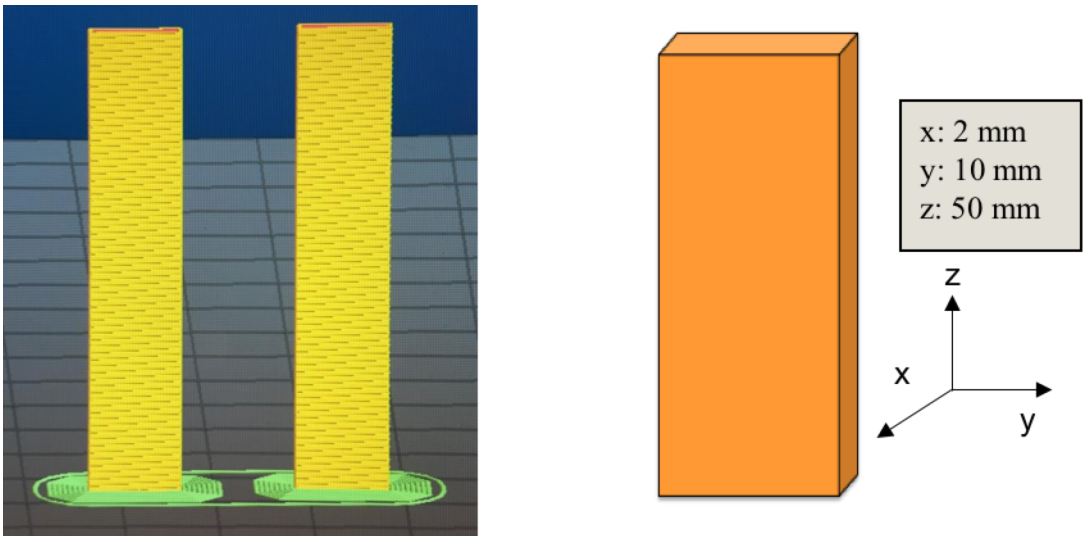

Figure 5.1: a) Illustration of the G code model of samples to monitor irreversible thermal expansion b) Geometry, orientation and dimensions of samples.

.

.

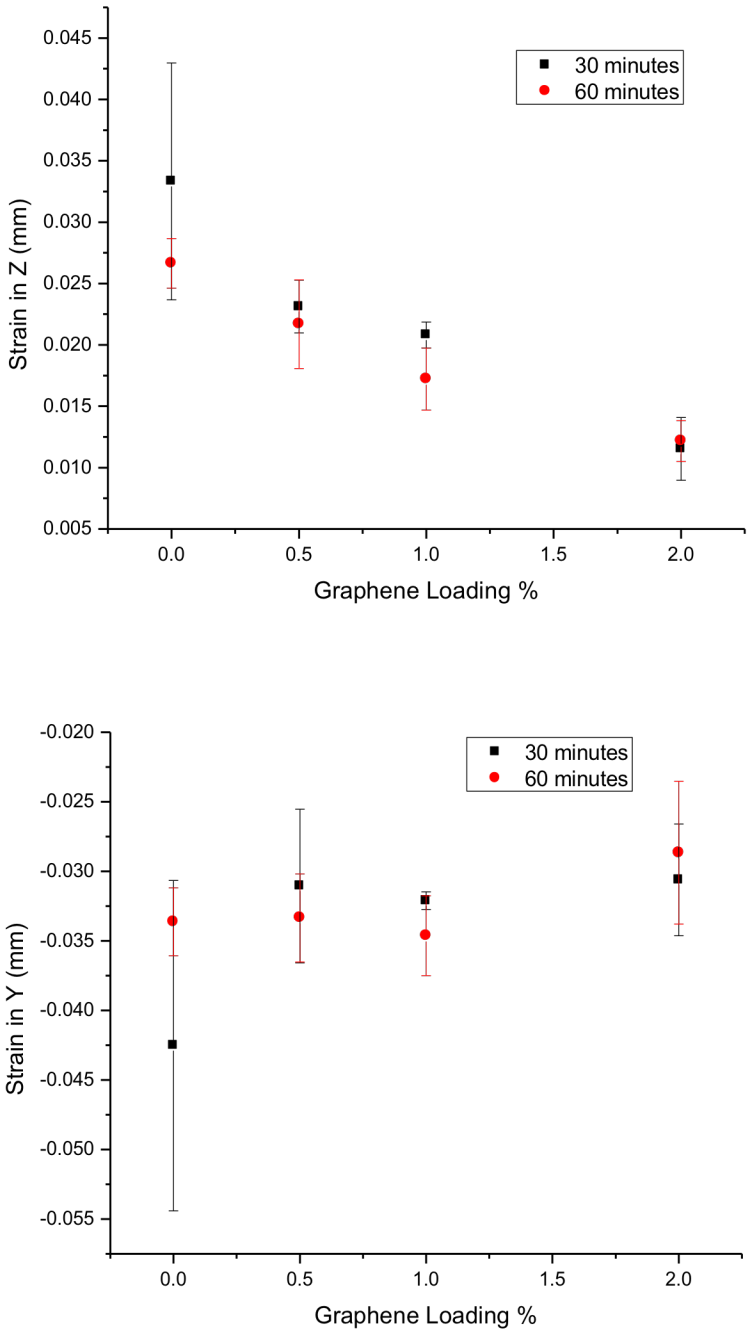

Figure 5.2: Irreversible thermal strain as a function of graphene loading in the z-direction (top) and xy-plane (bottom).

contraction in the y direction. Inspection of this plot shows that the the magnitude of expansion in the Z-direction of the pure PLA sample is greater than the expansion in the Z-direction for the nanocomposites, where the neat PLA sample expands by 3% expansion, while the 0.5% graphene nanocomposite sample expands by only 1%. The extent of expansion is reduced further by almost 50 % for the 2% graphene nanocomposite after 30 minutes of annealing. The reduction in expansion is also consistent for 1 hour of annealing. Interestingly, a clear trend is observed where increasing the graphene loadings leads to a gradual reduction in irreversible thermal expansion for both the z and the y directions. The irreversible thermal expansions obtained can then be related to residual stress inside the sample produced during printing with knowledge of the thermal expansion coefficient of the material and its elastic modulus using the following equations.

$$\varepsilon_{thermal} = \alpha \Delta T_1 \qquad \text{Equation 5.2}$$

$$\sigma_{residual\ stress} = E\alpha \Delta T_2 \qquad \text{Equation 5.3}$$

In these equations, α denotes the thermal expansion coefficient, ΔT_1 is the change in temperature between annealing and ambient conditions, E is the elastic modulus and ΔT_2 is the change between extrusion and ambient temperature.[131]

The calculated residual stress as measured in the Z-direction is shown in Figure 5.3, where significant reduction in residual stress is achieved with incorporation of graphene. To explain the observed accumulated residual stress during FDM printing process, we correlate stress to flow and stress that emerges

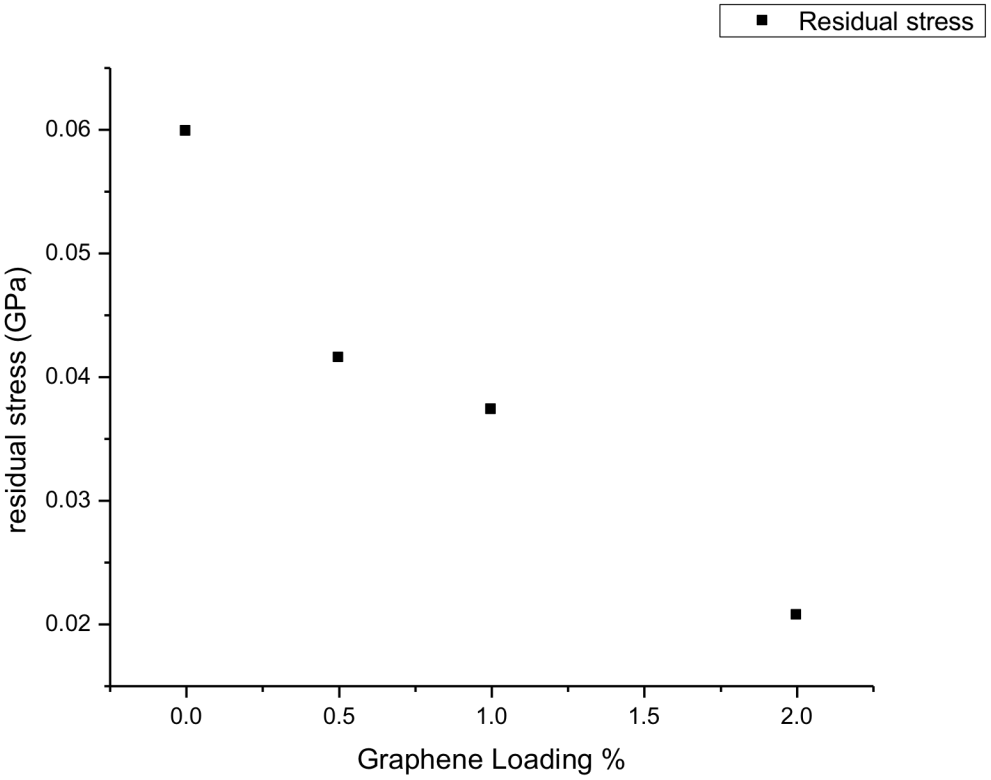

Figure 5.3: Residual stress in the z-direction as function of graphene loading.

.

due to thermal gradients in the printed samples. The residual stress induced by flow during printing is due to the alignment of polymer chains along the flow direction. In the quiescent molten state, the polymer chains exhibit a random coil packing, which become elongated in a shear field, as during the printing deposition process. As the material cools down quickly to ambient conditions, the polymer chains become trapped in this elongated unfavorable state leading to residual stress. As these prototypes are annealed above T_g the polymer chains gain enough mobility to return to its favorable, isotropic random coil state. This molecular level relaxation leads to an expansion of the sample perpendicular to the flow direction and a contraction along the filament flow direction.

Another contribution to the residual stress is created due to thermal gradients that develops across the sample during printing, leading to variation in cooling rates and a distribution of relaxation states. The heterogeneous cooling of the material includes the fast cooling of the surface by convection relative to the core that cools more slowly relying on conduction. The contraction for the core material is then restricted by the outer surface leading to trapped residual stress. Additionally, when a new layer is extruded at high temperature and laid down to solidify, where its contraction is usually restricted by its contact with cooler material underneath. This thermal gradient results in a mismatch in thermal expansion suggesting that better heat transfer between filaments through conduction can minimize temperature variations between neighboring layers, which should lead to a decrease in the residual stress.

Results in Chapter 4 show that the incorporation of graphene improves the thermal conductivity of the PLA filament, which in turn provides a more uniform thermal gradient along the height of a printed object. This increased thermal conductivity and more uniform thermal gradients of the graphene nanocomposites is consistent with the observed decrease in irreversible thermal expansion and residual stress in the graphene containing samples. Figure 5.4 shows the thermal gradient of samples printed using PLA and the graphene composites at bed temperature of 70°C where a more uniform thermal gradient is observed for the composites.

The expansion in the Z direction can be explained by Poisson's relation where a strain on one axis lead to same strain on the other axis but with a different sign, since the material resists changes in volume. Figure 5.5(a) show linear relation between the strain in y and z axis for PLA and composite with the Poisson's coefficient highlighting the anisotropic behavior of the samples.

Minimal changes in volume for the samples with annealing are shown in Figure 5.5(b). Previous studies on ABS showed similar results where slight variation in volume was observed that coincide with changes observed in the X axis. It is possible that the addition of fillers may lead to more alignment in polymer chains during printing under the shearing effect, however in this scenario the fillers can lead to more residual stress trapped within the prototypes due to being in this unfavorable state. Accordingly, the minimal changes in volume in our study suggests that the polymer chain alignments are not altered by the incorporation of

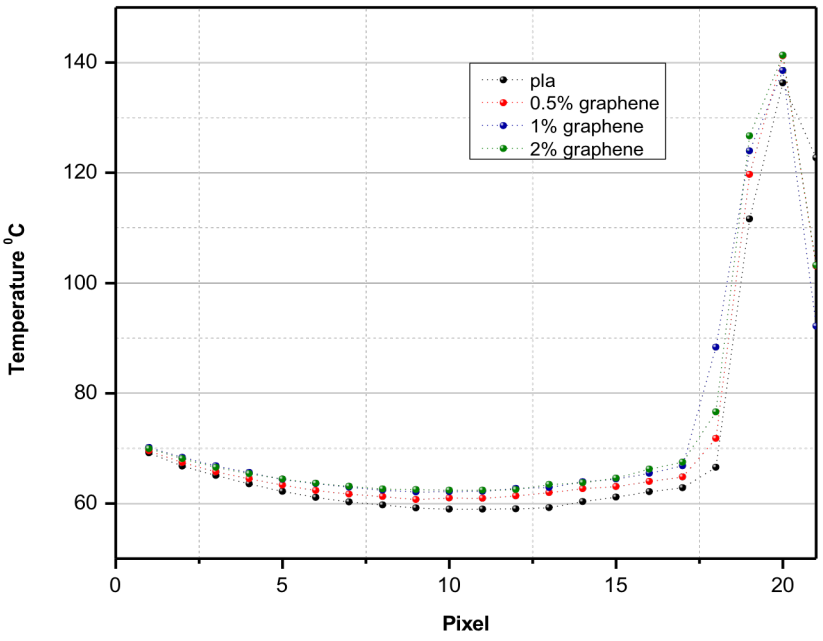

Figure 5.4: Thermal profiles of PLA and graphene composite samples during printing at bed temperature of 70 C°.

.

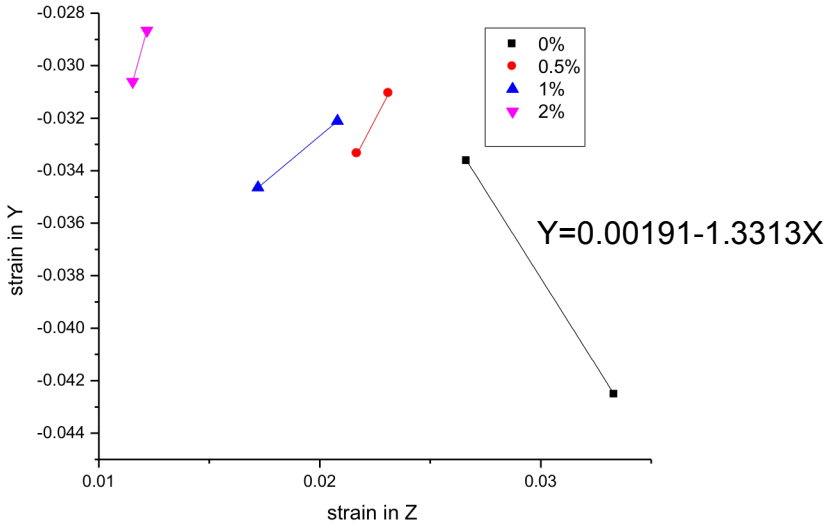

(a)

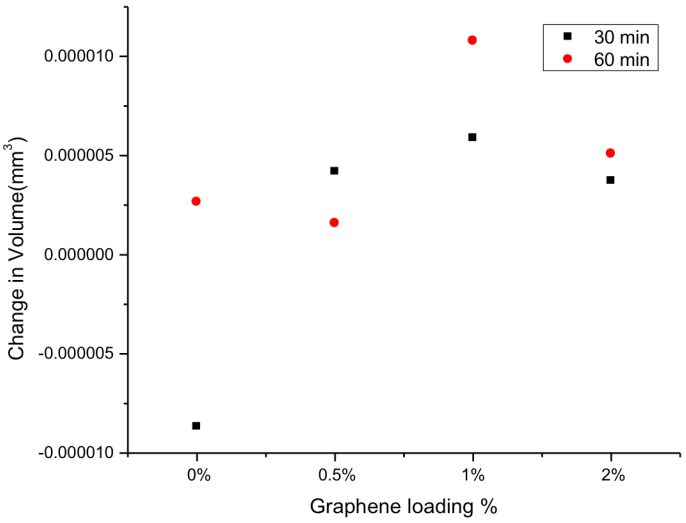

(b)

Figure 5.5: (a) Correlation of the strain in the Y-direction and the strain in the Z direction (b) The relative change in volume as function of graphene loading.

.

graphene and agree nicely with the reduction seen in residual strength for the graphene composite relative to the neat PLA. More experiments will be done to verify the alignment effect that graphene can have on polymers as PLA and ABS, which can further strengthen our argument.

Conclusion

In the presented work we examined the impact of graphene on residual stress and irreversible thermal expansion of PLA, to provide an insight onto the role of fillers in controlling dimensional accuracy and warping in 3D printing. Our results demonstrate that the incorporation of graphene in different concentrations reduces irreversible thermal expansion up to 50%. We explained this reduction as being correlated to residual stress developed during printing due to non uniform thermal gradient and poor heat transfer. This residual stress emerged due to fast cooling down of PLA where the polymer chains get trapped in an unfavorable elongated stretched state. The addition of graphene to the matrix enhances heat transfer by conduction and slows down the cooling rate of the laid filaments, allowing the polymer chains to return back to their favorable coiled state and hence reduce the trapped stress.

CHAPTER 6

CONCLUSION

Conclusions and Future Work

Polymer nanocomposites are a prominent area of research that is receiving significant interest. New potentially revolutionary industrial technologies demand new materials that exhibit extraordinary properties. The addition of fillers and nanoparticles that are nanoscale in size to the polymer matrix can improve their mechanical, electrical and thermal properties leading to superior materials relative to neat polymers. As the size of the nanoparticle decreases, the surface to volume ratio increases, leading to unusual changes in the dynamics and flow properties of the polymer matrix. Without a thorough knowledge of the impact of fillers and nanoparticles on the local and global dynamics of the polymer chains and the correlation between nanoparticle size and topology on mobility, the rational application of these nano additives to create materials with targeted properties will be challenging. Understanding the importance of several characteristics of the nanoparticle, including nanoparticle shape, size and polarity in determining the nanoparticle dispersion, local interactions and extent of polymer confinement is necessary to widen their application. Furthermore, the real application of fillers in new industrial technologies such as 3D printing necessitates further insight into their impact on the thermal, mechanical and flow properties of the surrounding polymer matrix. Therefore, the work in this dissertation focuses on understanding the physics that govern dynamics of entangled polymers with the inclusion of soft nanoparticles, and the impact of incorporating nanoscale additives in fused deposition modeling. This work has been accomplished through extensive

experimental studies that elucidate the impact of soft nanoparticle loadings on the diffusion of linear polymer chains, the correlation between soft PS nanoparticle topology and mobility and the consequence graphene has on inter-filament bonding and residual stress in fused deposition modeling.

The Impact of Soft Nanoparticle Concentration on Polymer Chain Diffusion

In this study, the diffusion of 535 K linear PS was monitored as function of nanoparticle concentration of a lightly crosslinked (~1%) soft polystyrene nanoparticle that consists of gel like cross-linked core with a fuzzy surface of PS chain ends. This chosen nanoparticle (NP1B) has a molecular weight of 238 K, which is 2 times lower than the matrix and is 20 nm in diameter which is larger than the reptation tube diameter. To monitor the interdiffusion across the bilayer interface, in-situ neutron reflectivity was used. The deuteration of one layer creates contrast and allows successful analysis of changes in vertical concentrations across the bilayer depth. The in-situ reflectivity technique involves the use of a temperature controlled chamber to anneal the sample at 130 °C quickly with no overshoot and with continuous acquisition of reflectivity curves with time. The technique allows us to study diffusion at short and long annealing times to ensure the system attains center of mass diffusion and allows the accurate determination of Fickian diffusion coefficients. Our results confirm that the soft nanoparticle increases the diffusion of the linear matrix at low concentrations, however with increase in nanoparticle loading and the extent of confinement, the increase in polymer diffusion is mitigated. Below a critical concentration of 1%, the diffusion of

the matrix doubles, however above 1% the increase in diffusion of the linear chain is attenuated as the nanoparticles confine the polymer chain. The increase in diffusion in this system was attributed to a constraint release mechanism similar to arm retraction in star polymers. The nanoparticle in our study includes a fuzzy interface of short polymer chain ends. These short chain ends move on a time scale that is faster than the reptation of the polymer chains of the matrix leading to a dilation and rearrangement of the reptation tube.

At higher nanoparticle loadings, the diffusion of the linear polymer chain is controlled by the balance of the enhancement of chain motion by constraint release and the attenuation of chain motion due to confinement of the polymer by the neighboring nanoparticles. The confinement regime at high loading is explained by the entropy barrier model used for inorganic nanoparticle. Within this model the interparticle distances are assumed to be fixed and can be calculated based on the nanoparticle loading and diameter. The confinement at high loadings can then be expressed using a parameter ($ID/2R_g$) that reflects the importance of the relative size of the nanoparticle to that of the matrix. Plotting the normalized diffusion as a function of the confinement parameter results in a universal plot for inorganic nanoparticles. For our soft nanoparticles, the results do not fall on this universal scale and show a contradictory trend due to the acceleration of the diffusion at low loadings. However, the translation from an acceleration to a confinement regime seems to occur at a confinement parameter that is close to 1 validating the importance of the relative size of the nanoparticle to the matrix. It is also worth

mentioning that the diffusion of the polymer chains within the soft nanocomposite is never less than that of the neat polymer, thus the enhancement effects are dominant in determining the diffusion of the linear polymer chain. Furthermore, the results also suggest that the attenuating confinement effects and enhancement processes are of similar magnitude. This unusual behavior in dynamics is fundamentally different than what has been reported for impenetrable inorganic nanoparticles and it highlights the uniqueness of this class of nanoparticles that can alter the dynamics of the matrix in a distinctive manner based on their loading in the matrix.

Future Work

Future work will focus on understanding the effect of loading that other soft nanoparticles may have on the diffusion of the linear matrix. Soft nanoparticles with smaller radii and matrices with different molecular weights can be analyzed to examine the impact of confinement and test whether the trend of dynamic transition from acceleration to confinement is universal for this class of all-polymer nanocomposites. Further work will also study the impact of the soft nanoparticle loading on the flow of polymer matrix at larger length scales using rheology. Other studies will also explore the impact of soft nanoparticles on the elastic modulus and other macroscopic properties of soft nanocomposites.

The Importance of Nanoparticle Softness on its Tracer Diffusion Coefficient

Determination of the soft nanoparticle mobility within the polymer matrix is a challenging problem due to the lack of contrast between the matrix and the

nanoparticle as well as the slow mobility of the nanoparticle relative to that of the linear polymer matrix. In this work, a protocol to determine the tracer diffusion coefficient of the soft nanoparticles in a linear 535 k polymer matrix is developed. Using neutron reflectivity, the mutual diffusion that represents the mutual motion of the polymer and the nanoparticle is determined. The mutual diffusion coefficient is then further analyzed using the Fast or Slow mode theories to extract the individual tracer diffusion coefficient of the soft nanoparticle. The Slow mode theory describes the behavior of our system owing to the fact that the mutual diffusion in this high molecular weight system is controlled by the diffusion of the slowest component, which is the nanoparticle. This experimental protocol was completed for wide range of nanoparticles that vary in topology based of their crosslinking density and molecular weight. Moreover, by monitoring the diffusion coefficient of nanoparticles with identical crosslinking density, and thus softness, for multiple molecular weights provides a pathway to examine the importance of nanoparticle softness on its diffusive properties. The results show that the motion of the nanoparticle is linked to its softness and therefore deformability. For a given molecular weight, increasing the crosslinking density of the nanoparticle increases its hardness and suppresses its diffusive motion in a linear matrix, emphasizing the importance of the deformability of the nanoparticle as well as its effective fuzziness on the nanoparticle motion. The molecular weight dependence of the nanoparticle varies with nanoparticle softness and deviates from the exponential molecular dependence for star polymer diffusion. Consequently, it appears that the

diffusion of these nanoparticles is similar to fractal microgels that can take advantage of the cooperative motion of the matrix to open pathways for the nanoparticle to diffuse. The comparison of diffusion of these nanoparticles to their estimated diffusion based on Stokes-Einstein for a hard sphere with similar radii shows significant deviation, where the soft nanoparticles diffuse much slower than the hard spheres. These results suggest that the simple friction factor in Einstein formula does not capture the motion of these nanoparticles where the fuzzy interface or entire nanoparticle may entangle with the polymer matrix leading to further suppression in motion.

Future Work

Future work will involve determination of the diffusion coefficient of soft nanoparticles in lower molecular weight matrix to test the role of matrix entanglements on diffusion and conformations adopted by the nanoparticle inside the matrix. Other studies will also include examining the diffusion of other soft nanoparticles in a linear polymer matrix with different topologies such as single chain nanoparticles, hyperbranched polymers and dendrimers.

Enhancing Inter-Filament Bonding of PLA via Graphene Reinforcement in Fused Deposition Modeling

In this work, the impact of the addition of graphene on inter-filament bonding and thermal conductivity of PLA is examined to address the anisotropy problem that FDM fabricated parts suffer from. The correlation between the thermal profiles developed during printing and the mechanical properties of the printed samples is

also studied, as well as the impact of bed temperature on the thermal gradients that evolve during printing and their correlation to mechanical properties of the printed parts. Our results show that the addition of graphene to PLA-filaments improves inter-filament bonding due to improved thermal conductivity where the improved thermal transport translates to longer times at elevated temperatures. The increase in thermal conductivity improves heat transfer in the z direction and creates a more homogeneous thermal profile especially at higher bed temperatures, where the composite samples remain above T_g for longer times during the printing process. These thermal improvements lead to more inter-filament diffusion of the polymer and thus, stronger filament-filament interface and a more robust structure. These improvements were also found in SEM images where fewer inter-filament voids were present in the better performing samples. The 0.5% graphene sample printed with 85 °C bed temperature shows significant improvement in the Z strength compared to the neat PLA sample, where a nearly isotropic sample has achieved in the 0.5% graphene sample. All improvements in structure and performance are achieved at low loadings of graphene (~0.5%). At higher graphene loading, the increase in inter-filament polymer diffusion appears to be slowed down by the presence of graphene sheets which is a well-known phenomenon in polymer nanocomposites. The work presented here, therefore, introduces a mechanism to tailor inter-filament adhesion via introducing fillers capable of enhancing thermal conductivity of the polymer.

Future Work

Future work will evaluate the effect of different printing parameters such as extrusion temperature, printing speed, and ambient conditions on the thermal transport in PLA and the composites during printing, and test their effects on mechanical properties of the printed protypes. Thermal models can then be established to predict the experimental thermal profiles to correlate specific printing conditions and nanocomposite characteristics to the thermal history of the sample during printing. A study can also be performed on polymer composites with carbon fibers and other well-known thermally conductive fillers. More work can also explore the possibility of using compatibilizers that can enhance dispersion of graphene and study their impact on flow and thermal conductivity of the polymer.

The Effect of Graphene on Residual Stress and Irreversible Thermal Expansion in FDM Printed Samples

This work examined the impact of graphene on the development of residual stress and irreversible thermal expansion of PLA during fused deposition modeling. This study provides crucial insight onto the role of fillers in controlling dimensional accuracy and warping in 3D printing. The results indicate that the incorporation of graphene at different concentrations reduces the irreversible thermal expansion of the printed part up to 50%. This reduction is attributed to reduction in residual stress developed during printing due to heterogeneous heat transfer and poor thermal conductivity of the polymer. The residual stress is developed due to the rapid cooling of the deposited PLA where the polymer chains

are trapped in an unfavorable elongated state. The incorporation of graphene enhances heat transfer during printing and slows down the cooling rate of the deposited filament, allowing the polymer chains to return back towards the favorable coiled state and hence reduced the trapped stress.

Future Work

Future work will focus on studying the impact of different additives on residual stress and evaluate their effect on voids spacing within the annealed samples using SEM. The impact of graphene on residual stress of other common polymers such as ABS will be tested as well. More work will study the change in the crystallinity of the polymer and the composite to evaluate the role of crystallinity and packing on changes in sample stress and volume.

REFERENCES

(1) Hussain, F.; Hojjati, M.; Okamoto, M.; Gorga, R. E. Review Article: Polymer-Matrix Nanocomposites, Processing, Manufacturing, and Application: An Overview. *J. Compos. Mater.* **2006**.

(2) Müller, K.; Bugnicourt, E.; Latorre, M.; Jorda, M.; Echegoyen Sanz, Y.; Lagaron, J.; Miesbauer, O.; Bianchin, A.; Hankin, S.; Bölz, U.; et al. Review on the Processing and Properties of Polymer Nanocomposites and Nanocoatings and Their Applications in the Packaging, Automotive and Solar Energy Fields. *Nanomaterials* **2017**, *7* (4), 74.

(3) Kalsoom, U.; Nesterenko, P. N.; Paull, B. Recent Developments in 3D Printable Composite Materials. *RSC Advances*. 2016.

(4) Chiang, C.-L.; Ma, C.-C. M. *Polymer Nanocomposites*; 2006.

(5) Jordan, J.; Jacob, K. I.; Tannenbaum, R.; Sharaf, M. A.; Jasiuk, I. Experimental Trends in Polymer Nanocomposites - A Review. *Mater. Sci. Eng. A* **2005**, *393* (1–2), 1–11.

(6) Choi, J.; Hore, M. J. A.; Clarke, N.; Winey, K. I.; Composto, R. J. Nanoparticle Brush Architecture Controls Polymer Diffusion in Nanocomposites. *Macromolecules* **2014**, *47* (7), 2404–2410.

(7) Kuo, S. W.; Chang, F. C. POSS Related Polymer Nanocomposites. *Prog. Polym. Sci.* **2011**.

(8) Holley, D. W.; Ruppel, M.; Mays, J. W.; Urban, V. S.; Baskaran, D. Polystyrene Nanoparticles with Tunable Interfaces and Softness. *Polymer (Guildf).* **2014**, *55* (1), 58–65.

(9) Cheng, S.; Xie, S. J.; Carrillo, J. M. Y.; Carroll, B.; Martin, H.; Cao, P. F.; Dadmun, M. D.; Sumpter, B. G.; Novikov, V. N.; Schweizer, K. S.; et al. Big Effect of Small Nanoparticles: A Shift in Paradigm for Polymer Nanocomposites. *ACS Nano* **2017**, *11* (1), 752–759.

(10) Lin, C. C.; Gam, S.; Meth, J. S.; Clarke, N.; Winey, K. I.; Composto, R. J. Do Attractive Polymer-Nanoparticle Interactions Retard Polymer Diffusion in Nanocomposites? *Macromolecules* **2013**, *46* (11), 4502–4509.

(11) Holt, A. P. The Effect of Attractive Polymer-Nanoparticle Interactions on the Local Segmental Dynamics of Polymer Nanocomposites. **2016**.

(12) Holt, A. P.; Gri, P. J.; Bocharova, V.; Agapov, A. L.; Imel, A. E.; Dadmun, M. D.; Sangoro, J. R.; Sokolov, A. P. Dynamics at the Polymer/Nanoparticle Interface in Poly(2- Vinylpyridine)/Silica Nanocomposites. **2014**.

(13) Holt, A. P.; Bocharova, V.; Cheng, S.; Kisliuk, A. M.; Ehlers, G.; Mamontov, E.; Novikov, V. N.; Sokolov, A. P. Interplay between Local Dynamics and Mechanical Reinforcement in Glassy Polymer Nanocomposites. *Phys. Rev. Mater.* **2017**, *1* (6), 062601.

(14) Stevens, M. P. Polymer Additives: Part I. Mechanical Property Modifiers. *J. Chem. Educ.* **1993**, *70* (6), 444.

(15) Ciprai, D.; Jacob, K.; Tannenbaum, R. Characterization of Polymer Nanocomposite Interphase and Its Impact on Mechanical Properties. *Macromolecules* **2006**, *39* (19), 6565–6573.

(16) Jancar, J.; Douglas, J. F.; Starr, F. W.; Kumar, S. K.; Cassagnau, P.; Lesser,

A. J.; Sternstein, S. S.; Buehler, M. J. Current Issues in Research on Structure-Property Relationships in Polymer Nanocomposites. *Polymer*. 2010.

(17) Arbe, A.; Pomposo, J. A.; Moreno, A. J.; LoVerso, F.; González-Burgos, M.; Asenjo-Sanz, I.; Iturrospe, A.; Radulescu, A.; Ivanova, O.; Colmenero, J. Structure and Dynamics of Single-Chain Nano-Particles in Solution. *Polymer (Guildf).* **2016**, *105*, 532–544.

(18) Russell, T. P.; Karim, A.; Mansour, A.; Felcher, G. P. Specular Reflectivity of Neutrons by Thin Polymer Films. *Macromolecules* **1988**, *21* (6), 1890–1893.

(19) Nelson, A. Co-Refinement of Multiple-Contrast Neutron/X-Ray Reflectivity Data Using MOTOFIT. *J. Appl. Crystallogr.* **2006**, *39* (2), 273–276.

(20) Russell, T. P. On the Reflectivity of Polymers: Neutrons and X-Rays. *Phys. B Condens. Matter* **1996**, *221* (1–4), 267–283.

(21) Mangal, R.; Srivastava, S.; Narayanan, S.; Archer, L. A. Size-Dependent Particle Dynamics in Entangled Polymer Nanocomposites. *Langmuir* **2016**.

(22) Cai, L. H.; Panyukov, S.; Rubinstein, M. Hopping Diffusion of Nanoparticles in Polymer Matrices. *Macromolecules* **2015**.

(23) Grabowski, C. A.; Mukhopadhyay, A. Size Effect of Nanoparticle Diffusion in a Polymer Melt. *Macromolecules* **2014**.

(24) Senses, E.; Ansar, S. M.; Kitchens, C. L.; Mao, Y.; Narayanan, S.; Natarajan, B.; Faraone, A. Small Particle Driven Chain Disentanglements in Polymer

Nanocomposites. *Phys. Rev. Lett.* **2017**.

(25) Senses, E.; Narayanan, S.; Mao, Y.; Faraone, A. Nanoscale Particle Motion in Attractive Polymer Nanocomposites. *Phys. Rev. Lett.* **2017**.

(26) Senses, E.; Faraone, A.; Akcora, P. Microscopic Chain Motion in Polymer Nanocomposites with Dynamically Asymmetric Interphases. *Sci. Rep.* **2016**, *6*.

(27) Shatrohan Lal, R. K. Synthesis of Organic Nanoparticles and Their Applications in Drug Delivery and Food Nanotechnology: A Review. *J. Nanomater. Mol. Nanotechnol.* **2014**, *03* (04).

(28) Tuteja, A.; Mackay, M. E.; Hawker, C. J.; Van Horn, B. Effect of Ideal, Organic Nanoparticles on the Flow Properties of Linear Polymers: Non-Einstein-like Behavior. *Macromolecules* **2005**.

(29) Colley, F. R.; Collins, S. A.; Richards, R. W. Tracer Diffusion of Four Arm Polystyrene Star Molecules into Linear and Star Polymer Matrices from Nuclear Reaction Analysis. In *Journal of Materials Chemistry*; 2003.

(30) Lyon, C. K.; Prasher, A.; Hanlon, A. M.; Tuten, B. T.; Tooley, C. A.; Frank, P. G.; Berda, E. B. A Brief User's Guide to Single-Chain Nanoparticles. *Polymer Chemistry*. Royal Society of Chemistry January 14, 2015, pp 181–197.

(31) Senses, E.; Tyagi, M.; Pasco, M.; Faraone, A. Dynamics of Architecturally Engineered All-Polymer Nanocomposites. *ACS Nano* **2018**.

(32) Martin, H. J.; White, B. T.; Yuan, G.; Saito, T.; Dadmun, M. D. Relative Size

of the Polymer and Nanoparticle Controls Polymer Diffusion in All-Polymer Nanocomposites. *Macromolecules* **2019**, *52* (7), 2843–2852.

(33) Martin, H. J.; White, B. T.; Scanlon, C. J.; Saito, T.; Dadmun, M. D. Tunable Synthetic Control of Soft Polymeric Nanoparticle Morphology. *Soft Matter* **2017**, *13* (46), 8849–8857.

(34) Index, B. C.; Collection, C. TOP 1 %. 2–14.

(35) Srivastava, V. K. A Reviev on Advances in Rapid Prototype 3D Printing of Multi-Functional Applications. *Sci. Technol.* **2017**, *7* (1), 4–24.

(36) Chen, Q.; Mangadlao, J. D.; Wallat, J.; De Leon, A.; Pokorski, J. K.; Advincula, R. C. 3D Printing Biocompatible Polyurethane/Poly(Lactic Acid)/Graphene Oxide Nanocomposites: Anisotropic Properties. *ACS Appl. Mater. Interfaces* **2017**, *9* (4), 4015–4023.

(37) Nikzad, M.; Masood, S. H.; Sbarski, I. Thermo-Mechanical Properties of a Highly Filled Polymeric Composites for Fused Deposition Modeling. *Mater. Des.* **2011**, *32* (6), 3448–3456.

(38) Li, Y.; Gao, S.; Dong, R.; Ding, X.; Duan, X. Additive Manufacturing of PLA and CF/PLA Binding Layer Specimens via Fused Deposition Modeling. *J. Mater. Eng. Perform.* **2018**, *27* (2), 492–500.

(39) Bellehumeur, C.; Li, L.; Sun, Q.; Gu, P. Modeling of Bond Formation Between Polymer Filaments in the Fused Deposition Modeling Process. *J. Manuf. Process.* **2004**, *6* (2), 170–178.

(40) Pollard, D.; Ward, C.; Herrmann, G.; Etches, J. Filament Temperature

Dynamics in Fused Deposition Modelling and Outlook for Control. *Procedia Manuf.* **2017**, *11* (June), 536–544.

(41) Ahn, S. H.; Montero, M.; Odell, D.; Roundy, S.; Wright, P. K. *Anisotropic Material Properties of Fused Deposition Modeling ABS*; 2002; Vol. 8.

(42) Levenhagen, N. P.; Dadmun, M. D. Bimodal Molecular Weight Samples Improve the Isotropy of 3D Printed Polymeric Samples. *Polymer (Guildf).* **2017**, *122*, 232–241.

(43) Dul, S.; Fambri, L.; Pegoretti, A. Fused Deposition Modelling with ABS-Graphene Nanocomposites. *Compos. Part A Appl. Sci. Manuf.* **2016**, *85* (March), 181–191.

(44) Compton, B. G.; Post, B. K.; Duty, C. E.; Love, L.; Kunc, V. Thermal Analysis of Additive Manufacturing of Large-Scale Thermoplastic Polymer Composites. *Addit. Manuf.* **2017**, *17*, 77–86.

(45) Zhou, X.; Hsieh, S.-J. Thermal Analysis of Fused Deposition Modeling Process Using Infrared Thermography Imaging and Finite Element Modeling. **2017**, 1021409.

(46) Rizvi, G. M.; Bellehumeur, C. T.; Gu, P.; Sun, Q. Effect of Processing Conditions on the Bonding Quality of FDM Polymer Filaments. *Rapid Prototyp. J.* **2008**, *14* (2), 72–80.

(47) D'Amico, A.; Peterson, A. M. An Adaptable FEA Simulation of Material Extrusion Additive Manufacturing Heat Transfer in 3D. *Addit. Manuf.* **2018**, *21* (February), 422–430.

(48) Saravanan, N.; Rajasekar, R.; Mahalakshmi, S.; Sathishkumar, T. P.; Sasikumar, K.; Sahoo, S. Graphene and Modified Graphene-Based Polymer Nanocomposites - A Review. *J. Reinf. Plast. Compos.* **2014**, *33* (12), 1158–1170.

(49) Potts, J. R.; Dreyer, D. R.; Bielawski, C. W.; Ruoff, R. S. Graphene-Based Polymer Nanocomposites. *Polymer (Guildf).* **2011**, *52* (1), 5–25.

(50) Graphene Characterization and Analysis. **2013**.

(51) Mattevi, C.; Eda, G.; Agnoli, S.; Miller, S.; Mkhoyan, K. A.; Celik, O.; Mastrogiovanni, D.; Granozzi, G.; Carfunkel, E.; Chhowalla, M. Evolution of Electrical, Chemical, and Structural Properties of Transparent and Conducting Chemically Derived Graphene Thin Films. *Adv. Funct. Mater.* **2009**, *19* (16), 2577–2583.

(52) Hu, K.; Kulkarni, D. D.; Choi, I.; Tsukruk, V. V. Graphene-Polymer Nanocomposites for Structural and Functional Applications. *Prog. Polym. Sci.* **2014**, *39* (11), 1934–1972.

(53) Du, F.; Fischer, J. E. A Coagulation Method to Prepare Single-Walled Carbon Nanotube / PMMA Composites and Their Modulus , Electrical Conductivity , and Thermal Stability. **2003**, *41* (24), 3333–3338.

(54) Valapa, R. B.; Pugazhenthi, G.; Katiyar, V. Effect of Graphene Content on the Properties of Poly(Lactic Acid) Nanocomposites. *RSC Adv.* **2015**, *5* (36), 28410–28423.

(55) Ilic, O.; Jablan, M.; Joannopoulos, J. D.; Celanovic, I.; Buljan, H.; Soljačić,

M. Near-Field Thermal Radiation Transfer Controlled by Plasmons in Graphene. *Phys. Rev. B - Condens. Matter Mater. Phys.* **2012**, *85* (15), 1–4.

(56) Khanafer, K.; Vafai, K. Analysis of the Anomalies in Graphene Thermal Properties. *Int. J. Heat Mass Transf.* **2017**, *104*, 328–336.

(57) Luo, T.; Lloyd, J. R. Enhancement of Thermal Energy Transport across Graphene/Graphite and Polymer Interfaces: A Molecular Dynamics Study. *Adv. Funct. Mater.* **2012**, *22* (12), 2495–2502.

(58) Shahil, K. M. F.; Balandin, A. A. Graphene-Multilayer Graphene Nanocomposites as Highly Efficient Thermal Interface Materials. *Nano Lett.* **2012**.

(59) Li, A.; Zhang, C.; Zhang, Y. F. Thermal Conductivity of Graphene-Polymer Composites: Mechanisms, Properties, and Applications. *Polymers (Basel).* **2017**, *9* (9), 1–17.

(60) Meth, J. S.; Gam, S.; Choi, J.; Lin, C. C.; Composto, R. J.; Winey, K. I. Excluded Volume Model for the Reduction of Polymer Diffusion into Nanocomposites. *J. Phys. Chem. B* **2013**, *117* (49), 15675–15683.

(61) Choi, J.; Hore, M. J. A.; Meth, J. S.; Clarke, N.; Winey, K. I.; Composto, R. J. Universal {Scaling} of {Polymer} {Diffusion} in {Nanocomposites}. *ACS Macro Lett.* **2013**, *2* (6), 485–490.

(62) Mu, M.; Seitz, M. E.; Clarke, N.; Composto, R. J.; Winey, K. I. Polymer Tracer Diffusion Exhibits a Minimum in Nanocomposites Containing Spherical

Nanoparticles. *Macromolecules* **2011**, *44* (2), 191–193.

(63) Mu, M.; Clarke, N.; Composto, R. J.; Winey, K. I. Polymer Diffusion Exhibits a Minimum with Increasing Single-Walled Carbon Nanotube Concentration. *Macromolecules* **2009**, *42* (18), 7091–7097.

(64) Lin, C. Dynamics in Polymer Nanocomposites Containing Fixed and Mobile Nanoparticles Dynamics in Polymer Nanocomposites Containing Fixed and Mobile. **2015**.

(65) Li, Y.; Kröger, M.; Liu, W. K. Nanoparticle Effect on the Dynamics of Polymer Chains and Their Entanglement Network. *Phys. Rev. Lett.* **2012**, *109* (11), 1–5.

(66) Lin, C.-C.; Gam, S.; Meth, J. S.; Clarke, N.; Winey, K. I.; Composto, R. J. Do {Attractive} {Polymer}–{Nanoparticle} {Interactions} {Retard} {Polymer} {Diffusion} in {Nanocomposites}? *Macromolecules* **2013**, *46* (11), 4502–4509.

(67) Composto, P. R. J. DYNAMICS IN POLYMER NANOCOMPOSITES Sangah Gam ABSTRACT DYNAMICS IN POLYMER NANOCOMPOSITES Sangah Gam. *Polymer (Guildf).* **2011**.

(68) Griffin, P. J.; Bocharova, V.; Middleton, L. R.; Composto, R. J.; Clarke, N.; Schweizer, K. S.; Winey, K. I. Influence of the Bound Polymer Layer on Nanoparticle Diffusion in Polymer Melts. *ACS Macro Lett.* **2016**, *5* (10), 1141–1145.

(69) Smyda, M. R.; Harvey, S. C. The Entropic Cost of Polymer Confinement. *J.*

Phys. Chem. B **2012**, *116* (35), 10928–10934.

(70) Flory, P. J. *In Principles of Polymer Chemistry*; 1953.

(71) Grosberg, A. Y.; Khokhlov, A. R.; Stanley, H. E.; Mallinckrodt, A. J.; McKay, S. Statistical Physics of Macromolecules. *Comput. Phys.* **1995**.

(72) Bromberg, S.; Dill, K. A. *Molecular Driving Forces*; 2011.

(73) Holt, A. P.; Bocharova, V.; Cheng, S.; Kisliuk, A. M.; White, B. T.; Saito, T.; Uhrig, D.; Mahalik, J. P.; Kumar, R.; Imel, A. E.; et al. Controlling Interfacial Dynamics: Covalent Bonding versus Physical Adsorption in Polymer Nanocomposites. *ACS Nano* **2016**.

(74) Berriot, J.; Montes, H.; Lequeux, F.; Long, D.; Sotta, P. Evidence for the Shift of the Glass Transition near the Particles in Silica-Filled Elastomers. *Macromolecules* **2002**.

(75) Holt, A. P.; Bocharova, V.; Cheng, S.; Kisliuk, A. M.; Ehlers, G.; Mamontov, E.; Novikov, V. N.; Sokolov, A. P. Interplay between Local Dynamics and Mechanical Reinforcement in Glassy Polymer Nanocomposites. *Phys. Rev. Mater.* **2017**, *1* (6), 062601.

(76) Balazs, A. C.; Emrick, T.; Russell, T. P. Nanoparticle Polymer Composites: Where Two Small Worlds Meet. *Science*. 2006.

(77) Burgos-Mármol, J. J.; Patti, A. Unveiling the Impact of Nanoparticle Size Dispersity on the Behavior of Polymer Nanocomposites. *Polymer (Guildf).* **2017**, *113*, 92–104.

(78) Papon, A.; Montes, H.; Hanafi, M.; Lequeux, F.; Guy, L.; Saalwächter, K.

Glass-Transition Temperature Gradient in Nanocomposites: Evidence from Nuclear Magnetic Resonance and Differential Scanning Calorimetry. *Phys. Rev. Lett.* **2012**.

(79) Kalathi, J. T.; Yamamoto, U.; Schweizer, K. S.; Grest, G. S.; Kumar, S. K. Nanoparticle Diffusion in Polymer Nanocomposites. *Phys. Rev. Lett.* **2014**, *112* (10), 1–5.

(80) Nusser, K.; Schneider, G. J.; Pyckhout-Hintzen, W.; Richter, D. Viscosity Decrease and Reinforcement in Polymer-Silsesquioxane Composites. *Macromolecules* **2011**.

(81) Jouault, N.; Moll, J. F.; Meng, D.; Windsor, K.; Ramcharan, S.; Kearney, C.; Kumar, S. K. Bound Polymer Layer in Nanocomposites. *ACS Macro Lett.* **2013**.

(82) Muthukumar, M. Entropic Barrier m o d e l for p o l y m e r Diffusion in Concentrated Polymer Solutions and r a n d o m m e d i A. **1991**, *133*, 654–666.

(83) Gam, S.; Meth, J. S.; Zane, S. G.; Chi, C.; Wood, B. A.; Seitz, M. E.; Winey, K. I.; Clarke, N.; Composto, R. J. Macromolecular Diffusion in a Crowded Polymer Nanocomposite. *Macromolecules* **2011**, *44* (9), 3494–3501.

(84) Lin, C. C.; Ohno, K.; Clarke, N.; Winey, K. I.; Composto, R. J. Macromolecular Diffusion through a Polymer Matrix with Polymer-Grafted Chained Nanoparticles. *Macromolecules* **2014**, *47* (15), 5357–5364.

(85) Gam, S.; Meth, J. S.; Zane, S. G.; Chi, C.; Wood, B. A.; Winey, K. I.; Clarke,

N.; Composto, R. J. Polymer Diffusion in a Polymer Nanocomposite: Effect of Nanoparticle Size and Polydispersity. *Soft Matter* **2012**, *8* (24), 6512–6520.

(86) Imel, A. E.; Rostom, S.; Holley, W.; Baskaran, D.; Mays, J. W.; Dadmun, M. D. The Tracer Diffusion Coefficient of Soft Nanoparticles in a Linear Polymer Matrix. *RSC Adv.* **2017**, *7* (25).

(87) Miller, B.; Imel, A. E.; Holley, W.; Baskaran, D.; Mays, J. W.; Dadmun, M. D. The Role of Nanoparticle Rigidity on the Diffusion of Linear Polystyrene in a Polymer Nanocomposite. *Macromolecules* **2015**, *48* (22), 8369–8375.

(88) Etampawala, T. Neutron Study of Structured. **2013**.

(89) Yin, W.; Dadmun, M. A New Model for the Morphology of P3ht/Pcbm Organic Photovoltaics from Small-Angle Neutron Scattering: Rivers and Streams. *ACS Nano* **2011**, *5* (6), 4756–4768.

(90) Hammouda, B. SANS Basics. **2013**, 1–23.

(91) Schollwöck, U.; Richter, J.; Farnell, D. J. J.; Bishop, R. F. *Lecture Notes in Physics*; 1879; Vol. 21.

(92) Klein, J. Dynamics of Entangled Linear, Branched, and Cyclic Polymers. *Macromolecules* **1986**, *19* (1), 105–118.

(93) Yamamoto, U.; Schweizer, K. S. Microscopic Theory of the Long-Time Diffusivity and Intermediate-Time Anomalous Transport of a Nanoparticle in Polymer Melts. *Macromolecules* **2015**.

(94) Bucknall, D. G.; Butler, S. A.; Higgins, J. S. Communications to the Editor

Real-Time Measurement of Polymer Diffusion Coefficients Using Neutron Reflection. **1999**, 5453–5456.

(95) Sugihara, H.; Kasuga, K. C o Mmuni c Ati o Ns. **2004**, 1480–1483.

(96) Khan, U.; Ryan, K.; Blau, W. J.; Coleman, J. N. The Effect of Solvent Choice on the Mechanical Properties of Carbon Nanotube-Polymer Composites. *Compos. Sci. Technol.* **2007**.

(97) Banerjee, P.; Conklin, D.; Nanayakkara, S.; Park, T. H.; Therien, M. J.; Bonnell, D. A. Plasmon-Induced Electrical Conduction in Molecular Devices. *ACS Nano* **2010**, *4* (2), 1019–1025.

(98) Puosi, F.; Leporini, D. Scaling between Relaxation, Transport, and Caged Dynamics in Polymers: From Cage Restructuring to Diffusion. *J. Phys. Chem. B* **2011**, *115* (48), 14046–14051.

(99) Choi, J.; Hore, M. J. A.; Meth, J. S.; Clarke, N.; Winey, K. I.; Composto, R. J. Universal Scaling of Polymer Diffusion in Nanocomposites. *ACS Macro Lett.* **2013**, *2* (6), 485–490.

(100) Chen, C.; Wylie, R. A. L.; Klinger, D.; Connal, L. A. Shape Control of Soft Nanoparticles and Their Assemblies. *Chem. Mater.* **2017**, *29* (5), 1918–1945.

(101) Mills, P. J.; Green, P. F.; Palmstrøm, C. J.; Mayer, J. W.; Kramer, E. J. Polydispersity Effects on Diffusion in Polymers: Concentration Profiles of D-polystyrene Measured by Forward Recoil Spectrometry. *J. Polym. Sci. Part B Polym. Phys.* **1986**, *24* (1), 1–9.

(102) Arlen, M. J.; Dadmun, M. D.; Hamilton, W. A. Using Neutron Reflectivity to Determine the Dynamic Properties of a Copolymer in a Homopolymer Matrix. *J. Polym. Sci. Part B Polym. Phys.* **2004**.

(103) Composto, R. J.; Kramer, E. J.; White, D. M. Mutual Diffusion in the Miscible Polymer Blend Polystyrene/Poly(Xylenyl Ether). *Macromolecules* **1988**, *21* (8), 2580–2588.

(104) Akcasu, A. Z.; Nägele, G.; Klein, R. Remarks on the “Fast” and “Slow” Mode Theories of Interdiffusion. *Macromolecules* **1995**, *28* (19), 6680–6683.

(105) Kim, E.; Kramer, E. J.; Osby, J. O.; Walsh, D. J. Mutual Diffusion and Thermodynamics in the Blends of Polystyrene and Tetramethylbisphenol-A Polycarbonate. *J. Polym. Sci. Part B Polym. Phys.* **1995**, *33* (3), 467–478.

(106) Akcasu, A. Z. The “Fast” and “Slow” Mode Theories of Interdiffusion in Polymer Mixtures: Resolution of a Controversy. *Macromolecular Theory and Simulations*. 1997, pp 679–702.

(107) Clarke, N.; Colley, F. R.; Collins, S. A.; Hutchings, L. R.; Thompson, R. L. Self-Diffusion and Viscoelastic Measurements of Polystyrene Star Polymers. *Macromolecules* **2006**, *39* (3), 1290–1296.

(108) Antonietti, M.; Sillescu, H. Diffusion of Intramolecular Cross-Linked and Three-Arm-Star Branched Polystyrene Molecules in Different Matrices. *Macromolecules* **1986**.

(109) Fuchs, M.; Schweizer, K. S. Mode-Coupling Theory of the Slow Dynamics of Polymeric Liquids: Fractal Macromolecular Architectures. *J. Chem. Phys.*

1997, *106* (1), 347–375.

(110) Schweizer, K. S.; Fuchs, M.; Szamel, G.; Guenza, M.; Tang, H. Polymer-Mode-Coupling Theory of the Slow Dynamics of Entangled Macromolecular Fluids. *Macromol. Theory Simulations* **1997**.

(111) Lim, S.; Buswell, R. A.; Le, T. T.; Austin, S. A.; Gibb, A. G. F.; Thorpe, T. Developments in Construction-Scale Additive Manufacturing Processes. *Autom. Constr.* **2012**, *21* (1), 262–268.

(112) Rengier, F.; Mehndiratta, A.; Von Tengg-Kobligk, H.; Zechmann, C. M.; Unterhinninghofen, R.; Kauczor, H. U.; Giesel, F. L. 3D Printing Based on Imaging Data: Review of Medical Applications. *Int. J. Comput. Assist. Radiol. Surg.* **2010**, *5* (4), 335–341.

(113) Dinwiddie, R. B.; Kunc, V.; Lindal, J. M.; Post, B.; Smith, R. J.; Love, L.; Duty, C. E. Infrared Imaging of the Polymer 3D-Printing Process. **2014**, *9105*, 910502.

(114) Levenhagen, N. P.; Dadmun, M. D. Interlayer Diffusion of Surface Segregating Additives to Improve the Isotropy of Fused Deposition Modeling Products. *Polymer (Guildf).* **2018**, *152*, 35–41.

(115) Appuhamillage, G. A.; Reagan, J. C.; Khorsandi, S.; Davidson, J. R.; Voit, W.; Smaldone, R. A. 3D Printed Remendable Polylactic Acid Blends with Uniform Mechanical Strength Enabled by a Dynamic Diels-Alder Reaction. *Polym. Chem.* **2017**, *8* (13), 2087–2092.

(116) Levenhagen, N. P.; Dadmun, M. D. Improving Interlayer Adhesion in 3D

Printing with Surface Segregating Additives: Improving the Isotropy of Acrylonitrile-Butadiene-Styrene Parts. *ACS Appl. Polym. Mater.* **2019**.

(117) Ning, F.; Cong, W.; Wei, J.; Wang, S.; Zhang, M. Additive Manufacturing of CFRP Composites Using Fused Deposition Modeling: Effects of Carbon Fiber Content and Length. *Vol. 1 Process.* **2015**, *80*, V001T02A067.

(118) Zhang, J.; Yang, B.; Fu, F.; You, F.; Dong, X.; Dai, M. Resistivity and Its Anisotropy Characterization of 3D-Printed Acrylonitrile Butadiene Styrene Copolymer (ABS)/Carbon Black (CB) Composites. *Appl. Sci.* **2017**, *7* (1), 20.

(119) Yu, W. W.; Zhang, J.; Wu, J. R.; Wang, X. Z.; Deng, Y. H. Incorporation of Graphitic Nano-Filler and Poly(Lactic Acid) in Fused Deposition Modeling. *J. Appl. Polym. Sci.* **2017**, *134* (15), 1–11.

(120) Feng, X.; Yang, Z.; Rostom, S. S. H.; Dadmun, M.; Xie, Y.; Wang, S. Structural, Mechanical, and Thermal Properties of 3D Printed L-CNC/Acrylonitrile Butadiene Styrene Nanocomposites. *J. Appl. Polym. Sci.* **2017**, *134* (31).

(121) Feng, X.; Yang, Z.; Rostom, S. S. H.; Dadmun, M.; Wang, S.; Wang, Q.; Xie, Y. Reinforcing 3D Printed Acrylonitrile Butadiene Styrene by Impregnation of Methacrylate Resin and Cellulose Nanocrystal Mixture: Structural Effects and Homogeneous Properties. *Mater. Des.* **2018**, *138*.

(122) Faes, M.; Ferraris, E.; Moens, D. Influence of Inter-Layer Cooling Time on the Quasi-Static Properties of ABS Components Produced via Fused Deposition Modelling. *Procedia CIRP* **2016**, *42* (Isem Xviii), 748–753.

(123) Gustafsson, S. E.; Log, T. Transient Plane Sourse (TPS) Technique for Measuring Thermal Transport Properties of Building Materials. *Fire Mater.* **1995**, *19* (August 1994), 43–49.

(124) Gustafsson, S. E. Transient Plane Source Techniques for Thermal Conductivity and Thermal Diffusivity Measurements of Solid Materials. *Rev. Sci. Instrum.* **1991**, *62* (3), 797–804.

(125) Scaffaro, R.; Botta, L.; Maio, A.; Gallo, G. PLA Graphene Nanoplatelets Nanocomposites: Physical Properties and Release Kinetics of an Antimicrobial Agent. *Compos. Part B Eng.* **2017**, *109*, 138–146.

(126) Teh, S. L. The Impact of Non-Covalent Interactions on the Dispersion of Fullerenes and Graphene in Polymers. **2010**.

(127) Rodríguez, J. F.; Thomas, J. P.; Renaud, J. E. Mechanical Behavior of Acrylonitrile Butadiene Styrene (ABS) Fused Deposition Materials. Experimental Investigation. *Rapid Prototyp. J.* **2001**.

(128) Sun, Q.; Rizvi, G. M.; Bellehumeur, C. T.; Gu, P. Effect of Processing Conditions on the Bonding Quality of FDM Polymer Filaments. *Rapid Prototyp. J.* **2008**, *14* (2), 72–80.

(129) Parlevliet, P. P. *Residual Strains in Thick Thermoplastic Composites*; 2010.

(130) Wang, T. M.; Xi, J. T.; Jin, Y. A Model Research for Prototype Warp Deformation in the FDM Process. *Int. J. Adv. Manuf. Technol.* **2007**, *33* (11–12), 1087–1096.

(131) D'Amico, A. A.; Debaie, A.; Peterson, A. M. Effect of Layer Thickness on

Irreversible Thermal Expansion and Interlayer Strength in Fused Deposition Modeling. *Rapid Prototyp. J.* **2017**, *23* (5), 943–953.

(132) Kantaros, A.; Karalekas, D. Fiber Bragg Grating Based Investigation of Residual Strains in ABS Parts Fabricated by Fused Deposition Modeling Process. *Mater. Des.* **2013**, *50*, 44–50.

VITA

Sahar Rostom was born in Kuwait on May 28th, 1983. She moved to Egypt while in second grade where she spent her youth over there. After graduating from Ain Shams university in 2004, she received her Masters degree in polymer at Ain Shams university in 2008. She moved to the states in 2009 with her husband who was pursuing his Ph.D in electrical engineering from Texas A&M University. She then moved to Knoxville and joined the Chemistry department at the University of Tennessee where she became the student of Dr. Mark Dadmun.